

Particles at complex membranes: receptors, ligands, and cytoskeleton

Inaugural-Dissertation

zur

Erlangung des Doktorgrads

der Mathematisch-Naturwissenschaftlichen Fakultät

der Universität zu Köln

vorgelegt von

Karandeep Singh

aus Sareyan, Indien

Köln 2018

Berichterstatter: Prof. Dr. Gompper

Prof. Dr. Lässig

Tag der mündlichen Prüfung: 08.05.2018

*Stop trying to fill your head with science - for to fill your heart with
love is enough.*

– Richard P. Feynman

Dedicated to this magical world and its kind, lovely inhabitants.

Acknowledgements

I would like to thank Prof. Dr. Gerhard Gompper for providing me the opportunity to come to Germany and be a part of this novel research. My sincere thanks goes to Dr. Thorsten Auth, who has guided me at each step in the past few years. Whenever I was stuck at any point, his doors were always open for me. I would express my gratitude to my colleagues and friends at ICS-2/IAS-2, who have helped me in all my queries related to work and life, especially Thomas, Shiba, and Arvind. I would like to thank my friends in Cologne and all around the world who have always been there for me, welcomed me with open arms. Last but not the least, I would like to thank my loving family, who support me at every stage of my life.

Thank you everyone, for being who you are! :)

Abstract

Cells internalize cargo via many biological pathways. In all cases, the cargo is encapsulated within a carrier that interacts with the plasma membrane of a cell via wrapping. Unravelling the interactions of nanoparticles with living cells is therefore fundamental for nanomedicine and nanotoxicology. Red blood cells serve as model cells with well-characterized properties. While the lipids in the bilayer are a two-dimensional fluid, the spectrin filaments of the cytoskeleton form a network with fixed connections; while the fluid membrane is characterized by its bending rigidity, the strength of the cytoskeleton can be quantified by its shear modulus. The cytoskeleton in particular reinforces the mechanical strength of the membrane and may also contribute actively to the engulfment of nanoparticles. We use a continuum membrane model with membrane bending energy, membrane adhesion energy, and membrane tension to study the membrane-nano-object interactions, and calculate the membrane deformation energy costs using Helfrich Hamiltonian. The adhesion can be mediated via different mechanisms, like homogeneous van der Waals adhesion, or inhomogeneous receptor-mediated adhesion. We apply simulation techniques used for biomechanics, such as molecular dynamics and Brownian dynamics simulations.

Quantitative experiments addressing the binding of carboxylated polystyrene nanoparticles to human red blood cells reveal saturated adsorption with only sparse coverage of the cell membrane by partial-wrapped nanoparticles independent of particle size. This suggests a restricted number of adhesive sites on the membrane. For adhesion mediated by receptor-ligand bonds, we find partial wrapping of nanoparticles for high bond energies and low receptor densities. We determine sets of receptor densities, receptor diffusion coefficients, minimum numbers of receptors required for multivalent binding of a nanoparticle, and maximum number of receptors that can bind to a nanoparticle based on experimental data and computer simulations. Furthermore, we provide quantitative characterisation and interpretation for both nanoparticle binding and red blood cell shape and deformability changes upon nanoparticle binding.

Designing optimal implants, like brain and cochlear implants, requires high signal-to-noise ratios for electrical signals from cells. This can be achieved extracellularly via microelectrode arrays, where the nanostructure geometries influence their wrapping. We find partial-wrapped and complete-wrapped states for the nanopillar geometries used in the experiments. Using a combination of theory and experiments, we predict that nanopillars with small radii and arrays with large pitches are the most favourable geometries to get wrapped by cell membranes. Our model provides an informed estimate of the optimal nanostructure geometries that maximize the adhered area to design efficient geometries for microelectrode arrays.

Both membrane and cortical cytoskeleton are key players in the passive wrapping process for cell membranes. We study the effect of a cortical spectrin cytoskeleton on nanoparticle wrapping using Brownian dynamics simulations. In particular, we investigate different particle sizes, different persistence lengths of the spectrin filaments, and the effect of the presence of ankyrin protein complexes that additionally bind the cytoskeleton to the lipid bilayer. We find five particle-wrapping regimes with metastable and stable non-wrapped, partial-wrapped and complete-wrapped states. Ankyrin complexes favour wrapping by effectively softening the spectrin network. Smaller particles travel faster through the red blood cell membrane.

We also investigate the entry of malaria-sized particles into red blood cells. The particle-red blood cell interactions depend on the force due to motor vertex, particle-membrane adhesion strength, breaking length of the spectrin bonds, and radius of the particle. In particular, we study the dynamics of the cytoskeletal network allowing cortical cytoskeletal bonds to break. We find that depending on the spectrin breaking length, we observe two types of partial wrapping for the particle: partial-wrapped states with an intact spectrin network, and partial-wrapped states with a broken spectrin network. For short spectrin breaking lengths, the cytoskeletal bonds break on the fly while the particle is traversing through the spectrin network, hence a transition from a partial-wrapped state to a complete-wrapped state. For longer breaking lengths, the particle gets stuck in the network, and after breaking the first spectrin bond it induces an avalanche of breaking bonds. The particle jumps from a partial-wrapped state to a complete-wrapped state. The cytoskeletal crack patterns suggest that longer spectrin breaking lengths facilitate ‘healing’ of the cytoskeleton.

Our calculations offer insights into the interaction of cell membranes with nanostructures, including the aspects of a multi-component lipid bilayer membrane and a cortical cytoskeleton. Furthermore, nanoparticle-covered red blood cells may be exploited as drug delivery systems that circulate in blood.

Zusammenfassung

Zellen können Stoffe, wie zum Beispiel Therapeutika, über viele verschiedene biologische Mechanismen aufnehmen. Dabei wird in allen diesen Fällen die Fracht in einem Trägerstoff eingekapselt, welcher mit der Plasmamembran der Zelle mittels wrapping (Ummantelung) wechselwirkt. The Erforschung dieses wrapping-Prozesses ist grundlegend für die Nanomedizin und Nanotoxikologie. Dabei dienen rote Blutkörperchen, deren Eigenschaften gut charakterisiert sind, als Modellsystem. Während die Lipide in der Doppelschicht als zweidimensionale Flüssigkeit betrachtet werden können, bilden die Spektrin-Filamente des Zytoskeletts ein Netzwerk mit festen Verbindungen. Die lipidmembran ist vor allem durch ihre Biegesteifigkeit gekennzeichnet und die Festigkeit des Zytoskeletts kann durch sein Schermodul quantifiziert werden. Das Zytoskelett verstärkt insbesondere die mechanische Festigkeit der Zellmembran und kann auch aktiv zur Einlagerung von Nanopartikeln beitragen. Wir verwenden für die Untersuchung der Membran-Nanostruktur-Wechselwirkungen ein Kontinuumsmembranmodell, welches durch dessen Membranbiegesteifigkeit, Adhäsionsenergie und Oberflächenspannung charakterisiert ist. Die Adhäsion kann über verschiedene Mechanismen wie zum Beispiel homogene Van-der-Waals-Wechselwirkungen oder inhomogene Rezeptor-ligand Wechselwirkungen vermittelt werden. Wir quantifizieren den Energieaufwand der Membrandeformation mittels des Helfrich Hamiltonian. Zudem verwenden wir Simulationsmethoden aus der Biomechanik, wie zum Beispiel Molekulardynamik- und Brownsche-Dynamik-Simulationen.

Experimente an menschlichen roten Blutkörperchen zur Bindung von carboxylierten Polystyrol-Nanopartikeln zeigen unabhängig von der Partikelgröße eine gesättigte Adsorption mit nur geringer Bedeckung der Zellmembran durch partiell ummantelte Nanopartikel. Dies deutet auf eine begrenzte Anzahl von Haftstellen auf der Membran hin. Für die Adhäsion, die durch Rezeptor-Liganden Wechselwirkungen vermittelt wird, finden wir eine partielle Ummantelung für hohe Bindungsenergien und geringe Rezeptordichten. Basierend auf experimentellen Daten und mittels Computersimulationen bestimmen wir Parameterbereiche von Rezeptordichten, Rezeptor-Diffusionskoeffizienten, der minimalen Anzahl von Rezeptoren, die für eine multivalente Bindung erforderlich sind, und der maximalen Anzahl von Rezeptoren, die an ein Nanopartikel binden können. Darüber hinaus bieten wir eine quantitative Charakterisierung und Interpretation sowohl der Nanopartikel-Bindung als auch der Form und Formänderungen der roten Blutkörperchen als Folge von Bindungen mit Nanopartikeln.

Die Entwicklung von optimierten Implantaten, wie Gehirn- und Cochlea-Implantaten, erfordert ein hohes Signal-Rausch-Verhältnis von den Zellen. Dies wird extrazellulär über Mikroelektroden-Arrays erreicht, wobei die Geometrien

der Nanostrukturen ihre Ummantelung beeinflussen. Wir finden teilweise ummantelte und vollständig ummantelte Zustände für die in den Experimenten verwendeten Nanosäulen-Geometrien. Durch eine Kombination aus theoretischen Berechnungen und experimentellen Messungen finden wir, dass Nanosäulen mit kleinen Radien und Anordnungen mit großen Abständen die günstigsten Geometrien, um von Zellmembranen ummantelt zu werden, aufweisen. Unser Modell liefert eine fundierte Schätzung der optimalen Geometrien von Nanostrukturen, um effizientere Mikroelektroden-Arrays zu entwerfen.

Sowohl die Membran als auch das Zytoskelett spielen eine Schlüsselrolle im wrapping-Prozess und bilden zusammen eine komplexe Struktur. Wir untersuchen die Wirkung des Zytoskeletts auf die Nanopartikelummantelung unter Verwendung von Brownsche-Dynamik-Simulationen. Insbesondere untersuchen wir verschiedene Partikelgrößen, unterschiedliche Persistenzlängen der Spektrin-Filamente und die Wirkung von Ankyrin. Wir finden fünf Partikelpackungsregime mit metastabilen und stabilen nicht ummantelten, teilweise ummantelten und vollständig ummantelten Zuständen. Dabei begünstigt Ankyrin das Ummanteln durch Erweichen des Spektrin-Netzwerks. Zudem wandern kleinere Teilchen schneller durch die Membran der roten Blutkörperchen.

Wir untersuchen auch den Eintritt von Malaria-relevanten Partikeln in rote Blutkörperchen. Die Wechselwirkung zwischen den Nanopartikeln und dem roten Blutkörperchen hängt von der Kraft der molekularen Motoren, der Partikel-Membran-Adhäsionsstärke, der Bruchlänge der Spektrinbindungen und dem Radius des Partikels ab. Insbesondere untersuchen wir die Dynamik des Zytoskelett-Netzwer-

ks, welches für biologische Zellen mit brechenden kortikalen Zytoskelett-Bindungen vorgeschlagen wurde. Wir finden, dass abhängig von der Spektrin-Bruchlänge zwei Arten von Phasenübergängen von einem teilweise ummantelten zu einem vollständig ummantelten Zustand beobachtet werden kann. Für kurze Spektrin-Bruchlängen brechen die Zellskelett-Bindungen instantan, während das Partikel das Spektrin-Netzwerk durchbricht. In diesem Fall beobachten wir also einen kontinuierlichen Übergang von einem teilweise ummantelten zu einem vollständig ummantelten Zustand. Bei längeren Bruchlängen bleibt das Teilchen im Netzwerk stecken und, erst nachdem die erste Spektrin-Bindung bricht, löst sich eine Lawine aus brechenden Bindungen aus. Das Teilchen springt also von einem teilweise ummantelten zu einem vollständig ummantelten Zustand. Die Rissmuster des Zytoskeletts legen nahe, dass längere Spektrin-Bruchlängen die "Heilung" des Zytoskeletts erleichtern.

Unser Modell bietet Einblicke in die Veränderung mechanischer Eigenschaften von Zellmembranen durch Nanopartikel. Darüber hinaus können mit Nanopartikeln bedeckte rote Blutzellen als Träger von pharmazeutischen Wirkstoffen und somit zur Wirkstoffabgabe genutzt werden.

Contents

1	Introduction	1
1.1	Nanoparticles	2
1.2	The cell	3
1.3	The cell membrane	4
1.4	Cellular trafficking across a membrane	5
1.5	Modelling the lipid-bilayer membrane	7
1.5.1	Continuum representation of a membrane	7
1.5.2	The Helfrich Hamiltonian	11
1.5.3	Monge parametrization of a surface	12
1.6	Understanding cellular uptake of nanoparticles: Simulations	15
1.6.1	Two-state model for particle wrapping	17
1.7	Wrapping a single spherical particle	18
1.8	The cytoskeletal network	20
1.8.1	Microtubules	22
1.8.2	Actin filaments	22
1.8.3	Intermediate filaments	23
1.9	Red blood cell cytoskeleton	23
1.10	Outline	25
2	Nanoparticle-decorated red blood cells reveal that particle size controls adsorption, cell shape, and cell deformability	29
2.1	Experimental determination of the absorption of polymeric nanoparticles of different sizes to human RBCs	31
2.2	Simulation of NP adsorption to RBCs	39
2.2.1	Receptor-mediated NP adhesion to membranes: kinetic model	40
2.3	The energetics of receptor-limited NP adsorption to RBCs	46
2.4	NP-induced shape changes of RBCs	51
2.4.1	NP-induced RBC shape changes via area-difference elasticity	52
2.4.2	NP-induced RBC shape changes via attached spherical caps	53
2.4.3	NP-induced RBC shape changes via reduced volume	56
2.5	NP-induced deformability changes of RBCs	57
2.6	Conclusions and Outlook	59

CONTENTS

3	Wrapping of polymeric nanostructures by neurons	61
3.1	Exploring the cell-nanostructure interface	64
3.1.1	Arrays with pitch twice the nanopillar diameter	65
3.1.2	Arrays with constant pitch of $1\ \mu\text{m}$	67
3.2	Theoretical modelling of nanostructure wrapping	68
3.2.1	Wrapping transitions	70
3.2.2	Wrapping diagrams for various σ and w	71
3.2.3	Wrapping diagrams for various r and w	73
3.2.4	Wrapping phase diagrams for w , l , and r of the nanopillar	74
3.2.5	Nanopillar-adhered area relative to the flat surface area	75
3.3	Conclusions and Outlook	77
4	Effect of red blood cell cytoskeleton on particle uptake	79
4.1	The RBC spectrin network as a network of entropic springs	79
4.1.1	Spring constant of an entropic spring	81
4.1.2	The model	82
4.2	Free energy of a particle crossing the spectrin network	84
4.2.1	Wrapping-energy calculations	85
4.2.2	Wrapping diagrams	89
4.3	Particle dynamics and first-passage times	91
4.4	Conclusions and Outlook	91
5	Malaria-like particle-red blood cell interactions	93
5.1	Simulating the particle-spectrin interaction	96
5.2	Particle-membrane interactions	99
5.2.1	Particle wrapping fraction versus time	99
5.2.2	Varying adhesion strength and motor forces	101
5.2.3	Particle wrapping fraction versus particle radius	103
5.3	Particle wrapping phase diagrams	105
5.4	Cytoskeletal crack patterns	105
5.5	Conclusions and Outlook	107
6	Conclusions and Outlook	111
A	First-passage time calculations	115
B	Shear modulus of the RBC spectrin network	117

Chapter 1

Introduction

You know nothing, Jon Snow.

– George R. R. Martin

The beauty of physics is that it enhances our understanding of the wonderful universe we thrive in. From explaining the celestial phenomena with astronomical units to the biological processes happening in our bodies in the range of microns and angstroms, physics is everywhere. We exploit here our physics machinery at hand to understand complex phenomena of cell-membrane interactions. Biophysics is a field of physics in which we try to understand the biological processes happening in nature from a physics point of view. One such phenomenon is the uptake of particles by biological cells. Usually, cargo is encapsulated within a carrier that interacts with the plasma membrane of a cell via wrapping. Thus a way to transport drugs into cells is via wrapping of nanoparticles (NPs), in which the drug is packed inside or attached to a NP. After internalization, the NP is inside an endocytic vesicle. The drug can be released from the endocytic vesicle by vesicle bursting [1]. Understanding the mechanisms involved in these internalization processes, like endocytosis, is important both from a fundamental science as well as from an application point of view. Physics provides us a tool to study and understand NP internalization by investigating energetics and dynamics of NP-cell membrane interactions.

The binding of NPs to cell membranes and the development of nanocarriers that circulate in blood is a cornerstone in targeted drug delivery, because the NPs play an important role in designing efficient drug-delivery agents [2, 3]. Furthermore, nanoparticles are used for food processing and in technological applications [4, 5]. Understanding the interaction of nanoparticles with the plasma membranes of biological cells and their subsequent entry into cells is the basis for understanding the toxicity of nanoparticles, which in turn is immensely important for health and safety [6]. Thus, investigating how NPs interact with cell membranes is an important problem to study. Nanoparticle wrapping by biological membranes depend on shape [7–11] and size [12, 13] of the particle,

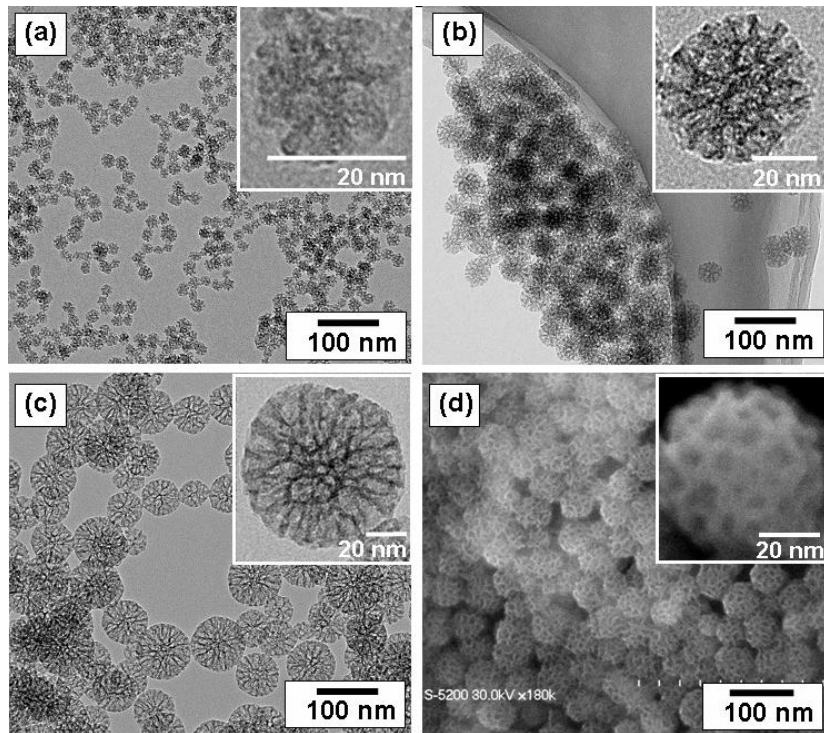


Figure 1.1: Mesoporous silica nanoparticles. Transmission Electron Microscopy images of particles with mean outer diameter (a) 20 nm, (b) 45 nm, and (c) 80 nm. (d) Scanning Electron Microscopy image corresponding to (b). The insets are high magnification images of single particles. Reproduced from Ref. [18].

the interaction between the cell membrane and the particle [14, 15], and bending rigidity and tension of the membrane [16].

1.1 Nanoparticles

A nanoparticle (or nanocluster or nanocrystal) is a particle which extends at least in one dimension less than 100 nm [17] (Fig. 1.1). Nanoparticles act as very small probes that allow us to spy at the cellular machinery without disrupting it at the same time [19]. They have widespread applications in diagnostics and medicine, such as:

- Fluorescent labels [20–22]
- Drug and gene delivery [23, 24]
- Bio-detection of pathogens [25]
- Detection of proteins [26]

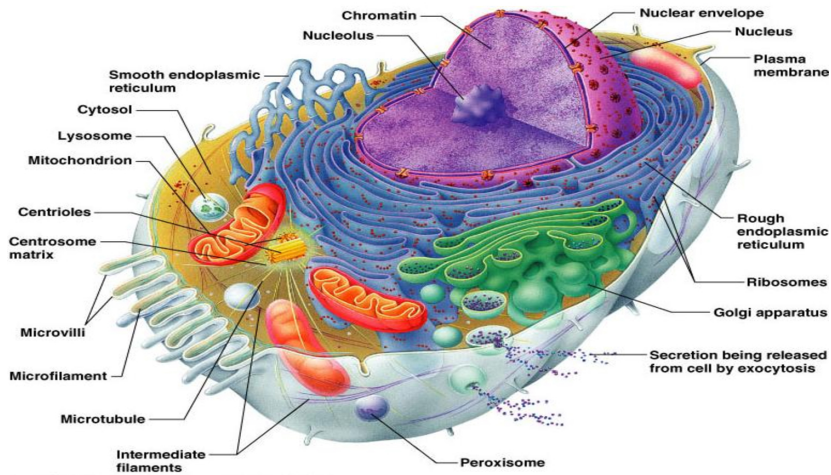


Figure 1.2: Structure of a generalized cell. Reproduced from Ref. [31].

- Probing of DNA structure [27]
- Tissue engineering [28, 29]
- Phagokinetic studies [30]

1.2 The cell

The cell is the basic building block of life [32]. A cartoon representation of a cell is shown in Fig. 1.2. A cell is defined by the plasma membrane, which separates the cytoplasm from the environment of the cell. The numerous functional and structural entities like the cytoskeleton and the cellular organelles exist within this liquid environment. Membrane, cytoskeleton, and the extracellular matrix together provide the structural integrity to cells. Life is reliant on the consumption and dissipation of energy, active processes are occurring all times inside cells. The plasma membrane is usually attached to the cytoskeleton, an interlinking polymerized network of proteins, filaments, and tubules that extends throughout the cytoplasm. Its structure, function and dynamics vary with organism and cell type. It performs a variety of functions, from providing cell shape, and mechanical resistance to deformation, to cell signalling pathways and uptake of particles by cells. Figure 1.3 shows an estimate of the number of cells in an adult human divided by cell type. The red blood cells are the most abundant cells in humans [33].

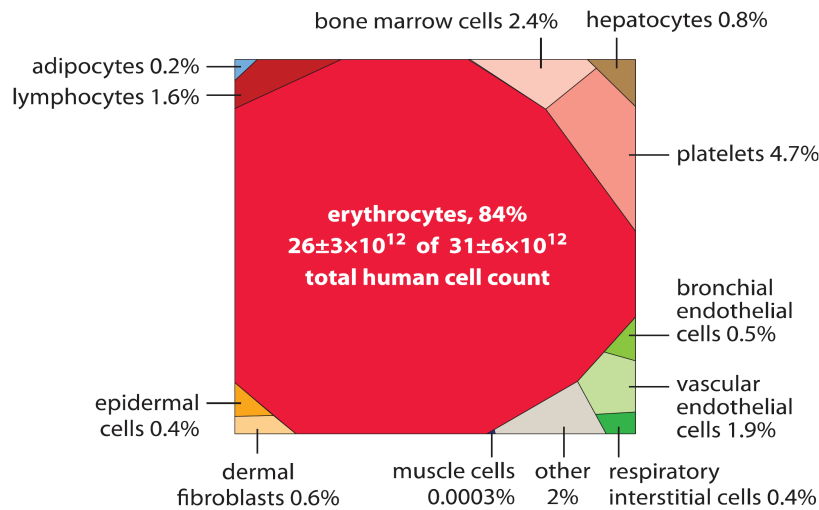


Figure 1.3: Estimate of the number of cells in an adult human divided by cell type. Each cell type in the human body is represented as a polygon with an area proportional to the number of cells. The dominant component is red blood cells. Reproduced from Ref. [33].

1.3 The cell membrane

The cell membrane is a lipid bilayer membrane with a thickness of few nanometers (~ 5 nm) behaving as a two-dimensional fluid at physiological temperatures, where the lipids can diffuse freely within each leaflet of the bilayer. A lipid is an amphiphilic molecule consisting of a polar, hydrophilic (i.e., *water-loving*) head and non-polar, hydrophobic (i.e., *water-fearing*) tails. In an aqueous environment, at a concentration higher than the critical micellar concentration, the lipids self-aggregate into spherical micelles by packing the non-polar tails towards the center of the aggregate, while the polar heads face the aqueous environment (Fig. 1.4). At higher concentrations, the lipids also self-aggregate into cylindrical micelles or bilayer structures, such as vesicles (Fig. 1.4).

In a lipid bilayer, the self-assembly of lipids results in the upper and lower leaflets of the bilayer (Fig. 1.5).¹ The main building blocks of the membrane are phospholipids, cholesterol, and other sterols [37, 38]. Phospholipids belong to either of these main classes: phosphatidylcholine (PC), phosphatidylserine (PS), phosphatidylinositols (PI), phosphatidylethanolamine (PE), sphingomyelin (SM), cardiolipin (CL), and glycolipids (Tab. 1.1). The lipid composition of different

¹In case of non-polar solvents, it is vice-versa, i.e. non-polar tails face the outside environment while the polar heads are packed inside. The morphology of the aggregate depends on the nature of the amphiphile, (i.e., the size of the head group and the hydrophobic tail), but also on the solution conditions (i.e., salt concentration, pH and temperature) [35].

1.4 Cellular trafficking across a membrane

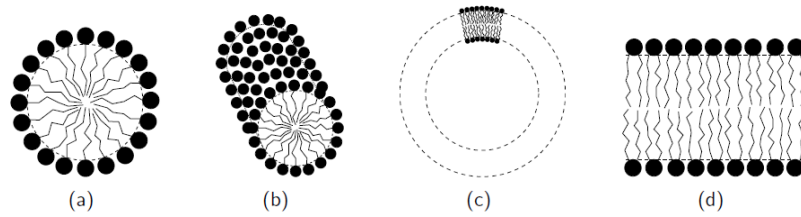


Figure 1.4: Typical structures that result from self-assembly of lipids: (a) spherical micelle, (b) cylindrical micelle, (c) flexible bilayer/vesicle, and (d) planar bilayer. The black circles are the hydrophilic heads, the chains the hydrophobic tails of the amphiphiles. Reproduced from Ref. [34].

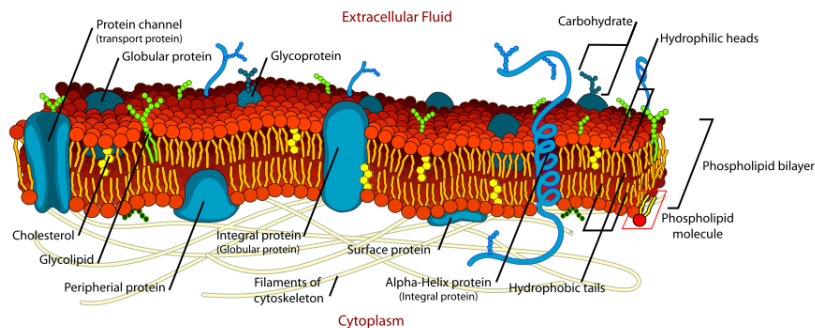


Figure 1.5: Cartoon representation of a lipid bilayer membrane along with other macromolecules such as proteins, polymer chains, and an underlying polymerised cell cytoskeletal network. Reproduced from Ref. [36].

membranes (either of the same cell or of different cells) varies considerably. It can also vary considerably between both the inner and the outer monolayer.

The cell membrane acts as interface separating the interior of a cell from the environment. Apart from its structural task in organizing distinct biochemical compartments, its contributions to essential cellular functions, such as protein organization, sorting, or signalling, play an important role in nature [32, 41]. Many of the tasks, such as exo- or endocytosis [42], the formation of vesicles [43–45], or the interaction with the cytoskeleton [46] play a more important role than just separation of the inner components of a cell from the environment.

1.4 Cellular trafficking across a membrane

In order for the proper functioning of a cell, it needs to exchange molecules and particles intracellularly [41, 47, 48], as well as with its environment [41, 49]. Such a complex physiological process depends on a variety of factors, like size, shape

Introduction

Membrane	PC	PE	PS	PI	SM	CL	Glycolipid	Cholesterol	Others
Erythrocyte (human)	20	18	7	3	18	–	3	20	11
Plasma (rat liver)	18	12	7	3	12	–	8	19	21
ER	48	19	4	8	5	–	tr	6	10
Golgi	25	9	3	5	7	–	0	8	43
Lysosome	23	13	–	6	23	≈ 5	–	14	16
Nuclear membrane	44	17	4	6	3	1	tr	10	15
Mitochondria	38	29	0	3	0	14	tr	3	13
Neurons	48	21	5	7	4	–	3	11	1
Myelin	11	17	9	1	8	–	20	28	6

Table 1.1: Composition of lipids of various membranes from erythrocytes, mammalian liver cells, and nerve cells in weight by percentage. Reproduced from Ref. [39], originally published in Ref. [40].

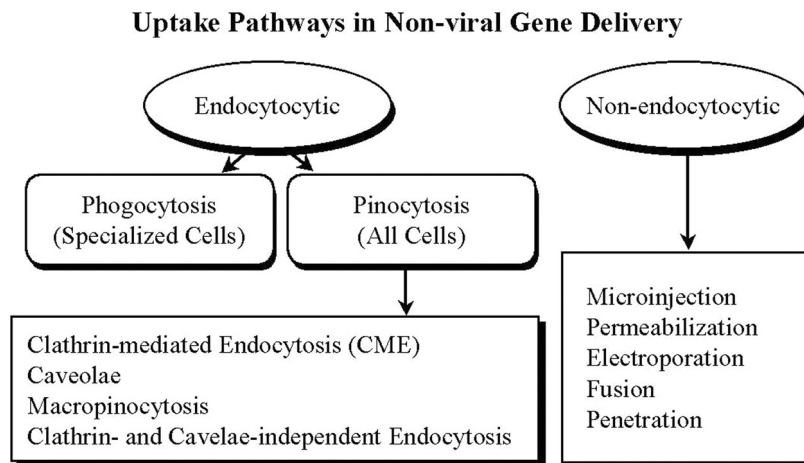


Figure 1.6: Uptake pathways for cellular uptake. Reproduced from Ref. [50].

and chemical composition of the particles, membrane charges and membrane mechanical properties. Cells have devised several efficient pathways for cellular trafficking. They can be broken down into two major cellular uptake pathways, nonendocytotic or energy-independent pathways, and endocytotic pathways [50] (Fig. 1.6). Endocytosis is one of the most important processes used by cells to internalize molecules and macromolecules. It can be classified into two broad categories, phagocytosis for uptake of large particles [51–56], and pinocytosis for uptake of fluids and solutes. Pinocytosis can be further subdivided into clathrin-mediated endocytosis [57–62], caveolae [56,58,63,64], macropinocytosis [56,65,66], and clathrin/caveolae-independent endocytosis [51,67,68]. Different endocytotic mechanisms are shown in Fig. 1.7. Non-endocytotic pathways involve direct penetration [69,70], microinjection [71,72], permeabilization [73,74], and electroporation [75].

1.5 Modelling the lipid-bilayer membrane

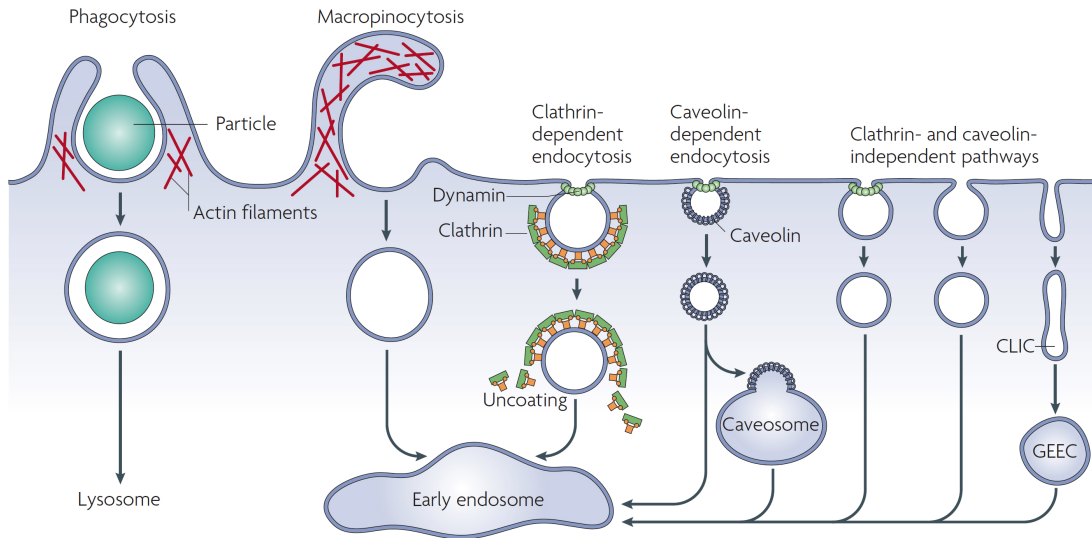


Figure 1.7: Endocytotic pathways. Reproduced from Ref. [51].

1.5 Modelling the lipid-bilayer membrane

The typical thickness of 5 nm for a lipid bilayer is much smaller than the overall dimensions of cells and organelles ($\sim 1-10 \mu\text{m}$). Complete modelling of the membrane with its molecular structure preserved at such length scales is often computationally intractable, thus membranes can be described by two-dimensional mathematical surfaces with curvature elasticity. Continuum membrane models have been used extensively to study a variety of physical phenomena involving membranes: vesicle shapes [76–81], vesicle adhesion [82, 83], colloid wrapping [84, 85], and tether pulling [86–90]. Here, the fluid nature of the lipid bilayer membrane is exploited, and the membrane is modelled as two-dimensional mathematical surface embedded in three-dimensional space. The energy associated with membrane deformations is described by the Helfrich Hamiltonian, which depends on the surface geometry. It costs energy to bend the membrane and this energy cost is quadratic in the curvature. Before we delve directly into the membrane model, we refresh some concepts about curves and surfaces from differential geometry.

1.5.1 Continuum representation of a membrane

The curvature c of a 2-D curve is a measure for the change of its normal vector, and is given by the inverse of the radius r of the osculating circle. Similarly, for a two-dimensional mathematical surface, there exist two principal curvatures c_1 and c_2 at every point, which correspond to the inverse of radii of the circles drawn

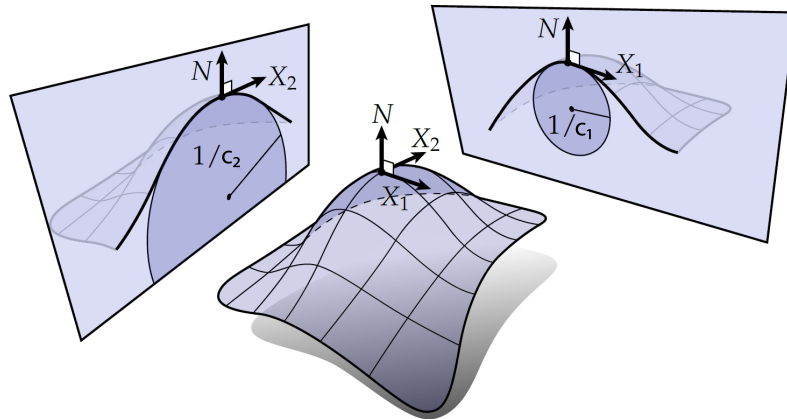


Figure 1.8: The unit vectors X_1 and X_2 along which we find the maximum and minimum normal curvatures c_1 and c_2 are called the *principal directions*; the curvatures c_i are called the *principal curvatures*. Reproduced from Ref. [91].

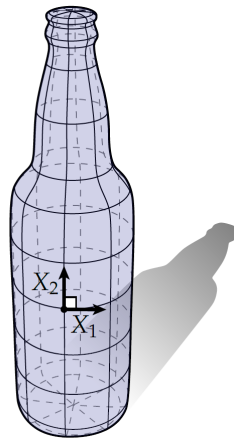


Figure 1.9: The beer bottle has principal curvatures $c_1 = 1/R$, $c_2 = 0$, where R is the radius of the cylindrical part of the bottle. Reproduced from Ref. [91].

at that point having the maximum and minimum radius r_1 and r_2 , respectively (Fig. 1.8). For instance, the beer bottle in Fig. 1.9 has the principal curvatures $c_1 = 1/R$, $c_2 = 0$ at the marked point, where R is the radius of the cylindrical part of the bottle. The principal curvatures tell us everything there is to know about the curvature of a surface at a point, since we can express any tangent vector Y as a linear combination of the principal directions X_1 and X_2 . In particular, if Y is a unit vector, offset from X_1 by an angle θ , then the associated normal curvature is

$$c_n(Y) = c_1 \cos^2 \theta(Y) + c_2 \sin^2 \theta(Y). \quad (1.1)$$

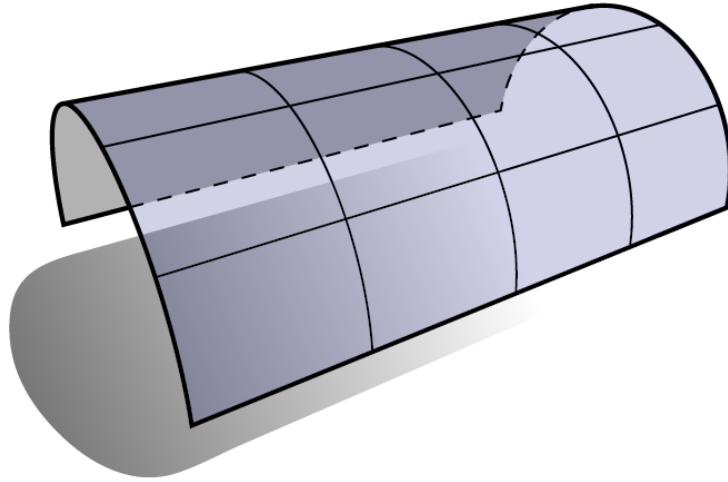


Figure 1.10: Cylindrical surface. Gaussian curvature, $K = 0$. Reproduced from Ref. [91].

The mean curvature

$$H = \frac{c_1 + c_2}{2} \quad (1.2)$$

is the arithmetic mean of the principal curvatures, and the Gaussian curvature

$$K = c_1 c_2 \quad (1.3)$$

is the (square of the) geometric mean. The Gaussian curvature is like a logical “and” (Is there curvature along *both* directions?), whereas the mean curvature is like a logical “or” (Is there curvature along *at least one* direction?).

For some special surfaces, the principal curvatures and associated mean and Gaussian curvatures are as follows:

- For a plane, $c_1 = c_2 = 0$, $H = 0$, $K = 0$.
- For a sphere of radius r , $c_1 = c_2 = 1/r$, $H = 1/r$, $K = 1/r^2$.
- For a cylinder of radius r , $c_1 = 1/r$, $c_2 = 0$, $H = 1/2r$, $K = 0$.
- For a saddle-like surface, $c_1 = 1/r$, $c_2 = -1/r$, $H = 0$, $K = -1/r^2$.

Vanishing-curvature surfaces are well-studied in mathematics and they also have special names. Surfaces with zero Gaussian curvature are called *developable surfaces* because they can be developed or flattened out into the plane without any stretching or tearing. For instance, any piece of a cylinder is developable since one of the principal curvatures is zero (Fig. 1.10). Surfaces with zero mean curvature are called *minimal surfaces*, because they minimize the surface area (with

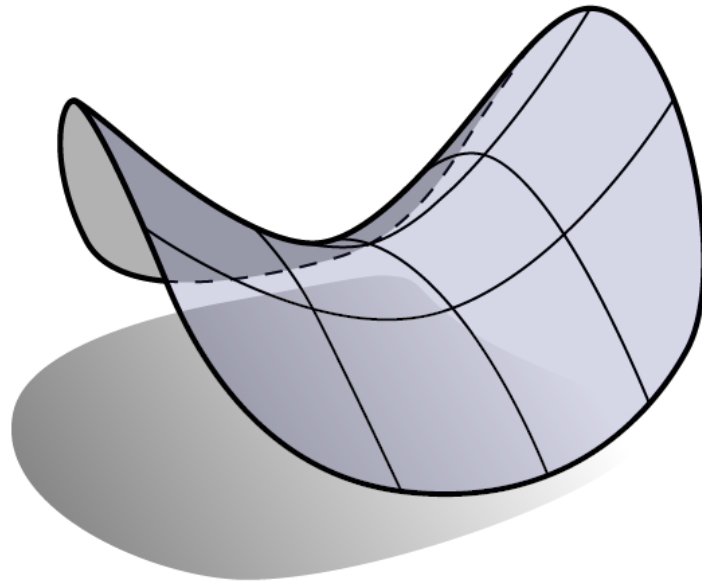


Figure 1.11: Saddle-shaped surface. Mean curvature, $H = 0$. Reproduced from Ref. [91].

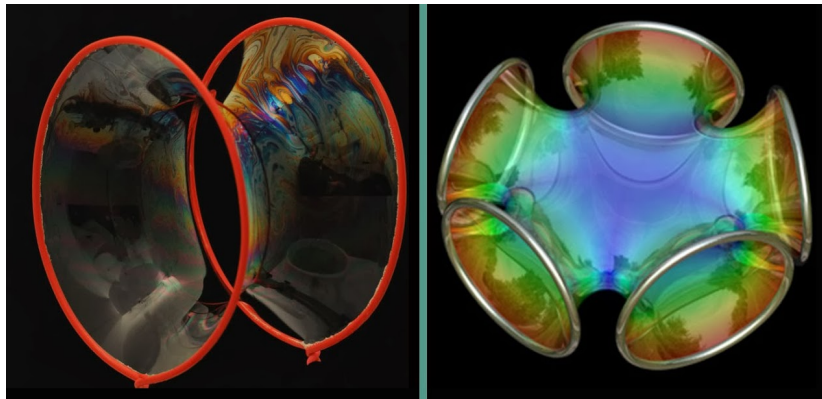


Figure 1.12: Left: Soap film formed between two coaxial rings. Right: Soap film formed between five rings. They form catenoidal surfaces, which have zero mean curvature everywhere. Reproduced from Ref. [92].

respect to certain constraints). Minimal surfaces are saddle-like since the principal curvatures have equal magnitude but opposite sign (Fig. 1.11). One example of a minimal surface is a catenoid, which is formed by a soap film between two coaxial rings (Fig. 1.12). The catenoid is also important in membrane budding, as often the neck of a spherical bud attains a catenoidal shape, which gradually

shrinks and disappears as the bud pinches off.

There are multiple parametrizations reported to investigate membrane shapes [77, 79–81, 93]. A few examples of functional parametrizations are spherical harmonics [94], Fourier functions [95], and Cassini ovals [96]. One of the most frequently occurring surface descriptions in the literature is the so-called *Monge parametrization*. We will discuss it in detail later.

1.5.2 The Helfrich Hamiltonian

A fluid membrane can be described as a mathematical surface with an elastic deformation energy according to Helfrich-Canham [93, 96],

$$\mathcal{H} = \int dA [\sigma + 2\kappa (H - c_0)^2 + \bar{\kappa}K], \quad (1.4)$$

where the integral extends over the entire membrane area, and dA represents the area element. The parameters σ , κ , c_0 , and $\bar{\kappa}$ are the membrane tension, the bending rigidity, the spontaneous curvature, and the saddle-splay modulus, respectively. Typical bending rigidities for biological membranes are in the range of $10 < \kappa < 100 \text{ k}_B\text{T}$ [97–99], membrane tensions are in the range of $7.5 \times 10^{-4} < \sigma < 2.43 \text{ k}_B\text{T}/\text{nm}^2$ [100, 101], and spontaneous curvatures are in the range of $-6 < c_0 < 14 \mu\text{m}^{-1}$ [79, 102].

Membrane tension. Many cell movements proceed via a crawling mechanism, where polymerization of the cytoskeletal protein actin pushes out the membrane of the leading edge [103, 104]. Membrane tension optimizes motility by streamlining polymerization in the direction of movement. Its reduction is correlated with a decrease in cell displacement speed, whereas an increase in membrane tension enhances motility [103]. Similarly, membrane tension is significant for phagocytosis [105] and for biophysicochemical interactions at the nano-bio interface [106].

Membrane bending rigidity. The membrane shape is determined in the following by the changes in the squared mean curvature H^2 and its associated bending rigidity κ . Membrane-induced interactions between curved inclusions, such as proteins or colloidal particles are influenced by the bending rigidity [107, 108]. These curvature-mediated interactions lead to aggregation and vesiculation of membrane proteins [59]. The membrane bending also plays a role in vesicle and particle adhesion, as the particle needs to pay the costs due to membrane bending in order to adhere to the membrane [82, 109, 110]. We will discuss it in more detail later.

Membrane spontaneous curvature. Membranes can have a spontaneous curvature c_0 , which can arise due to various mechanisms [45, 111, 112], (a) different sizes of lipids in the two monolayers [113], (b) membrane scaffolding through cytoskeletal proteins/filaments [114, 115], (c) insertion of extra proteins, which

results in an inhomogeneity in the bilayer [116], (d) presence of intrinsically-curved proteins like the bar-domains [117], and (e) macromolecular crowding [118,119], as shown in Fig. 1.13, along with shape transformations during particle uptake by the membrane [99,120]. For symmetric membranes (identical on both sides) $c_0 = 0$.

Gaussian saddle-splay modulus. The Gaussian saddle-splay modulus only comes into play if there are global topological changes. We invoke here the Gauss-Bonnet theorem, which connects the integral over the Gaussian curvature of a surface with its topology characterized by the Euler characteristic λ [121],

$$\int_P dA K + \int_{\partial P} ds k_g = 2\pi\lambda(P) = 2\pi(2 - 2g). \quad (1.5)$$

Here, dA is the area element of the surface P , ds the line element along the boundary of P , and k_g the geodesic curvature at the boundary. The theorem applies to compact surfaces without boundary, in which case the second integral term drops out [121–123]. The Euler characteristic of a surface is $\lambda(P) = 2 - 2g$, where g is the genus of the surface and counts the number of handles (Fig. 1.14). In fact, among all surfaces that have no boundary and are connected (meaning a single piece), compact (meaning closed and contained in a ball of finite size), and orientable (having two distinct sides), the genus is the only quantity that distinguishes two surfaces from a topological point of view.

A sphere has the Euler characteristic $\lambda = 2$ and a torus $\lambda = 0$, since $g = 0$ and $g = 1$ for a sphere and a torus, respectively. We can also classify minimal surfaces based on their genus. For example, conventionally, triply periodic minimal surfaces (TPMS) must have genus at least 3 [124]. Examples of some minimal surfaces are shown in Fig. 1.15. TPMS are of relevance in natural science [126,127]. They have been observed for biological membranes [128], for block-copolymer self-assembly [129], and as equipotential surfaces in crystals [130]. The Euler characteristic, being a topological invariant, will not change if we deform the surface P . Hence, all the vesicle geometries like prolate, oblate, dumbbell-like [131,132], and starfish [133] can be treated as an overall perturbation of the spherical shape. Therefore, all of them have the same Euler characteristic, $\lambda = 2$, and a constant integral over the Gaussian curvature of 4π . For a constant Gaussian saddle-splay modulus $\bar{\kappa}$, the integral over the Gaussian curvature can thus be neglected in the Helfrich Hamiltonian for dealing with shape transformations only if the topology of the system is conserved.

1.5.3 Monge parametrization of a surface

The Monge parametrization is suitable for surfaces that do not have any “overhangs”, i.e., where the membrane can be described using a unique-valued height field $h(\vec{\rho})$, where $\vec{\rho} = (x, y)$ are the coordinates in the reference plane as shown in Fig. 1.16. The mean curvature H within Monge gauge is [134]

1.5 Modelling the lipid-bilayer membrane

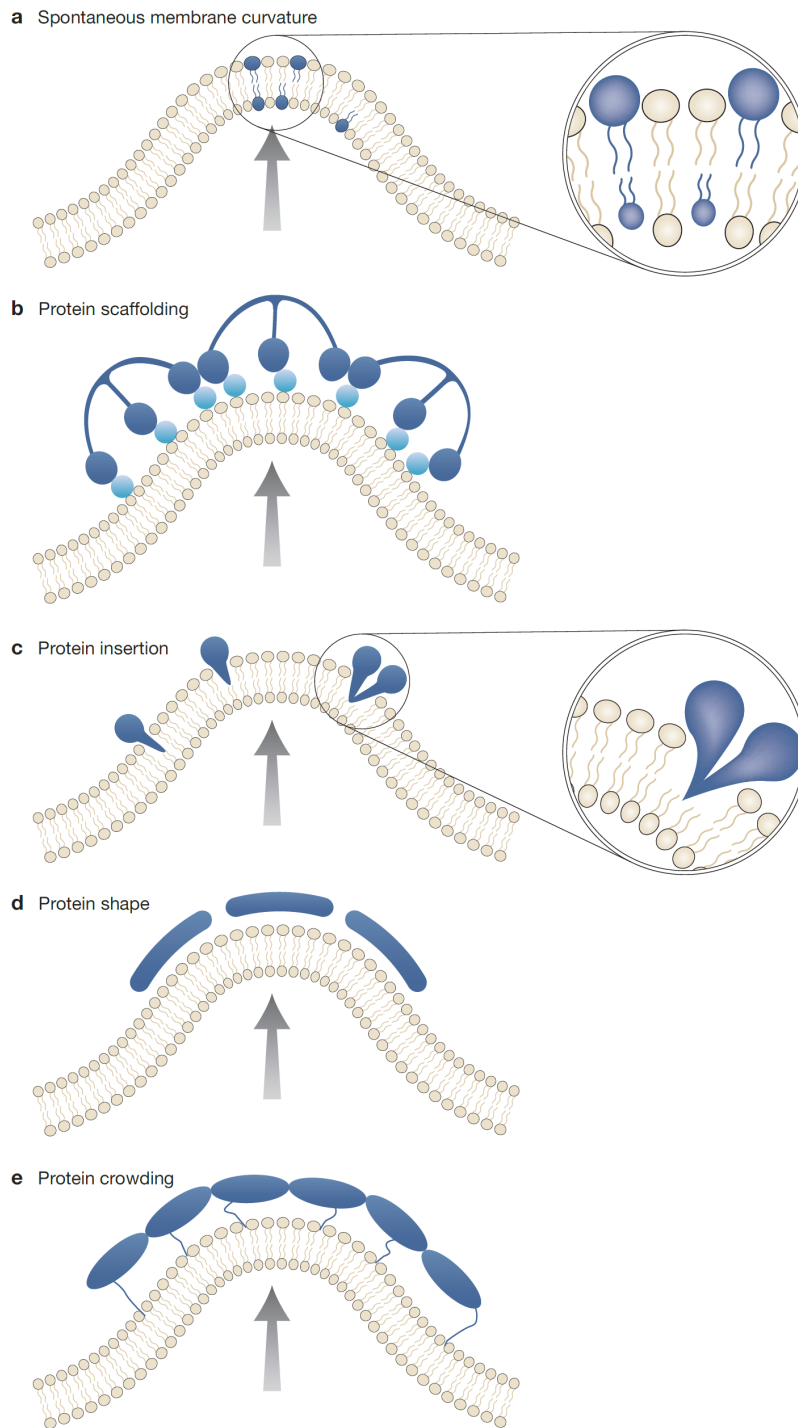


Figure 1.13: Various mechanisms to bend a lipid bilayer. Reproduced from Ref. [111].

Introduction

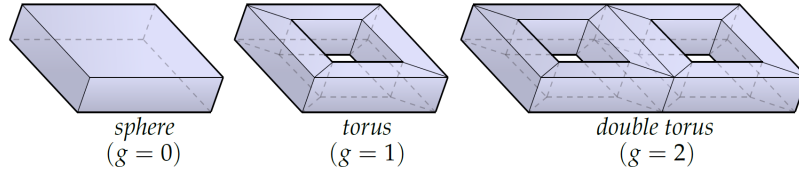


Figure 1.14: Euler characteristic $\lambda = 2, 0, -2$, for a sphere, torus, and a double torus, respectively. The sphere has zero handles (holes), the torus one, and the double torus two, corresponding to the genus g . Reproduced from Ref. [91].

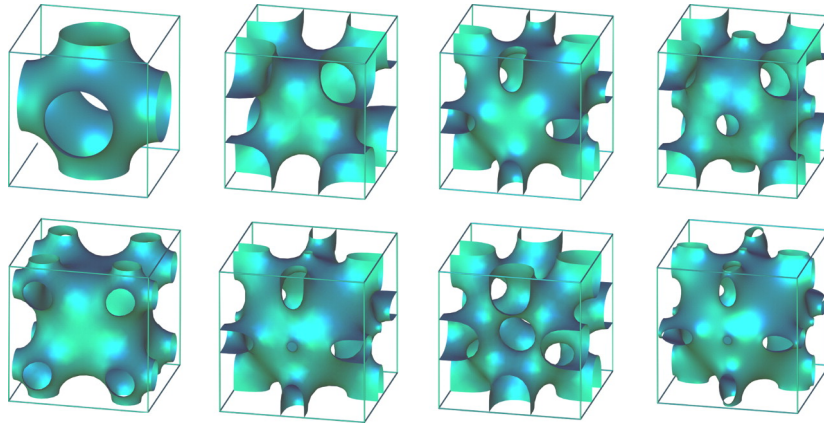


Figure 1.15: Examples of triply periodic minimal surfaces. The first row displays Schwarz-P with $g = 3$, Schoen-IWP with $g = 7$, Neovius N with $g = 9$ and Schoen OCTO with $g = 10 = 3 + 7$, where the sum refers to the combination of handles. The second row shows surfaces obtained by Karcher with $g = 12$, $g = 12 = 3 + 9$ (P- with N-handles combined), $g = 14 = 5 + 9$, and $g = 15 = 3 + 12$, where the sums again refer to the combination of handles. They have zero mean curvature at all points on their surfaces. Reproduced from Ref. [125].

$$2H = \nabla \cdot \left(\frac{\nabla h(\vec{\rho})}{\sqrt{1 + (\nabla h(\vec{\rho}))^2}} \right) \stackrel{|\nabla h| \ll 1}{\approx} \Delta h(\vec{\rho}), \quad (1.6)$$

where ∇ and Δ are the Nabla and the Laplace operator on the base plane, respectively. Hence, the bending energy for the membrane as described by Helfrich-Canham Hamiltonian is

$$\mathcal{E}_{\text{bend}} = \frac{\kappa}{2} \int_{A_{\text{tot}}} dA \sqrt{1 + (\nabla h(\vec{\rho}))^2} \left[\nabla \cdot \frac{\nabla h(\vec{\rho})}{\sqrt{1 + (\nabla h(\vec{\rho}))^2}} \right]^2 \quad (1.7)$$

with $\int dA$ the integral over the reference plane. Using the small-gradient approximation, i.e., for almost planar membranes, the total bending energy for the

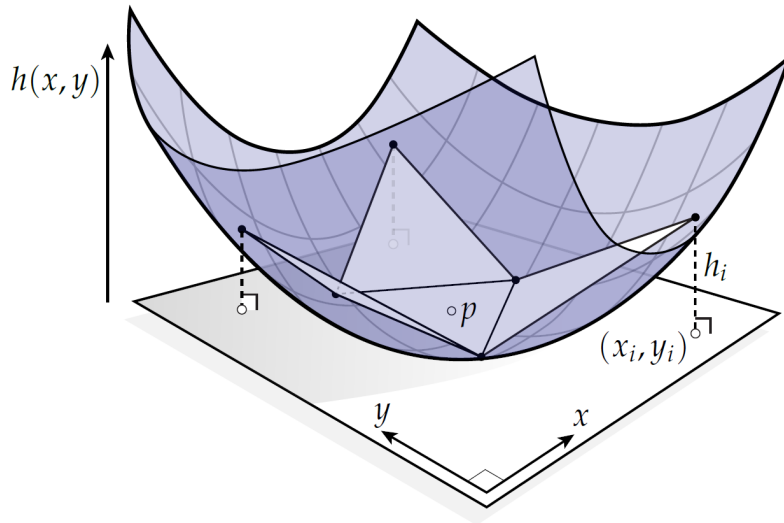


Figure 1.16: A two-dimensional surface described by its height field $h(x, y)$, with its projection in the $x - y$ plane. Reproduced from Ref. [91].

membrane is

$$\mathcal{E}_{\text{bend}} = \frac{\kappa}{2} \int_{A_{\text{tot}}} dA (\Delta h(\vec{\rho}))^2. \quad (1.8)$$

1.6 Understanding cellular uptake of nanoparticles: Simulations

Computer simulation is an important tool to understand cellular processes and to test hypotheses about such processes in a quantitative manner [135–139]. Depending on the length and time scales of interest, different membrane models have to be used (Fig. 1.17) [140, 141]. For example, for processes which occur on relatively small time scales of the order of few nanoseconds, like membrane receptor-ligand binding, a fully-atomistic simulation method can be employed. For investigating biophysical processes at slightly longer time scales ranging from few μs to ms, like fusion-pore dynamics [142], different coarse-grained models can be used, where the molecular resolution of the membrane structure is preserved but chemical specificity is neglected. Another example is a NP passing through a lipid-bilayer membrane, see Fig. 1.18. The membrane wraps around the particle, and after the particle is wrapped completely, it detaches from the membrane [139]. Similarly, aggregation of membrane proteins and vesiculation by curvature-mediated interactions has been studied using coarse-grained simulations, see Fig. 1.19 [59].

However, to investigate processes on the time scales of few seconds, or on

Introduction

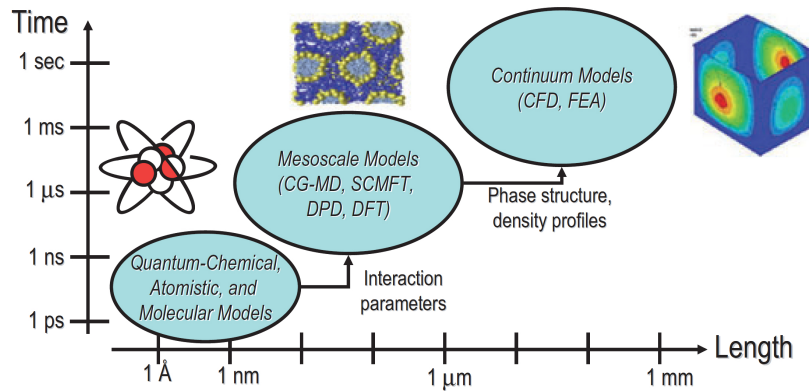


Figure 1.17: Schematic representation of length and time scales involved in various types of physical models of polymeric and biological systems. CFD = computational fluid dynamics; CG-MD = coarse-grained molecular dynamics; DPD = dissipative particle dynamics; FEA = finite element analysis; SCMFT = self-consistent mean field theory; DFT = density functional theory. Reproduced from Ref. [141].

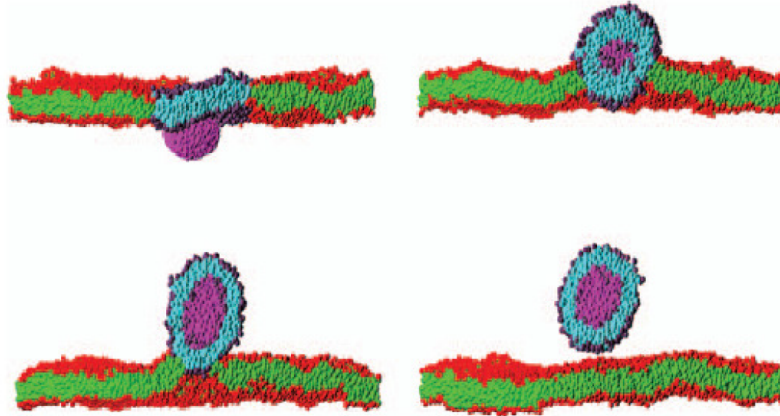


Figure 1.18: Sequence of snapshots of a cross section through a nanoparticle (magenta) translocating across a planar lipid bilayer membrane immersed in solvent. The membrane contains molecules of one lipid type (purple headgroups and cyan tails) surrounded by molecules of the second lipid type (red headgroups and green tails). Reproduced from Ref. [139].

length scales of few microns comparable to the cell size [143, 144], molecular methods are computationally very expensive. Here, mesoscopic models describing cell membranes with a continuum model as a two-dimensional surface prove to be extremely useful [140].

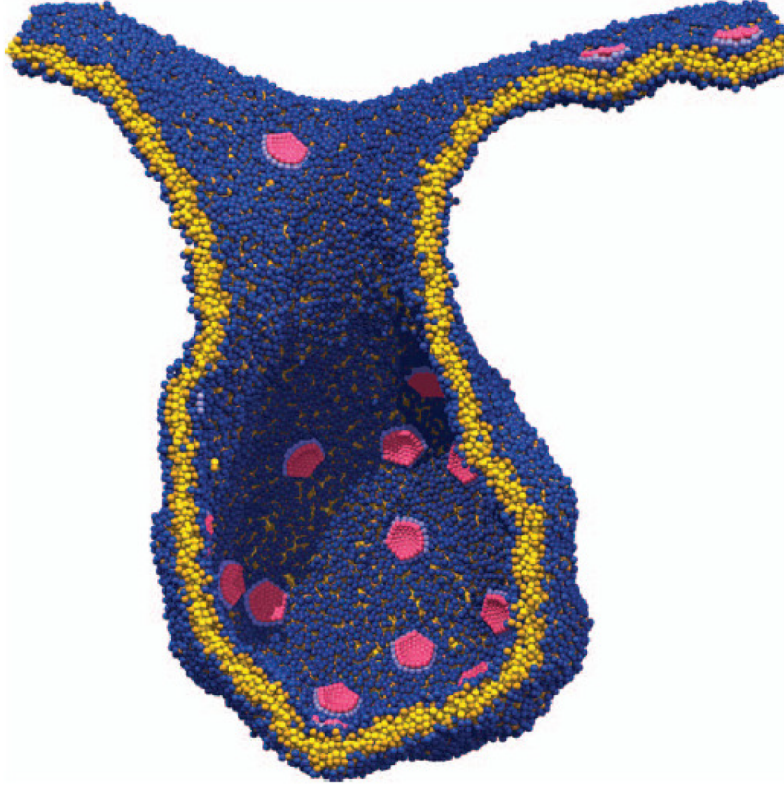


Figure 1.19: A cross section through a membrane invagination driven by the presence of rigid, spherical-cap inclusions. Reproduced from Ref. [59].

1.6.1 Two-state model for particle wrapping

Wrapping of a particle by a membrane can be understood by the competition between the deformation energy cost arising due to bending and stretching of the membrane, and the adhesion energy gain for the contact between particle and membrane. For a membrane with zero tension, the energy contribution due to an infinitely large free membrane around the particle can be neglected, as it attains a catenoidal shape, which is a minimal surface with zero bending energy. Figure 1.20 depicts a simple two-state model for particle wrapping. For a spherical particle of radius R and homogeneous adhesion strength w , and for a complete-wrapped state, the bending energy cost is

$$\mathcal{E}_{\text{bend}} = \frac{\kappa}{2} \int_{A_{\text{tot}}} dA H^2 = \frac{\kappa}{2} 4\pi R^2 \frac{4}{R^2} = 8\pi\kappa, \quad (1.9)$$

and the adhesion energy gain is

$$\mathcal{E}_{\text{adh}} = -w \int_{A_{\text{adh}}} dS = -4\pi R^2 w, \quad (1.10)$$



Figure 1.20: Two-state model for wrapping of a spherical particle of radius R by a membrane with adhesion strength w . (a) A non-wrapped state. (b) A complete-wrapped state.

with adhered area $A_{\text{adh}} = 4\pi R^2$. At the border between a wrapped and non-wrapped particle, the bending energy cost must be balanced by the adhesion energy gain. We obtain a critical adhesion strength $w^* = 8\pi\kappa/4\pi R^2 = 2\kappa/R^2$ for a spontaneous transition without any energy barrier from (a) a non-wrapped state to (b) a complete-wrapped state, as shown in Fig. 1.20. For $R < \sqrt{\kappa/w}$, the membrane bending energy costs are too high, such that the adhesion energy gain cannot compensate them. For typical values of $\kappa = 50 \text{ k}_B\text{T}$ and $w = 0.25 \text{ k}_B\text{T/nm}^2$ [145], one can estimate a minimum particle radius $R_{\text{min}} \approx 22 \text{ nm}$ below which the particles will not get wrapped.

The interaction of NPs with cell membranes is not limited to a homogeneous adhesion strength due to van der Waals attraction as for many model lipid-bilayer systems. One of the adhesive sites is receptors in the membrane that interact with ligands on the particle [146], and it leads to inhomogeneous NP-membrane interactions. For receptor-ligand bonds, both bond energy and receptor entropy within the membrane determine the effective adhesion strength. The maximal number of bound NPs is determined by receptor and ligand densities and the receptor diffusion coefficient within the membrane [147–153]. For gold nanoparticles and Hela cells, for $R > R_{\text{max}} = 50 \text{ nm}$, almost all the free receptors available on the membrane to bind are used up, thus further endocytosis is shut down [154]. Via receptor-mediated adhesion, one can estimate an optimal NP radius R_{opt} for wrapping [145, 148, 155]. At $R_{\text{opt}} \approx 25 - 30 \text{ nm}$, the bending and membrane tension costs balance the adhesion energy gain due to receptor diffusion, and thus the cellular uptake is high [145, 148, 154, 155].

1.7 Wrapping a single spherical particle

From a two-state model, we move on to a more detailed approach to study particle wrapping. Figure 1.21 depicts the wrapping of a spherical particle, where a particle of radius R is partially wrapped at wrapping angle θ . The bending energy can be divided into two parts, arising from the adhered part as well as the free part of the membrane. Thus, we can write the total energy of the particle as

$$\mathcal{E}_{\text{tot}} = \mathcal{E}_{\text{bend}}^{\text{adh}} + \mathcal{E}_{\text{bend}}^{\text{free}} + \mathcal{E}_{\text{adhesion}} + \mathcal{E}_{\text{tension}}, \quad (1.11)$$

1.7 Wrapping a single spherical particle

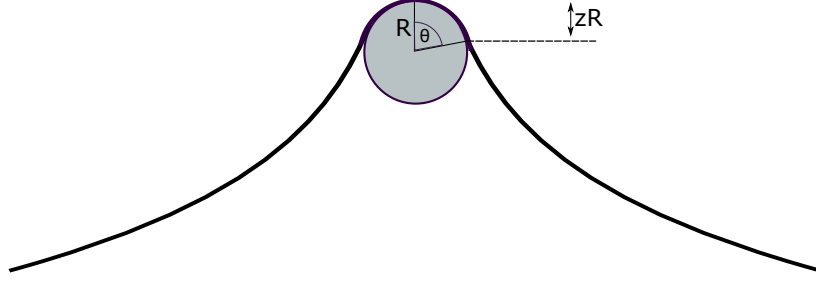


Figure 1.21: For a wrapping angle θ , the membrane wraps around a spherical particle of radius R with a degree of wrapping $z = 1 - \cos \theta$. The degree of wrapping $z = 0$, $0 < z < 2$, and $z = 2$, for a non-, partial-, and a complete-wrapped state, respectively.

where $\mathcal{E}_{\text{bend}}^{\text{adh}}$ and $\mathcal{E}_{\text{bend}}^{\text{free}}$ are the bending energy contributions due to adhered membrane and free membrane, respectively. For a membrane with finite tension, the estimation for the tension energy term is not straightforward and requires numerical approaches [10, 84, 85].

The wrapping fraction is defined as ratio of the wrapped area of the particle to the total area of the particle,

$$f_w = \frac{A_{\text{adh}}}{A_{\text{total}}} = \frac{R^2 \int_0^\theta \int_0^{2\pi} d\theta d\phi \sin \theta}{4\pi R^2} = \frac{1 - \cos \theta}{2}. \quad (1.12)$$

The degree of wrapping is defined as

$$z = 2f_w = 1 - \cos \theta. \quad (1.13)$$

For no wrapping, $z = f_w = 0$, while for complete wrapping, $z = 2$ and $f_w = 1$. The bending energy due to the adhered membrane is,

$$\begin{aligned} \mathcal{E}_{\text{bend}}^{\text{adh}} &= 2\kappa \left(\frac{1}{R} - c_0 \right)^2 \left(2\pi R^2 \int_0^\theta d\theta \sin \theta \right) \\ &= 2\kappa \left(\frac{1}{R} - c_0 \right)^2 [2\pi R^2 (1 - \cos \theta)] \\ &= 4\pi\kappa \left(\frac{1}{R} - c_0 \right)^2 R^2 z, \end{aligned} \quad (1.14)$$

using Eqs. (1.4) and (1.13). Using Eq. (1.10), we can write the adhesion energy

$$\mathcal{E}_{\text{adhesion}} = -w \int_{A_{\text{adh}}} dS = -2\pi R^2 w \int_0^\theta d\theta \sin \theta = -2\pi R^2 w z, \quad (1.15)$$

where we have used Eq. (1.13).

Introduction

The tension contribution is obtained by calculating the excess membrane area, which is equal to the difference of the adhered area $A_{\text{adh}} = 2\pi R^2 z$ and the area enclosed by the projection of the contact line, where the membrane detaches from the particle, to the $x - y$ plane. The radius of the projected circle is $\rho = R \sin \theta$, hence the projected area is $A_{\text{adh}}^{\text{proj}} = \pi R^2 \sin^2 \theta$. Thus

$$\mathcal{E}_{\text{tension}} = \sigma \left(A_{\text{adh}} - A_{\text{adh}}^{\text{proj}} \right) = \sigma (2\pi R^2 z - \pi R^2 \sin^2 \theta). \quad (1.16)$$

Using Eq. (1.13), we can simplify the above equation as

$$\mathcal{E}_{\text{tension}} = \pi R^2 z^2 \sigma. \quad (1.17)$$

Using Eq. (1.15) and Eq. (1.17), we can write the total energy (Eq. (1.11))

$$\mathcal{E}_{\text{tot}} = 2\pi R^2 z \left[2\kappa \left(\frac{1}{R} - c_0 \right)^2 - w \right] + \pi R^2 z^2 \sigma. \quad (1.18)$$

Using dimensionless variables, $\tilde{\mathcal{E}} = \mathcal{E}_{\text{tot}}/\pi\kappa$, $\tilde{w} = 2wR^2/\kappa$, $\tilde{\sigma} = \sigma R^2/\kappa$, and $\tilde{c}_0 = Rc_0$ for reduced energy, reduced adhesion strength, reduced membrane tension, and reduced spontaneous curvature, respectively, we can write Eq. (1.18) as

$$\tilde{\mathcal{E}} = - \left[\tilde{w} - 4(1 - \tilde{c}_0)^2 \right] z + \tilde{\sigma} z^2. \quad (1.19)$$

For a symmetric membrane, $c_0 = 0$, we obtain

$$\tilde{\mathcal{E}} = -(\tilde{w} - 4)z + \tilde{\sigma} z^2. \quad (1.20)$$

Minimizing Eq. (1.20) with respect to z , we identify the different wrapping transitions between the non-wrapped (NW), partial-wrapped (PW), and the complete-wrapped state (CW) (Fig. 1.22). For $\tilde{w} < 4$, the particle is not wrapped, as the adhesion energy gain cannot overcome the bending energy cost. For $4 < \tilde{w} < 4 + 4\tilde{\sigma}$, we obtain a stable partial-wrapped state, indicated by a free-energy minimum for $0 < f_w < 1$. The degree of partial wrapping is $z = 2f_w = (\tilde{w} - 4)/2\tilde{\sigma}$. Full envelopment occurs only for $\tilde{w} > 4 + 4\tilde{\sigma}$, where the membrane completely wraps around the particle resulting in a stable complete-wrapped state.

1.8 The cytoskeletal network

The cytoskeleton is a complex network of interlinking filaments and tubules that extend throughout the cytoplasm, from the nucleus to the plasma membrane. It is a structure that helps cells maintain their shape and internal organization, and it also provides mechanical support that enables cells to carry out essential functions like division and motility. Most of the cytoskeletons consist of three

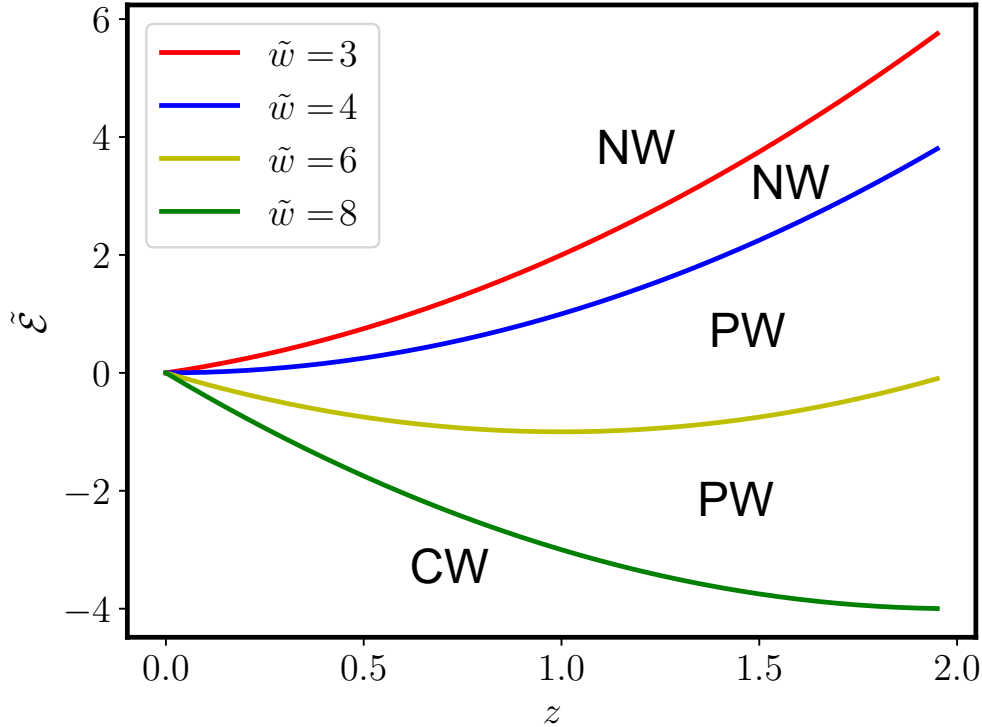


Figure 1.22: Total energy $\tilde{\mathcal{E}}$ of the particle as a function of the degree of wrapping z for tension $\tilde{\sigma} = 1$ for different \tilde{w} values. Wrapping transitions from non-wrapped (NW) to partial-wrapped (PW) and complete-wrapped (CW) states are marked. Here we ignore the bending energy contribution due to the free membrane. The curves correspond to Eq. (1.20).

major classes of elements that differ in size and in protein composition. Microtubules, with an outer diameter of about 25 nm, are composed of a protein called *tubulin*. They have a persistence length of 1 – 8 μm , which shows that a microtubule is essentially rigid over cellular dimensions [156–158]. Actin filaments have a diameter of only about 6 nm, and they are made of globular *actin*. They have a persistence length of 3 – 10 μm , which makes them highly flexible, and this perhaps explains why actin filaments within cells are usually cross-linked into bundles [156, 157]. Intermediate filaments are in between microtubules and actin filaments with respect to the size, with a diameter of about 10 nm. An intermediate filament has a persistence length of $\approx 1 \mu\text{m}$ [156].

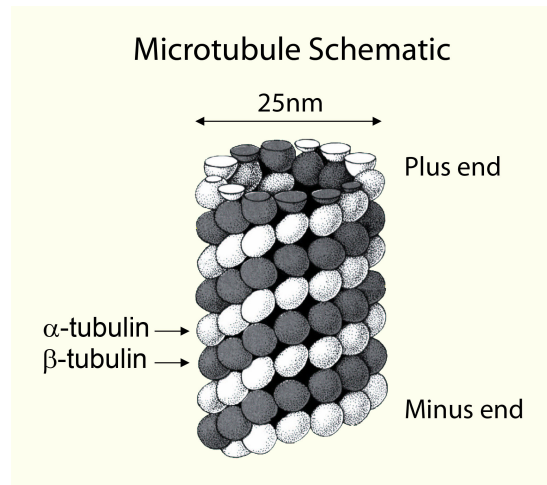


Figure 1.23: Schematic representation of a microtubule depicting its plus and minus ends. Reproduced from Ref. [159].

1.8.1 Microtubules

Tubulin contains two polypeptide subunits, α and β tubulin, that form heterodimers. Many of these heterodimers assemble to form protofilaments. Thirteen linear protofilaments, which are made of vertically-stacked tubulin heterodimers, are arranged side-by-side to form a hollow, cylindrical microtubule [159]. Microtubules have a distinct polarity that is critical for their biological function; one end is called the plus end, and the other one the minus end (Fig. 1.23). They play key roles in (i) intracellular transport, (ii) cell motility, (iii) mitotic spindle formation, and (iv) maintenance of cell shape [160].

1.8.2 Actin filaments

Actin is abundant in all eukaryotic cells, and actin filaments slide along myofilaments to make the cells contract. Actin filaments are made up of globular actin arranged in a long spiral chain [161]. Like microtubules, actin filaments have plus and minus ends, with more ATP-powered growth occurring at the filaments' plus ends. In many types of cells, networks of actin filaments form the cortical cytoskeleton of cells, which is the meshwork of membrane-associated proteins that supports and strengthens the plasma membrane. Such networks allow cells to have specialized shapes, such as the brush border of microvilli [161]. Actin filaments are crucial for tissue organization and for establishing cell polarity and cohesion among epithelial cells, and are also involved in cytokinesis and cell movement (Fig. 1.24) [161]. For example, a core of actin filaments provides microvilli structural support and enables cells to increase their surface area and nutrient-absorbing capacity. In another example, the integrity of epithelial

cell layers or sheets is maintained by a belt of actin filaments (i.e. the adhesion belt). This belt links the cytoskeleton of adjacent cells. Actin filaments is the primary cytoskeletal component to drive cell motility. The filaments found in membrane protrusions, such as filopodia and lamellipodia, rapidly assemble and disassemble. These cellular structures are essential in cell migration and are predominately found at the leading edge of a moving cell. They also allow the cell to probe or sense its microenvironment. The arrays of actin filaments, such as those found in stress fibers, allow a cell to brace against the underlying surface. Actin-associated myosin motor proteins use ATP hydrolysis to exert forces against the stress fibers during muscle contraction; the energy of hydrolysis can also be converted to tensile forces at the trailing cell edge to promote edge retraction in motile cells [161].

1.8.3 Intermediate filaments

Intermediate filaments are rope-like filaments [160]. They are less dynamic than actin filaments or microtubules. Intermediate filaments commonly work in tandem with microtubules, providing strength and support for the fragile tubulin structures [160]. Figure 1.25 shows the structure of intermediate filaments. They are composed of smaller strands in the shape of rods. Eight rods are aligned in a staggered array with another eight rods, and these components all twist together to form the rope-like conformation of an intermediate filament.

All cells have intermediate filaments, but the protein subunits of these structures vary. Some cells have multiple types of intermediate filaments, and some intermediate filaments are associated with specific cell types. For example, neurofilaments are found specifically in neurons (most prominently in the long axons of these cells), desmin filaments are found specifically in muscle cells, and keratins are found specifically in epithelial cells. Intermediate filaments are not polar in the way that actin or tubulin are.

1.9 Red blood cell cytoskeleton

The red blood cell (RBC) cytoskeleton is a highly deformable network, composed mainly of spectrin tetramers with a contour length $l_c = 200$ nm, highly extensible elastic molecules. The spectrin heterodimer consists of intertwined α (280 kDa) and β (246 kDa) polypeptide chains running antiparallel to each other [162, 163]. The α -chain consists of ≈ 22 tandem repeats of triple-helical units of 106 amino acids, whereas the β -chain consists of ≈ 17 such repeat units [164]. The spectrin dimers self-associate to form tetramers and the ends of these tetramers are linked together by junctional complexes containing actin and protein 4.1 to form a hexagonal network [165]. In addition to tetramers, also heterodimers, hexamers, and other spectrin oligomers exist, but they are a minority [166], see Fig. 1.26.

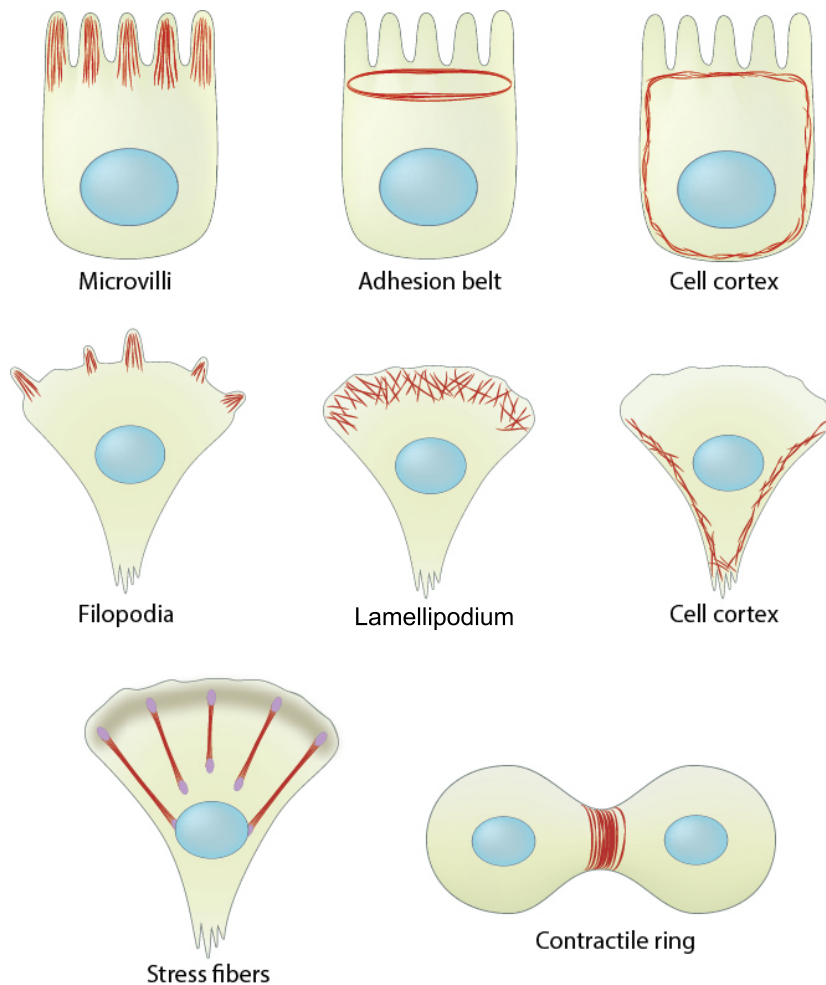


Figure 1.24: Actin filament distribution in cells and tissues. Actin filaments are widely distributed throughout cells, forming a range of cytoskeletal structures and contributing to an even broader range of processes. Reproduced from Ref. [161].

There are about 120,000 tetramers that cover the $140 \mu\text{m}^2$ RBC membrane area, corresponding to a tetramer density of about $800 \mu\text{m}^{-2}$ [174], and 35,000 junction complexes; the average length between the junction complexes is 60 – 100 nm [167]. Band 3 is a transmembrane protein that serves as a major site of skeletal attachment to the lipid bilayer through interactions with ankyrin and protein 4.2 [165, 168–170]. A schematic representation of the RBC cytoskeleton is shown in Fig. 1.27. It is highly convoluted *in vivo*, but can be stretched by about a factor of seven in area to reveal its relatively uniform four-fold to six-fold connectivity [171–173]. The spectrin network plays an important role in maintenance of plasma membrane integrity and RBC deformations [175].

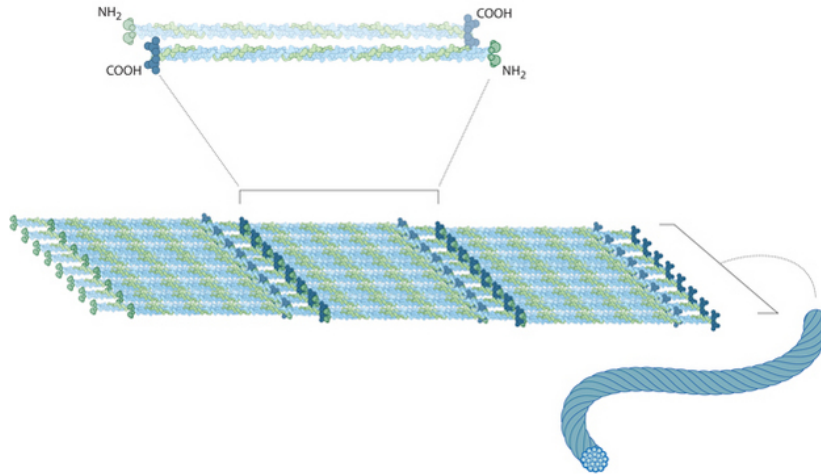


Figure 1.25: The structure of intermediate filaments. Reproduced from Ref. [160].

1.10 Outline

In Chap. 2, we investigate NP wrapping using spherical nanoparticles with attached ligands and lipid-bilayer membranes with receptors that mediate the interaction between membranes and nanoparticles. Our experimental collaborators use pristine nanoparticles, unmodified by proteins and lipids, which enables us to systematically explore the relationship between NP size and surface characteristics to cell adhesion. They characterize both the adsorption of nanoparticles to cells, as well as the cells' mechanical response using electron microscopy, fluorescence microscopy, flow cytometry, and cell deformability measurements. The analytical calculations and computer simulations allow us to interpret the experimental adsorption data using a model based on cooperative binding of adhesive sites on the cells to the particles. In addition, we theoretically discuss mechanisms for nanoparticle adsorption-induced shape changes of RBCs. The well-characterised RBCs serve as model cells, such that the shape changes can be used to quantify effective spontaneous curvatures for nanoparticle-decorated cell membranes of mammalian cells.

Chapter 3 deals with the wrapping of nanopillars by neurons. The cell-surface interface is important for biomedical applications, like brain implants to restore neural functions. The topography of the implantable biomaterials is critical for optimizing the electrical coupling between cells and the device surface. Thus, in-depth understanding of the nanostructure-cell interface is important. We address this problem by a combination of experiments and theoretical modelling. Our experimental collaborators characterize the cell-nanostructure interface using Scanning Electron Microscopy (SEM) and Focussed Ion Beam-Scanning Electron Microscopy (FIB-SEM). The theoretical calculations address the engulfment-like

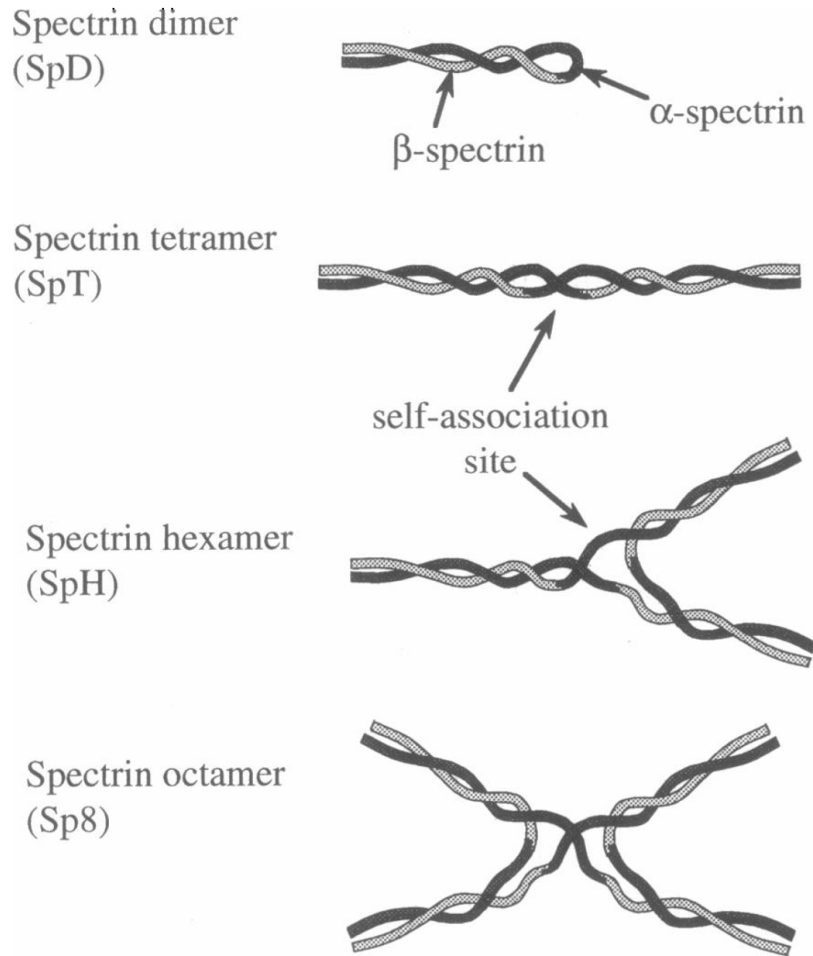


Figure 1.26: Interaction of α -spectrin and β -spectrin in a dimer (SpD), tetramer (SpT), hexamer (SpH), and octamer (Sp8). Reproduced from Ref. [165].

process of the 3D nanostructures by the cell membrane. This wrapping process depends on the membrane mechanical properties, such as bending rigidity and membrane and line tensions, surface properties that determine the nanopillar-membrane adhesion strength, and the geometry of the nanopillar array. We characterize the wrapping transitions between non-wrapped, partial-wrapped, and complete-wrapped states, and systematically study the effect of each parameter.

Chapters 4 and 5 focus on the interaction of spherical nano- and microparticles with a plasma membrane that is supported by a cortical cytoskeleton. We model the spectrin mesh via a network of entropic springs anchored to the lipid bilayer, and calculate the energy associated to the particle uptake process. The presence of ankyrin complexes in the middle of the spectrin filaments shortens

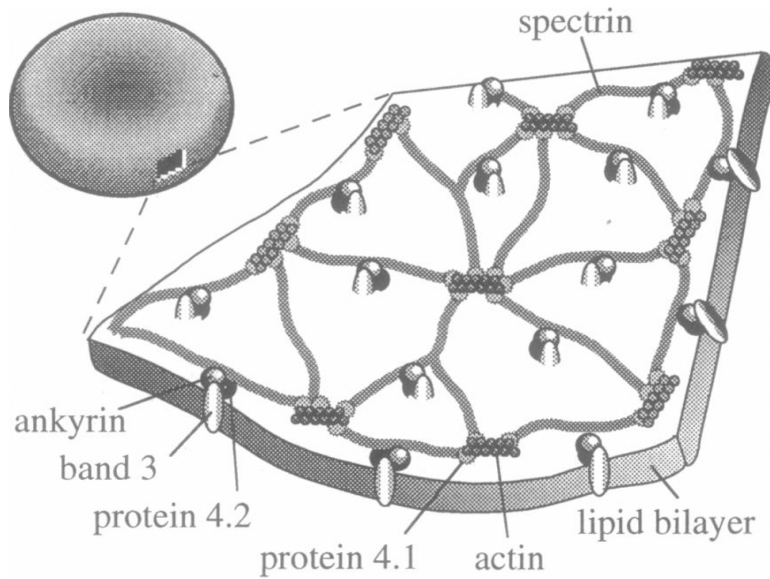


Figure 1.27: Arrangement of the major components of the RBC membrane skeleton. Reproduced from Ref. [165].

their persistence length and makes the springs softer, which in turn helps in particle wrapping by the RBC membrane. Furthermore, we obtain phase diagrams for wrapping transitions from non-wrapped (NW) to partial-wrapped (PW) and complete-wrapped (CW) states. We also identify different wrapping mechanisms depending on the spring breaking length of a spectrin bond, and study systematically the dependence of uptake of malaria-like particles on motor force and adhesion strength. Smaller particles travel through the membrane faster as fewer spectrin bonds are broken compared to the larger ones. Moreover, longer breaking lengths of the spectrin bonds suggest faster ‘healing’ of the cytoskeleton.

Introduction

Chapter 2

Nanoparticle-decorated red blood cells reveal that particle size controls adsorption, cell shape, and cell deformability

Simplicity is the ultimate sophistication.

– Leonardo da Vinci

Adhesion of nanoparticles (NPs) to the plasma membrane of a cell is a crucial step for the initial interaction of NPs with cells. Unravelling the characteristics of this interaction is pivotal for advancements in nanotoxicology and nanomedicine. It has been shown that direct contact between NPs and the plasma membrane of cells constitutes the primary event in nanotoxicology, which is followed by the endocytic uptake of the NPs with possible consequent cytotoxic effects [106,147,176,177]. The binding of NPs to cell membranes is also a cornerstone of targeted drug delivery for nanocarriers decorated with specific ligands that circulate in the blood [178–181]. Nevertheless, quantitative characterization of NP adhesion to the cell membrane has been scarcely addressed [182,183], though a direct relation between the primary adhesion step with the secondary process of NP uptake has been observed [176].

Studies of the interaction of NPs with lipid monolayers, supported lipid bilayers, and unilamellar vesicles have reported that the adsorption of small (~ 20 nm) amorphous silica NPs freeze the lipid bilayer, thereby decreasing the phospholipid lateral mobility, leading eventually to the release of membrane tension through stress-induced formation of a single microsize hole in a giant unilamellar vesicle. In contrast, larger particles (> 80 nm) have been reported to lead to an increased lipid lateral mobility in electrochemical impedance spectroscopy measurements, probably due to membrane defect formation in the membrane, and eventually to collapse of the vesicles [184]. In addition, the extent of interaction of

Nanoparticle-decorated red blood cells reveal that particle size controls adsorption, cell shape, and cell deformability

silica NPs with a dioleoyl phosphatidylcholine (DOPC) monolayer on a mercury film electrode has been shown to be inversely proportional to NP size when the NPs formed a monolayer on the DOPC bilayer, irrespective of their size [185]. Theoretical and computer simulation studies of NP-bilayer interactions range from molecular simulations for small NPs [146, 186–189] to continuum models that can be solved analytically or numerically for NPs with radii of 10 nm and above [11, 16, 85, 190–192]. In the latter case, the deformation energy costs due to bending rigidity and tension for wrapping a lipid bilayer membrane around a NP have to be overcome by the adhesion energy gain for the contact between NP and membrane. In particular, continuum models allow for systematic studies of generic aspects of NP wrapping, such as membrane tension-stabilized partial-wrapped states for spherical NPs [84, 192], continuous and discontinuous wrapping transitions due to different local curvatures of non-spherical NPs [10, 11], membrane-mediated aggregation of NPs [192–195], and NP-induced tube formation [192, 194, 196, 197]. Recently, also stable partial-wrapped states and energy barriers for wrapping because of membrane spontaneous curvature and membrane curvature prior to wrapping have been predicted [190, 191].

Although lipid-bilayer model systems mimic some characteristics of cell membranes, they are devoid of the higher complexity of biological membranes with lipid-protein, protein-protein, and membrane-cytoskeleton interactions. In particular, the interaction of NPs with cell membranes is not limited to a homogeneous adhesion strength due to van der Waals attraction as for many model lipid-bilayer systems. A variety of adhesive sites, such as receptors in the membrane that interact with ligands on the particle [146], electrical charges [198], and domains or rafts that can have different mechanical properties and possibly different hydrophilicity than the surrounding membrane [199, 200] lead to inhomogeneous NP-membrane interactions. For example, for receptor-ligand bonds both bond energy and receptor entropy within the membrane determine the effective adhesion strength. The maximal number of bound NPs is determined by receptor and ligand densities and the receptor diffusion coefficient within the membrane [147–153]. However, very few systematic experimental studies correlate pristine physicochemical properties of NPs that are unmodified by proteins and lipids with NP adhesion to cells.

We investigate the interaction of NPs and red blood cells (RBCs) using an interdisciplinary approach employing experiments, theoretical modelling, and computer simulations. Our study addresses the effect of NP size on the adhesion to human RBCs and the consequent effect on the RBCs' mechanical characteristics as reflected by RBC shape and deformability changes. RBCs do not show active endocytic uptake. This enables us to explore the adsorption of NPs to the complex cell membrane using a receptor model for the NP-cell membrane interaction. Emphasis was put on preserving the pristine physicochemical characteristics of the NPs, employing protein and lipid-free media, in order to prohibit the formation of a “corona” which coats the NP and masks its pristine surface

2.1 Experimental determination of the absorption of polymeric nanoparticles of different sizes to human RBCs

characteristics [153]. This enabled us to systematically explore the relationship between NP size and surface chemistry with their adhesion to the cell membrane. The binding of NPs to cells was initially characterized using Langmuir isotherms. However, since the NPs are strongly attached to the cells, the number of adsorbed NPs per cell appears to be determined by kinetic processes. We interpret the experimental data for the interaction of NPs with RBCs using analytical calculations and computer simulations. We model NP-membrane adhesion using receptor-ligand bonds and calculate the membrane deformation energy using the continuum membrane model introduced in Chap. 1. In order to obtain the wrapping state, we minimize the sum of membrane deformation energy and the receptor free energy. Our calculations predict partial wrapping of the NPs, as observed in the experiments, if there are only few adhesive sites on the cell membrane. Adhered NPs of the smallest size of 27 nm were found to alter the shape distribution of RBCs, such that the fraction of discocytes is decreased. We attribute the experimentally observed shape changes to various mechanisms of NPs altering the spontaneous curvature of the membrane. These shape changes may be responsible for the decreased RBC deformability.

2.1 Experimental determination of the absorption of polymeric nanoparticles of different sizes to human RBCs

In order to quantitatively investigate the adhesion process of NP to the cell membrane without contributions of active biological processes, we have chosen human RBCs as a cellular model, since they are devoid of endocytosis. Our choice of the RBC as a cellular model system emerges also from the many quantitative experiments, computer simulations, and analytical calculations that investigate shapes [177–180, 182] and potentially metabolically-driven shape fluctuations of the cells [81, 102, 146, 180, 183–188, 201–204]. Moreover, the RBC, as the most abundant cell type in blood, has the potential to serve as a drug carrier in nanomedicine [178, 180].

In order to maintain a pristine NP surface devoid of protein or lipid corona, the incubation of RBCs with NPs was carried out in a PBSG medium, containing solely salts and glucose, thereby providing an optimal chemical environment that interferes only minimally both with the surface of the NPs as well as with the RBC membrane.

RBCs were exposed to a suspension of carboxylate surface-modified core-fluorescent polystyrene NPs of three sizes: 27 nm, 45 nm and 100 nm. The exposure was carried out under mild rotatory mixing of the NPs with cells for 15 min at 24 °C. After excessive washing, a combination of fluorescence and differential interference contrast (DIC) microscopy revealed NPs adhered to the RBC

Nanoparticle-decorated red blood cells reveal that particle size controls adsorption, cell shape, and cell deformability

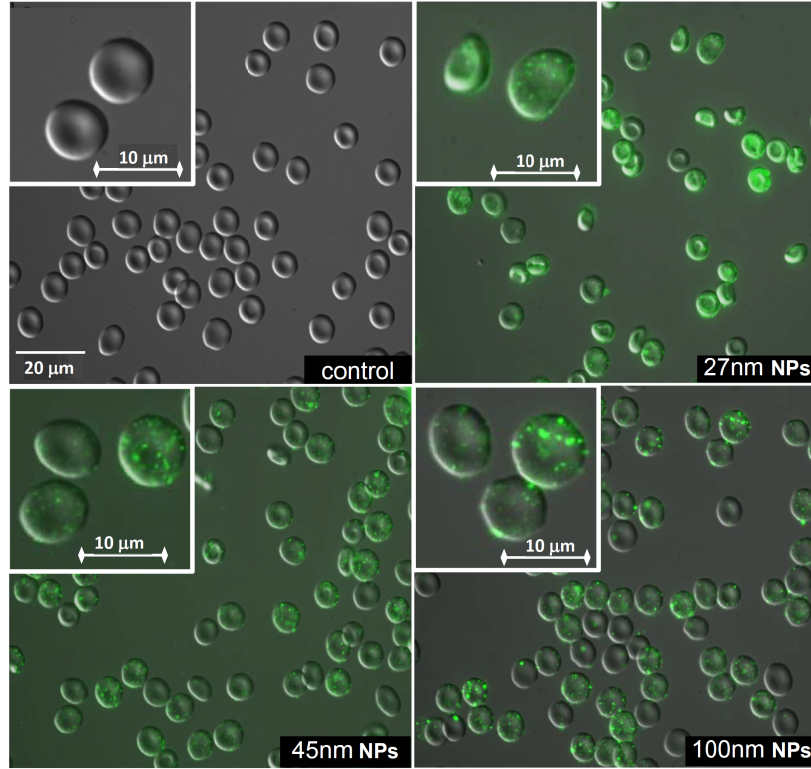


Figure 2.1: Adsorption of carboxylated polystyrene NP to human erythrocytes. Composition of differential interface contrast (DIC) and green fluorescence. Epi-fluorescent and DIC images of RBCs were collected using inverted Zeiss AxioObserverZ1 microscope equipped with $\times 40$ water immersion objective. Incubation of RBC for 15 min at room temperature in suspension with $c_{\text{tot}} = 10^{12}/\text{ml}$.

surface (Fig. 2.1). The RBC population shows an uneven labelling by the fluorescent NPs. Furthermore, some fluorescent spots on the RBC membrane appear to be brighter than others, suggesting the occurrence of NP aggregates. The presence of NP aggregates is further confirmed by scanning electron microscopy (SEM) images (Fig. 2.2). Taking into account the absence of any significant NP aggregation in suspension (Fig. 2.3), we assume that NP clustering occurs directly on the cell membrane surface. The SEM images also show that the NPs are adsorbed to RBC membrane with a significant contact area. In order to quantify the adsorption of NPs to the cell membrane, we exposed RBCs to suspensions of fluorescent NPs possessing concentrations between $c_{\text{tot}} = 1.82 \times 10^9/\text{ml}$ and $c_{\text{tot}} = 9.24 \times 10^{13}/\text{ml}$. Using flow cytometry, we measured the total fluorescence intensity per cell. The average number of NPs adsorbed to a single RBC was calculated (Fig. 2.5, left) using calibrated beads with known amounts of dye molecules (Fig. 2.4), taking into account the manufacturer data on the average

2.1 Experimental determination of the absorption of polymeric nanoparticles of different sizes to human RBCs

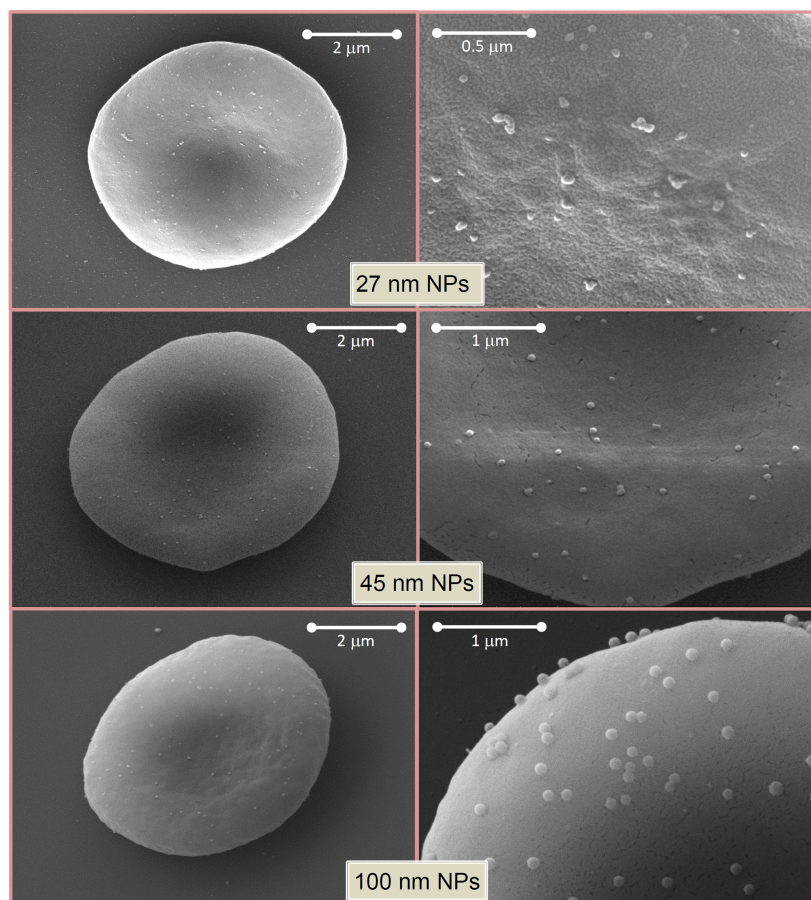


Figure 2.2: SEM micrographs of RBCs. Left panel - magnification $30000\times$, right higher magnifications. For SEM imaging RBCs were attached to round coverslips by incubation in PBSG with 0.9 mM CaCl_2 , 0.5 mM MgCl_2 and 1 mg/ml bovine serum albumin for 20 min at 37°C , washed by PBSG and fixed with PBSG solution containing 1mM EGTA and 2.5% glutaraldehyde. The samples were then dehydrated in a graded series of ethanolwater mixtures and dried by the criticalpoint method. RBC samples were coated with 60/40 gold/palladium alloy and viewed at Quanta 200 ESEM (FEI, USA).

amount of the fluorescent molecules in each batch of the studied NPs. In order to examine the temporal dependence of NP adhesion on the incubation time, we have varied the duration of the exposure of RBCs to NP suspension up to 90 min (Fig. 2.6). Within this time frame, two regimes for the adsorption kinetics can be observed. The fitting of the experimental data by an exponential function (Fig. 2.6) shows the existence of a fast binding kinetics with a characteristic time of ~ 1 min, followed by a much slower kinetic process (Tab. 2.1). This slower process is represented by the almost linear gradual rise for 45 and 100 nm NPs, and

Nanoparticle-decorated red blood cells reveal that particle size controls adsorption, cell shape, and cell deformability

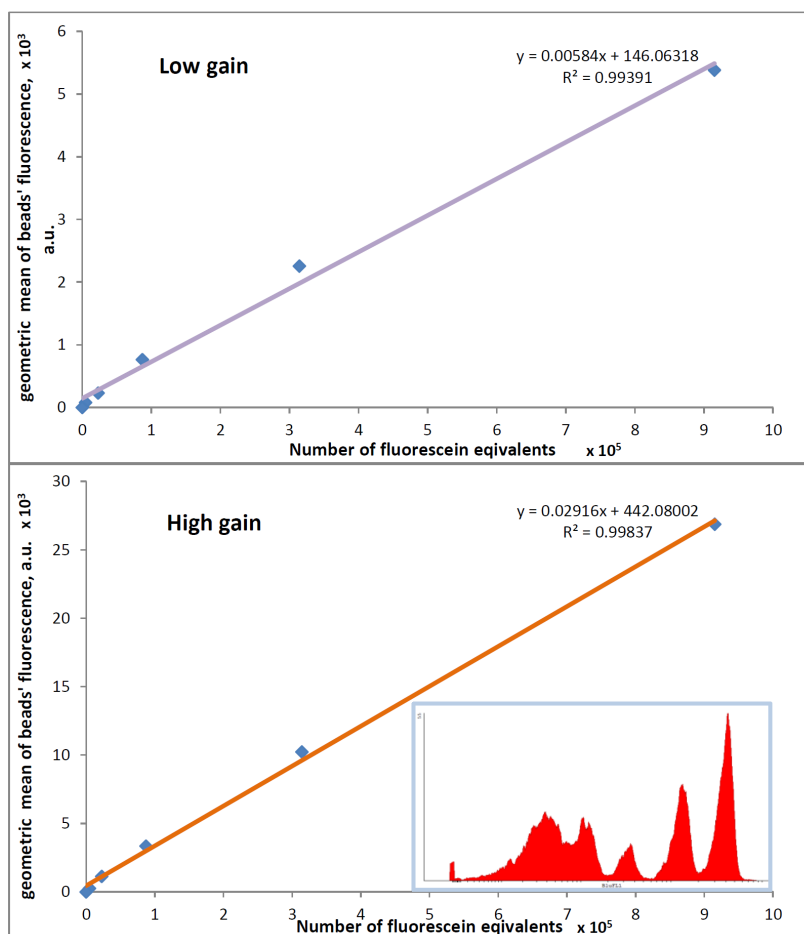


Figure 2.3: Calibration of FACS measurements employing calibrated beads (Bang, USA) with specified amount of fluorescein equivalents. Each flow-cytometry experiment of NP binding to human erythrocytes was accompanied by examining the calibration beads at low (upper panel) and high (lower panel) gain settings for high and low NP concentration ranges respectively. Knowing the fluorophore amount per NP of particular batch (manufacturer data), one can calculate the amount of NPs per cell. Inset: typical FACS green fluorescence distribution histogram of the mixture of calibration beads.

an exponential accumulation with a characteristic time of 30 – 60 min, depending on the NP concentration, for 27 nm NPs. The fast kinetic process is responsible for about 65% of binding of 45 and 100 nm NPs, while for 27 nm NPs the fast fraction is smaller - 20 – 30% of total adsorption. We relate the fast kinetics to the direct interaction of NP with receptors persisting on the cell surface and the slow kinetics to cell membrane rearrangements, such as lipid flip-flop or clustering

2.1 Experimental determination of the absorption of polymeric nanoparticles of different sizes to human RBCs

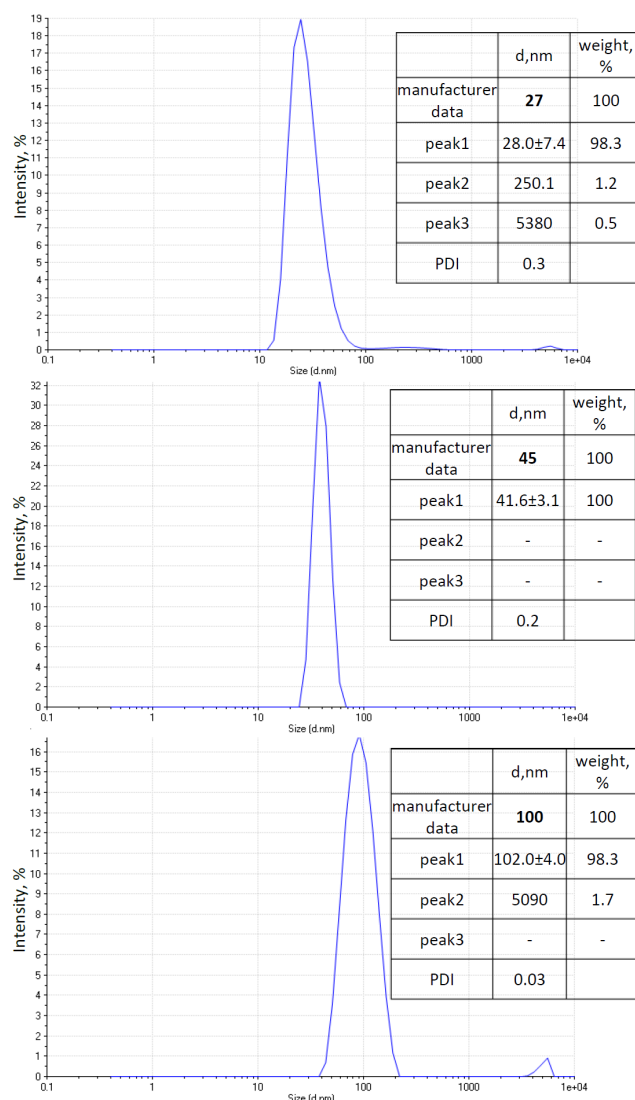


Figure 2.4: Assessment of NP size by dynamic light scattering (DLS). NP size distributions were obtained by analyzing 3.7×10^{12} , 2.0×10^{12} and 7.3×10^{10} NP/ml dispersions in PBSG solution for 27, 45 and 100 nm NPs respectively. The measurements were performed by Dynamic Light Scattering (DLS) using the Zetasizer ZS (Malvern Instruments Ltd, UK). The measurement backscattering angle was set to 173° with the automatic selection for the optimal position and attenuation. The measurement temperature was 25°C with equilibration time of 60 s. Three 60s acquisitions were performed with the delay of 2 s between them. The dispersions were stable for at least 3 hours.

of membrane components, as a result of continued exposure to NPs.¹ Due to the

¹The computer simulations also show a fast and a slow process. For a smaller maximum

Nanoparticle-decorated red blood cells reveal that particle size controls adsorption, cell shape, and cell deformability

NP diameter (nm), c_{tot} (ml^{-1})		A_1	t_1 (min)	A_2	t_2 (min)	Goodness of fit (R^2)
27, 1.0×10^{12}	experimental	22.6 ± 7.7	1.04 ± 1.09	96.6 ± 21.1	53.69 ± 29.86	0.85
	Brownian dynamics simulations	75.35	5.44×10^{-3}	24.67	9.70×10^{-3}	0.99
27, 4.0×10^{12}	experimental	30.2 ± 10.2	0.59 ± 0.76	69.0 ± 11.4	27.03 ± 14.06	0.81
	Brownian dynamics simulations	53.98	2.29×10^{-3}	46.25	2.29×10^{-3}	0.99
45, 2.0×10^{12}	experimental	65.5 ± 5.3	0.56 ± 0.30	2.6×10^{11}	7.02×10^{11}	0.75
	Brownian dynamics simulations	94.05	5.17×10^{-3}	3.84	6.16×10^{-5}	0.99
100, 1.0×10^{12}	experimental	62.4 ± 6.9	0.31 ± 0.47	1.1×10^6	2.6×10^6	0.72
	Brownian dynamics simulations	82.38	8.99×10^{-3}	19.25	1.02	0.99

Table 2.1: Fit Parameters for the exponential association function with experiments and Brownian dynamics simulations.

rise in RBC shape volatility during prolonged incubations in the absence of the stabilizing effect of BSA, we focused our analysis on the fast adsorption phase. We restricted the incubation time with NPs to 15 min, when on the one hand more than 50% of binding occurs (Fig. 2.6) and on the other hand RBC viability is minimally compromised.

The NPs that were still attached to the RBCs after the washing steps appeared to be tightly adsorbed to the RBC membrane and did not show significant desorption during a time period of 4 hours, as validated by flow cytometry (Fig. 2.7). This is consistent with the significant contact area of the NPs with the cell membrane which emerges from the SEM images (Fig. 2.2). The dependencies of the number of adsorbed NPs per cell on the bulk concentration of NPs for all three sizes of NPs, were found to be fitted well by Langmuir-like adsorption model (Fig. 2.5, right). The slope yields the maximal number of NPs adsorbed on a single RBC ($Slope = 1/\text{maximal adsorption}$), while the intercept with y-axis gives the Langmuir adsorption constant K_L for NPs to RBCs ($Intercept = 1/K_L * \text{maximal adsorption}$) (Tab. 2.2). Indeed, comparing the dependence of the binding constant on the NPs size, one obtains higher binding constants for the larger NPs, which is in line with the number of binding sites per NP.

number of receptors that is allowed to bind to a nanoparticle the kinetics of the fast process increases.

2.1 Experimental determination of the absorption of polymeric nanoparticles of different sizes to human RBCs

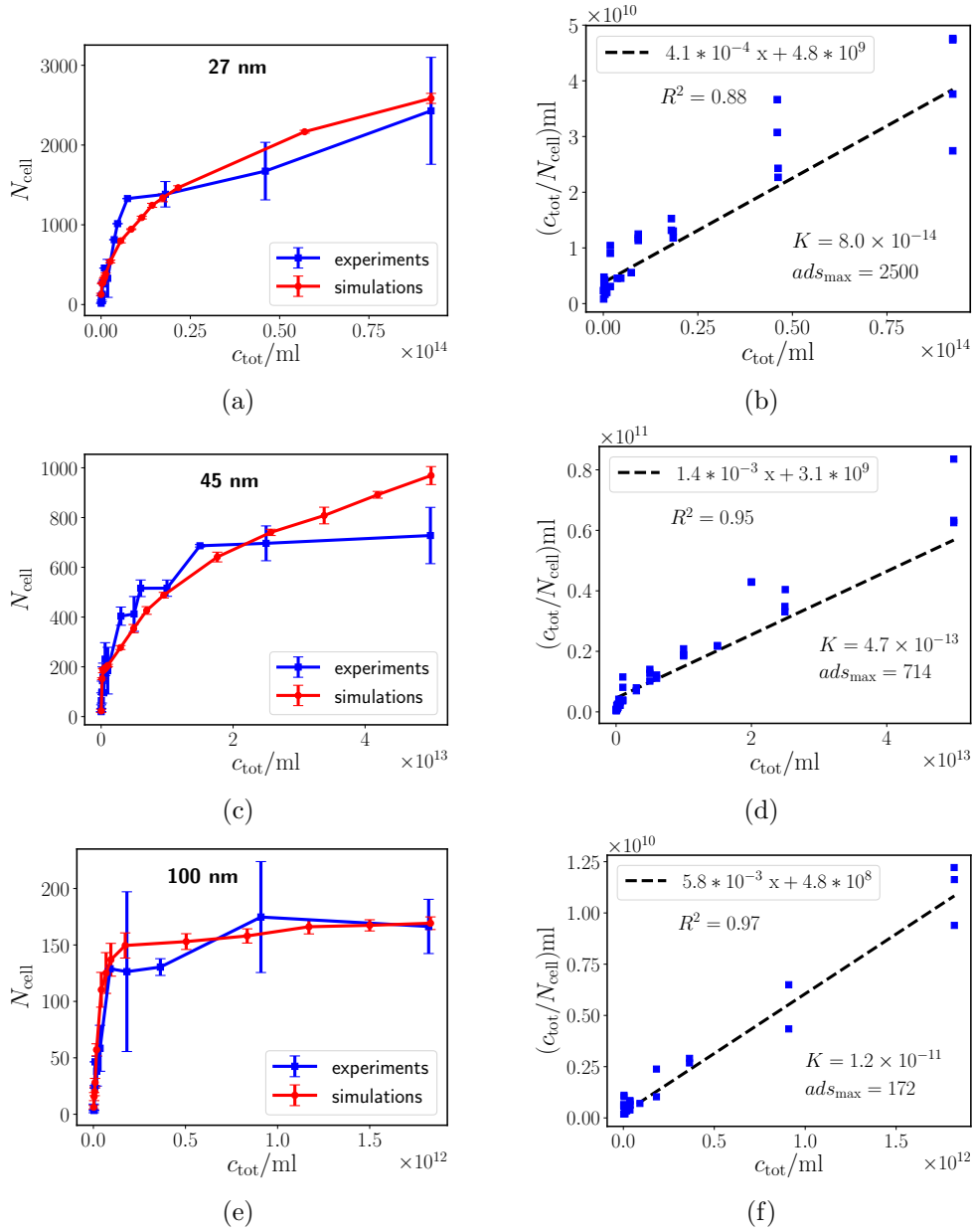


Figure 2.5: Adsorption isotherms of NPs to RBCs and comparison of experimental adsorption data with computer simulations. Left panel - flow cytometry data in terms of adsorbed particles per red blood cell after incubation with nanoparticles of different sizes at various concentrations at 5% hematocrit for 15 min at 24 °C while shaking at 300 rpm. Amounts of adsorbed NPs per RBC (blue lines) are compared to the amounts of adsorbed NPs obtained using Brownian dynamics simulations (red lines). Right panel - linear fitting of the adsorption data of NP of respective size by Langmuir isotherm. Fitting parameters, goodness of fitting as well as maximal adsorption and binding constants are shown at the respective graphs.

Nanoparticle-decorated red blood cells reveal that particle size controls adsorption, cell shape, and cell deformability

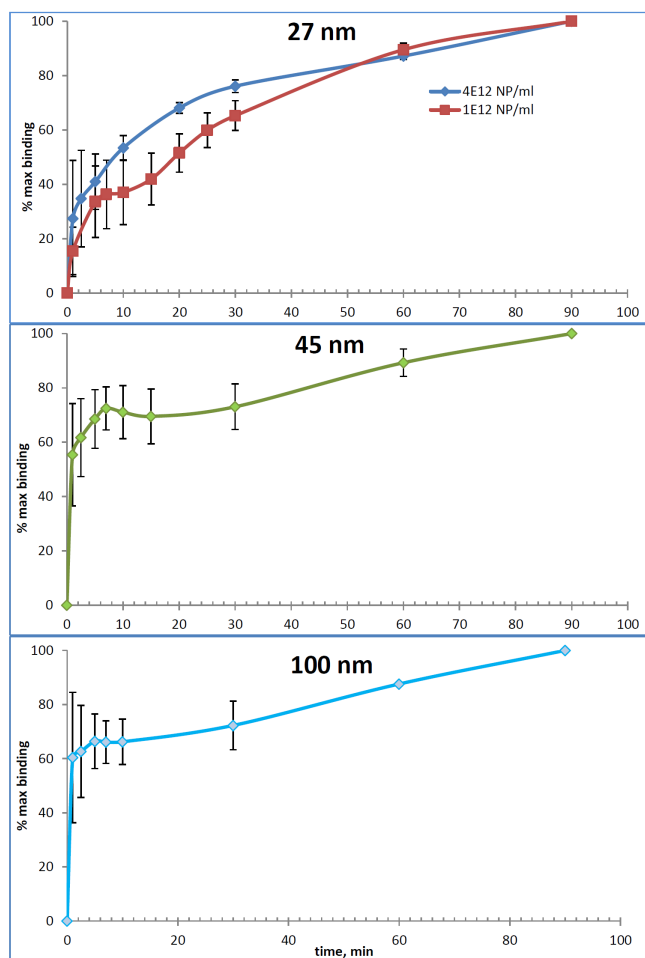


Figure 2.6: Binding kinetics of NPs to RBCs. NPs were incubated with RBCs at concentrations of 4.0×10^{12} NP/ml and 1.0×10^{12} NP/ml for 27 nm NPs, of 2.0×10^{12} NP/ml for 45 nm NPs, and of 1.0×10^{12} NP/ml for 100 nm NPs at 25 °C under mixing (~ 200 rpm) for the specified time period. Subsequently, the solutions were diluted 1 : 50 in a large volume of PBSG in the absence of NPs, then washed twice by centrifugation, and analyzed by flow cytometry. The results were normalized to the maximal binding at 90 min; 3 – 5 independent experiments were performed for each time period. Results are represented as mean \pm SD. Lines results of the fitting of experimental data by exponential association function $f(x) = A_1 (1 - \exp^{-x/t_1}) + A_2 (1 - \exp^{-x/t_2})$ which is sum of the two exponents with characteristic times of t_1 and t_2 and amplitudes of A_1 and A_2 respectively. The fitting was performed employing Origin 6 software (Microcal Software Inc.). Fitting parameters are denoted in Tab. S1.

2.2 Simulation of NP adsorption to RBCs

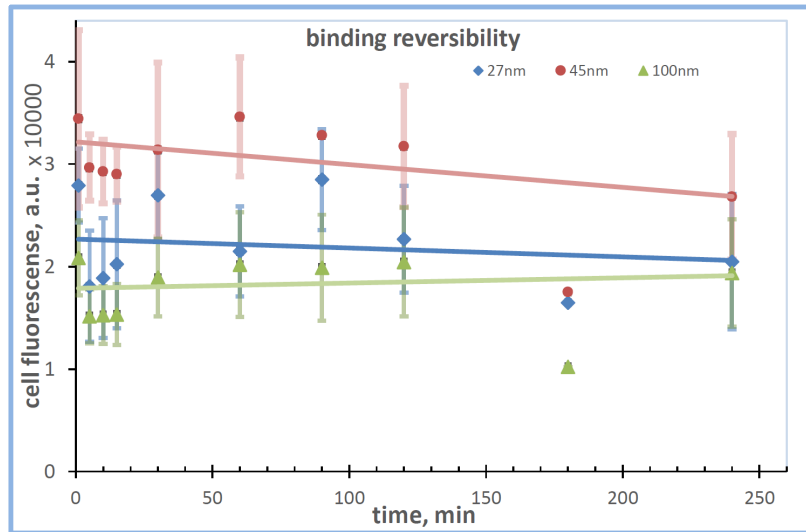


Figure 2.7: Study of desorption kinetics. NPs were incubated with RBCs for 15 min at concentrations of $c_{\text{tot}} = 4.0 \times 10^{12}/\text{ml}$ for 27 nm NPs, $c_{\text{tot}} = 2.0 \times 10^{12}/\text{ml}$ for 45 nm NPs, and $c_{\text{tot}} = 1.0 \times 10^{12}/\text{ml}$ for 100 nm NPs at 25 °C under mixing. Subsequently, the solutions were diluted 1 : 50 in a large volume of PBSG without NPs, washed by centrifugation, and either fixed immediately using 2% glutaraldehyde or further incubated in PBSG without NPs at room temperature while mixing (~ 200 rpm). After the specified period of time, the RBCs were fixed and analyzed by flow cytometry; 3 – 4 independent experiments were performed for each time period. The results are represented as mean \pm SD.

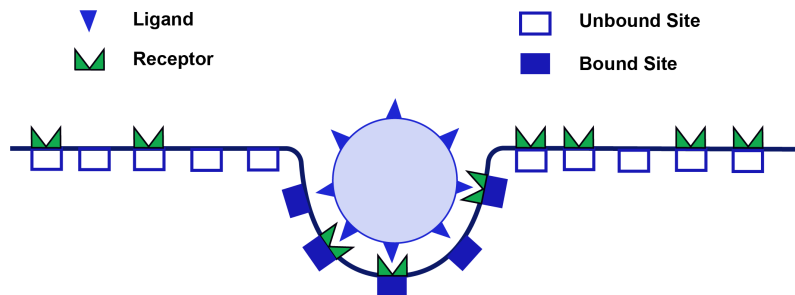


Figure 2.8: The receptor model. The RBC membrane is discretized into sites on that mobile receptors diffuse. When a NP is in the vicinity of the membrane, its ligands bind to these receptors, forming ligand-receptor bonds and initiating the membrane to curve and wrap around the NP.

2.2 Simulation of NP adsorption to RBCs

We simulate NPs adsorption to RBC by taking into account a ligand-receptor interaction model (Fig. 2.8) with a limited number of receptors (binding sites) on

Nanoparticle-decorated red blood cells reveal that particle size controls adsorption, cell shape, and cell deformability

		NP size (nm)		
		27	45	100
NP surface area (nm ²) ♣		2.29×10^3	6.36×10^3	31.41×10^3
COOH groups per particle ♣		4280	22000	107000
maximal adsorption of NPs per cell	Langmuir model	2500	714	172
	Brownian dynamics simulations	2500	1000	175
total surface area of adsorbed NPs (μm ²) *	Langmuir model	5.72	4.54	5.41
	Brownian dynamics simulations	5.92	6.16	5.34
total number of adsorbed COOH groups *	Langmuir model	1.07×10^7	1.57×10^7	1.84×10^7
	Brownian dynamics simulations	1.11×10^7	2.13×10^7	1.82×10^7
Langmuir adsorption constant		8.01×10^{-14}	4.67×10^{-13}	1.16×10^{-11}
NP concentration at 50% occupancy (ml ⁻¹)	Langmuir model	1.25×10^{13}	2.14×10^{12}	8.62×10^{10}
	Brownian dynamics simulations	1.60×10^{13}	9.50×10^{12}	3.20×10^{10}

♣ - manufacturer data; * - at saturation

Table 2.2: Nanoparticle adsorption data.

the membrane. This assumption is in agreement with only 2% of the membrane being adhered to NPs at saturation. Furthermore, our model accounts for (i) NP radius R , (ii) a minimum number r_{\min} of receptors required for a NP to bind to a RBC, (iii) a maximum number r_{\max} of receptors that can bind to a NP, (iv) NP concentration c_{tot} in solution and receptor density σ on the membrane, and (v) NP and receptor diffusion coefficients, D_p and D_r , respectively. Multivalent binding that requires a minimum number of receptors desired for stable NP attachment has also been found for receptor-ligand interaction in the case of supported lipid bilayers [205], while the maximum number of receptors that can bind is given by the number of ligands on the NP.

2.2.1 Receptor-mediated NP adhesion to membranes: kinetic model

We performed Brownian dynamics simulations to investigate irreversible binding of NPs to receptors on the membrane. NPs and receptors are modeled using

2.2 Simulation of NP adsorption to RBCs

spheres of radius r_{NP} and r_{rec} that diffuse in bulk and on the membrane, respectively. The membrane is modeled by a planar wall; parallel to the membrane periodic boundary conditions are used and at the side of the box opposite to the membrane a hard, repulsive wall borders the simulation box. We use a box with dimensions $250 \times 250 \times 1000$ cubed simulation units (su), where $1 \text{ su} = 26.47 \text{ nm}$. For NPs with diameter 27 nm, the lowest NP density in bulk corresponds to $N = 625$ NPs and the highest NP density to $N = 107,100$ NPs. For 45 nm NPs, the numbers of nanoparticles used in the simulations vary between $11 \leq N \leq 58,000$, for 100 nm NPs between $2 \leq N \leq 2,120$. When a NP enters a thin slab above the membrane, the number of receptors that can bind to the NP is calculated. If more than r_{min} receptors are bound, the NP is marked as bound and its position at the membrane is fixed. Further receptors can bind to this NP until the maximum number of receptors, r_{max} , is reached. If less than r_{min} receptors are bound, the NP remains free and can diffuse back to the bulk. The repulsive interaction force between two NPs i and j is given by $F_{ij} = (2r_{\text{NP}} - r_{ij})\hat{r}_{ij}$ if $r_{ij} < 2r_{\text{NP}}$ and $F_{ij} = 0$ otherwise; there is no interaction between receptors. The dynamics of NPs and receptors is calculated

$$\zeta_{\text{NP}}\partial_t r_{\text{NP}} = \sum_{j \neq i} F_{ij} + \sqrt{2\zeta_{\text{NP}}kT}\eta_{\text{NP}}(t), \quad (2.1)$$

and

$$\zeta_{\text{rec}}\partial_t r_{\text{rec}} = \sqrt{2\zeta_{\text{rec}}kT}\eta_{\text{rec}}(t), \quad (2.2)$$

with the frictions coefficients ζ_{NP} and ζ_{rec} for the NPs in solution and for the receptors in the membrane, respectively. The Gaussian white noises $\eta_{\text{NP}}(t)$ and $\eta_{\text{rec}}(t)$ have zero mean $\langle \eta(t) \rangle = 0$ and $\langle \eta(t)\eta(t') \rangle = \delta(t - t')$. Using the Einstein relation, $D = kT/\zeta$, we can express the above equations in terms of the diffusion coefficients for the NPs and the receptors. The equations of motion for NPs and receptors are integrated using Euler algorithm with a time step of $\Delta t = 77.85 \text{ ns}$ [206].

The computer simulations allow us to predict the dependence of the number of adhered nanoparticles per cell on the parameters of the model.

- i. Increasing r_{min} reduces the probability for NPs in the suspension to find a sufficient number of receptors at the same time and therefore reduces NP adsorption.
- ii. Decreasing r_{max} decreases the number of receptors that can bind to each NP, which increases the total number of NPs that can bind to a RBC.
- iii. Increasing σ increases NP adsorption, because there are more receptors available to bind NPs.
- iv. For small NP concentrations, increasing D_r/D_p increases NP adsorption. Higher values of D_r/D_p increase the probability that free NPs find r_{min}

Nanoparticle-decorated red blood cells reveal that particle size controls adsorption, cell shape, and cell deformability

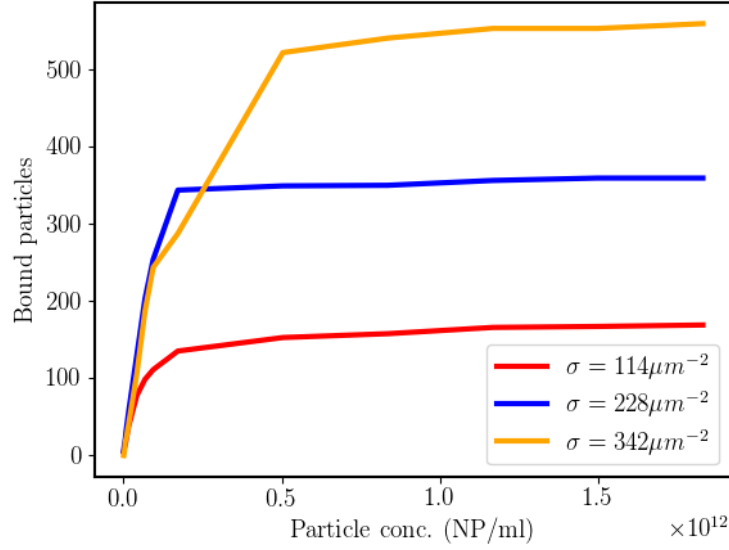


Figure 2.9: Number of bound NPs per RBC for three receptor densities on the membrane.

receptors to attach to RBCs while they are close to the membrane, which results in higher NP adsorption. For high NP concentrations and for small D_r/D_p , decreasing D_r/D_p increases NP adsorption because already bound NPs collect receptors from the system slower than for high ratios D_r/D_p , such that free receptors remain available to attach to NPs in suspension for a longer time.

The NP concentrations in solution are controlled in our experiments (Fig. 2.5), and the NP diffusion coefficients in water of $D_p = 16 \mu\text{m}^2/\text{s}$ for 27 nm NPs, $D_p = 9 \mu\text{m}^2/\text{s}$ for 45 nm NPs, and $D_p = 4 \mu\text{m}^2/\text{s}$ for 100 nm NPs, are calculated using Stokes friction. Experimentally measured diffusion coefficients for proteins within the RBC membranes are $D_r = 0.25 \mu\text{m}^2/\text{s}$ for Band 3 [207], and for lipids within the RBC membranes are $D_r = 0.55 \mu\text{m}^2/\text{s}$ for NBD-PE [208]. These measurements include hindering of the diffusion by the cytoskeleton [59, 209–211]; the diffusion coefficients in the cell are lower than those measured in model lipid bilayers, such as $D_r = 1.7 \mu\text{m}^2/\text{s}$ for glycophorin [212], $D_r = 3.3 \mu\text{m}^2/\text{s}$ for rhodopsin [213], and $D_r = 6 \mu\text{m}^2/\text{s}$ and $D_r = 13.2 \mu\text{m}^2/\text{s}$ for NBD-POPE [214] and NBD-DLPE [214]. Based on the range of diffusion coefficients provided by this published experimental data, we assume $D_r \sim 0.6 \mu\text{m}^2/\text{s}$ for our simulations. We now present systematic studies of the parameter dependence for the number of adsorbed NPs per RBC. Figures 2.9-2.12 show the number of adsorbed NPs as function of the NP concentration in solution for the different cases, in each case

2.2 Simulation of NP adsorption to RBCs

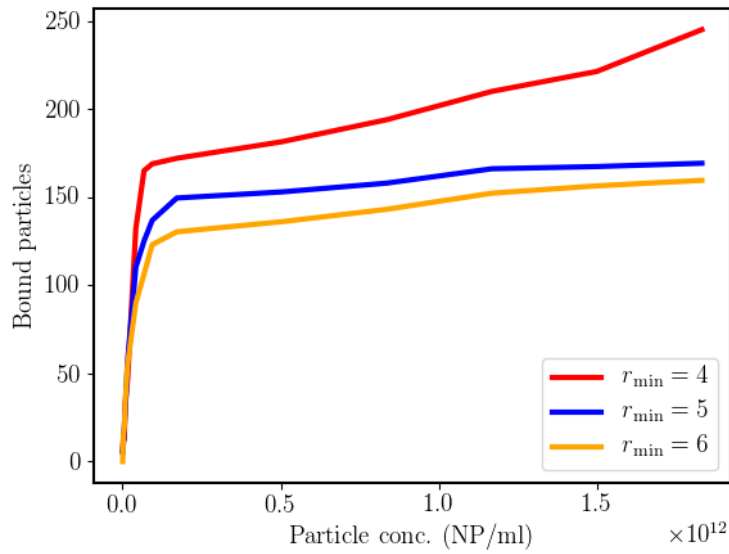


Figure 2.10: Number of bound NPs per RBC for three numbers of receptors required for multivalent binding, r_{\min} .

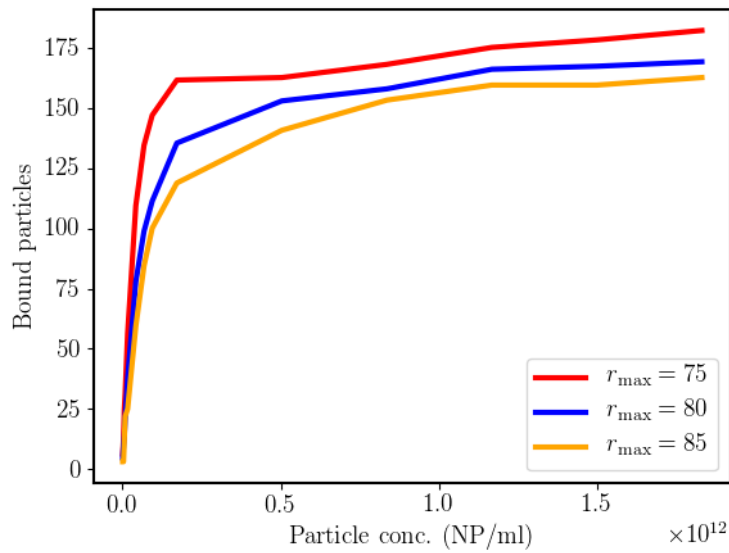


Figure 2.11: Number of bound NPs per RBC for three maximum numbers of receptors that can bind to a NP, r_{\max} .

Nanoparticle-decorated red blood cells reveal that particle size controls adsorption, cell shape, and cell deformability

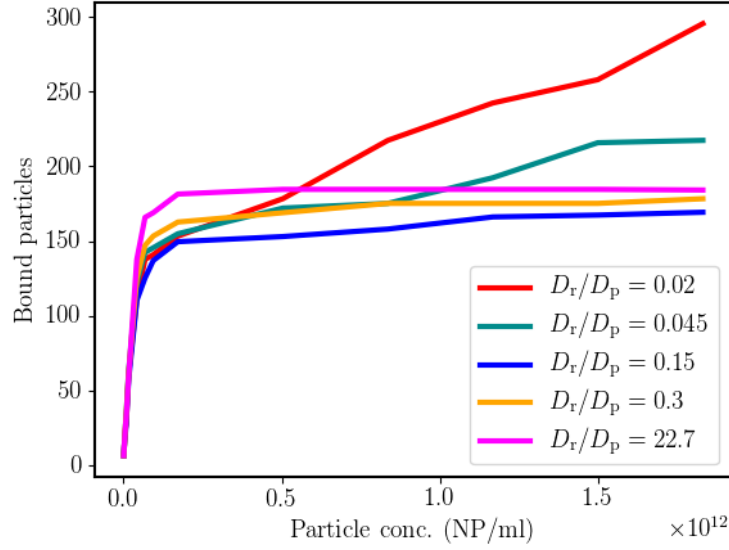


Figure 2.12: Number of bound NPs per RBC for five ratios of receptor and NP diffusion coefficients, D_r/D_p .

keeping all but one parameter fixed.

- (a) **Varying σ :** We plot NP adsorption for three receptor densities, $\sigma = 114 \mu\text{m}^{-2}$, $\sigma = 228 \mu\text{m}^{-2}$, and $\sigma = 342 \mu\text{m}^{-2}$. $r_{\min} = 5$, $r_{\max} = 80$, and $D_r/D_p = 0.15$ (Fig. 2.9). Increasing σ increases NP adsorption.
- (b) **Varying r_{\min} :** We plot NP adsorption for three different minimum numbers of receptors required for multivalent binding, $r_{\min} = 4$, $r_{\min} = 5$, and $r_{\min} = 6$. $\sigma = 114 \mu\text{m}^{-2}$, $r_{\max} = 80$, and $D_r/D_p = 0.15$ (Fig. 2.10). Increasing r_{\min} reduces NP adsorption.
- (c) **Varying r_{\max} :** We plot NP adsorption for $r_{\max} = 60$, $r_{\max} = 80$, and $r_{\max} = 90$. $\sigma = 114 \mu\text{m}^{-2}$, $r_{\min} = 5$, $D_r/D_p = 0.15$ (Fig. 2.11). Decreasing r_{\max} increases NP adsorption.
- (d) **Varying D_r/D_p :** We plot NP adsorption for $D_r/D_p = 0.02$, $D_r/D_p = 0.045$, $D_r/D_p = 0.15$, $D_r/D_p = 0.3$, and $D_r/D_p = 22.7$ (Fig. 2.12). $r_{\min} = 5$, $r_{\max} = 80$, and $\sigma = 114 \mu\text{m}^{-2}$. We find two different regimes for NP adsorption. For $D_r/D_p = 0.02$ and $D_r/D_p = 0.045$ higher NP concentrations result in higher NP adsorption, for all other values of D_r/D_p the number of bound NPs saturates for high NP concentrations at values that increase with increasing D_r/D_p .

2.2 Simulation of NP adsorption to RBCs

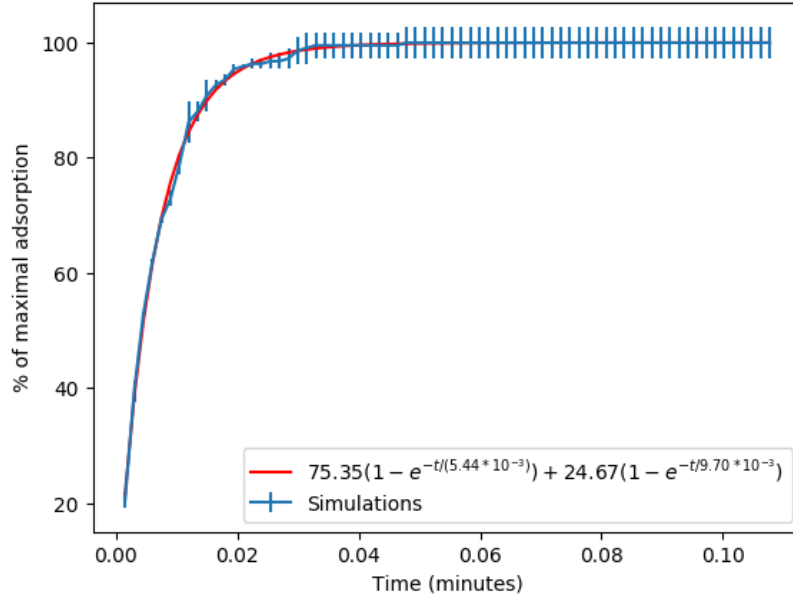


Figure 2.13: Percentage of maximal NP adsorption as function of time for 27 nm NPs at $c_{\text{tot}} = 1 \times 10^{12}/\text{ml}$. We use $\sigma = 114 \mu\text{m}^{-2}$, $D_r/D_p = 0.04$, $r_{\text{min}} = 2$, and $r_{\text{max}} = 60$.

Table 1 summarizes the key quantities for both Brownian dynamics simulations and Langmuir model. We choose the parameters in the simulations, such that the simulation results fit our experimental results for the three NP sizes (Fig. 2.5), and thus extract the parameter sets D_r/D_p , r_{min} , r_{max} , and σ . Assuming a receptor density $\sigma = 114 \mu\text{m}^{-2}$ (obtained from the number of receptors in the simulation divided by the membrane patch area, where the lengths in simulation and experiment are connected via the NP diameters, d_{exp} and d_{sim}), we obtain $D_r/D_p = 0.04$, $r_{\text{min}} = 2$, and $r_{\text{max}} = 60$ for 27 nm NPs, $D_r/D_p = 0.07$, $r_{\text{min}} = 3$, and $r_{\text{max}} = 75$ for 45 nm NPs, and $D_r/D_p = 0.15$, $r_{\text{min}} = 5$, and $r_{\text{max}} = 80$ for 100 nm NPs. However, because the receptor density in the RBC membrane is unknown, matching the time scales for experiment and simulation is difficult (Tab. 2.1). The characteristic times for fast and slow binding kinetics predicted by the simulations are found to be two orders of magnitude shorter than those obtained from the experiments (Figs. 2.13-2.16). Here, time scales in simulations and experiments are connected using $t_{\text{exp}} = (D_{\text{sim}}d_{\text{exp}}^2)/(D_{\text{exp}}d_{\text{sim}}^2)t_{\text{sim}}$, together with typical values of NP diffusion coefficients in experiments (calculated using the Stokes friction of a sphere in water) and simulations as gauge. The receptor density used in our course-grained simulations is lower than typical densities for potential receptors reported in the literature, such as $\sigma = 7300 \mu\text{m}^{-2}$ for Band 3, $\sigma = 350 - 6570 \mu\text{m}^{-2}$ for Glycophorin A (GPA), $\sigma = 365 - 730 \mu\text{m}^{-2}$

Nanoparticle-decorated red blood cells reveal that particle size controls adsorption, cell shape, and cell deformability

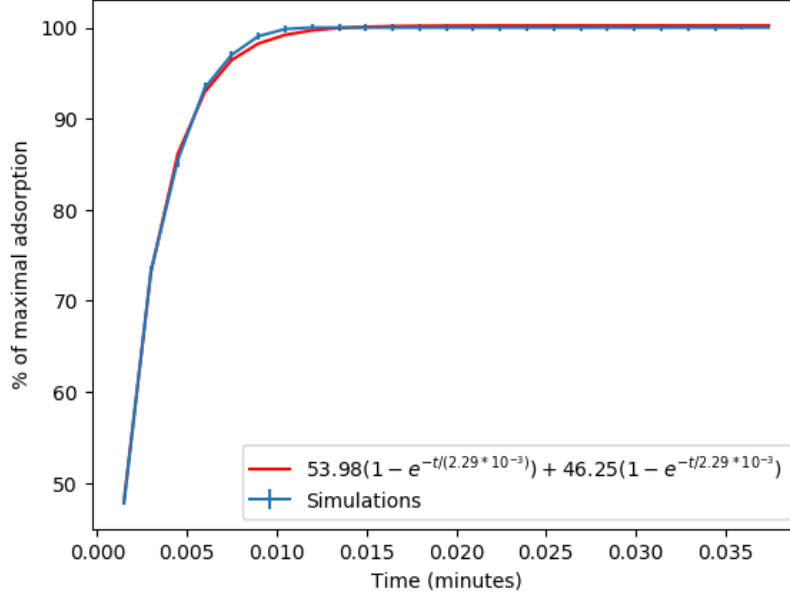


Figure 2.14: Percentage of maximal NP adsorption as function of time for 27 nm NPs at $c_{\text{tot}} = 4 \times 10^{12}/\text{ml}$. We use $\sigma = 114 \mu\text{m}^{-2}$, $D_r/D_p = 0.04$, $r_{\text{min}} = 2$, and $r_{\text{max}} = 60$.

for Glycophorin C (GPC), and $\sigma = 252\,000 \mu\text{m}^{-2}$ for sialic acid residues in the RBC membrane [215–218]. Therefore we expect that our values for r_{min} and r_{max} are smaller than those in the experimental system. Thus, the characteristic times are difficult to compare, because the initial binding probability of a NP scales as $(\sigma r_{\text{NP}}^2)^{r_{\text{min}}}$ and therefore strongly depends on the receptor density σ and the number r_{min} of receptors required for multivalent binding. However, the simulations provide a systematic study of the dependence of the number of bound particles on receptor density, minimal and maximal number of receptors that can bind to a NP, and the ratio of receptor to NP diffusion coefficients (Figs. 2.9–2.12). In particular, our simulations show that in order to successfully interpret the experimental data, multivalent binding is required (r_{min}) and that only a maximal number of receptors can bind to a NP (r_{max}).

2.3 The energetics of receptor-limited NP adsorption to RBCs

The energetics of NP adsorption to RBCs is described using a continuum model to calculate the membrane deformation energy and using a lattice model to calculate the receptor free energy (Fig. 2.8). The deformation energy of the lipid bilayer is

2.3 The energetics of receptor-limited NP adsorption to RBCs

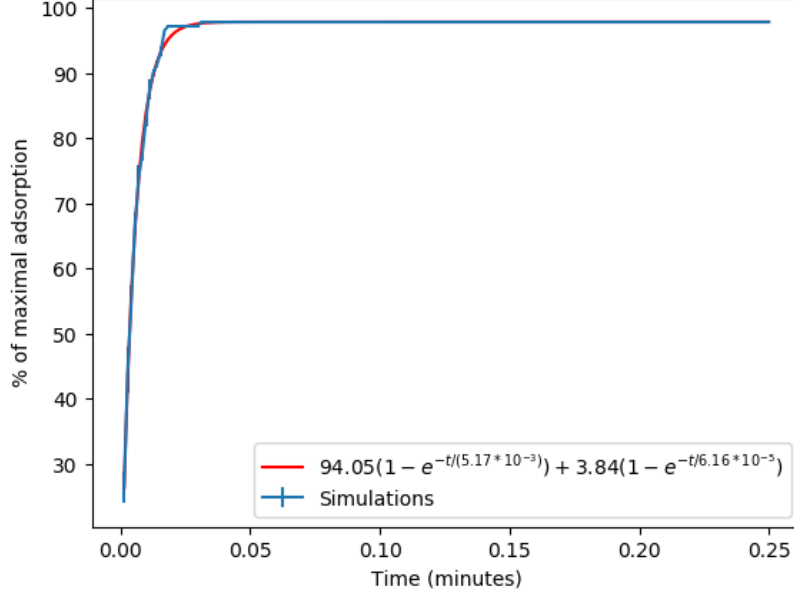


Figure 2.15: Percentage of maximal NP adsorption as function of time for 45 nm NPs at $c_{\text{tot}} = 2 \times 10^{12}/\text{ml}$. We use $\sigma = 114 \mu\text{m}^{-2}$, $D_r/D_p = 0.07$, $r_{\text{min}} = 3$, and $r_{\text{max}} = 75$.

calculated using Helfrich's curvature-elasticity Hamiltonian [93, 96],

$$E_d = \int dA (2\kappa(H - c_0)^2). \quad (2.3)$$

The most important elastic parameters of the membrane in our calculations are the bending rigidity and the spontaneous curvature of the lipid bilayer. The spherical carboxylate surface-modified polystyrene NPs that we study have diameters that are similar to and smaller than the mesh size of the spectrin cytoskeleton, such that we do not expect a direct contribution of the shear modulus of the cytoskeleton to NP adhesion.

The deformation-energy cost for the RBC membrane has to be overcome by the adhesion-energy gain for the contact between the NPs and the membrane. For a homogeneous membrane with vanishing spontaneous curvature and tension, the deformation energy is $E_d = 8\pi\kappa f_w$ per NP, where f_w is the wrapped fraction of the NP surface area. The adhesion energy gain depends on the physicochemical properties of the NP surface, the biochemical composition of the membrane, and the chemical environment provided by the buffer. We calculate the entropy of the receptors by discretizing the membrane into $S = S_b + S_f$ sites on that in total $N = N_b + N_f$ receptors are distributed. The sites on the membrane are divided into S_b sites where N_b receptors can bind to a ligand on a particle and S_f sites where N_f distributed receptors do not bind to a ligand. The total free energy of

Nanoparticle-decorated red blood cells reveal that particle size controls adsorption, cell shape, and cell deformability

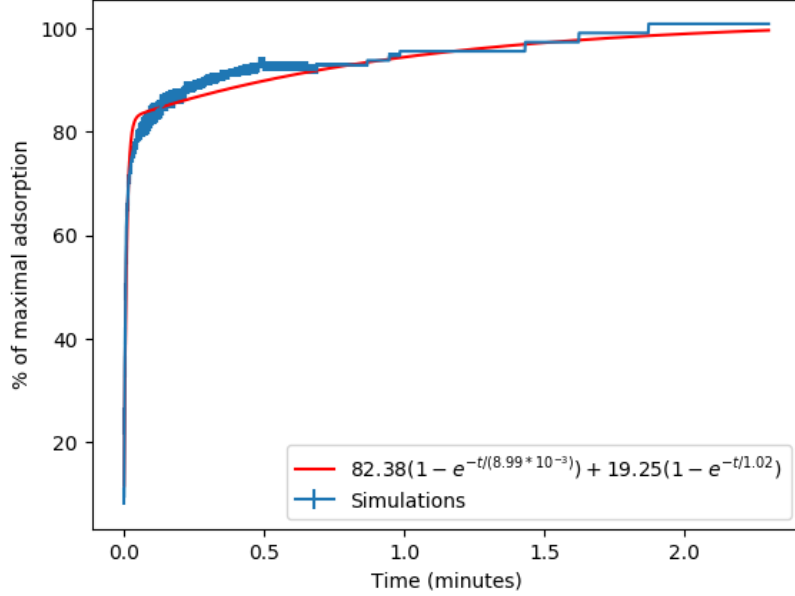


Figure 2.16: Percentage of maximal NP adsorption as function of time for 100 nm NPs at $c_{\text{tot}} = 1 \times 10^{12}/\text{ml}$. We use $\sigma = 114 \mu\text{m}^{-2}$, $D_r/D_p = 0.15$, $r_{\text{min}} = 5$, and $r_{\text{max}} = 80$.

the receptors is then

$$F_r = -N_b U - kT \ln \left(\binom{S_b}{N_b} \binom{S_f}{N_f} \right), \quad (2.4)$$

where $\binom{S_b}{N_b} = S_b! / ((S_b - N_b)! N_b!)$ and $\binom{S_f}{N_f} = S_f! / ((S_f - N_f)! N_f!)$, where the first term is the total binding energy for N_b receptor-ligand bonds with energy U , and the second term is the free-energy contribution due to receptor entropy. We minimize F_r with respect to N_b , and obtain

$$\ln \frac{N_b}{S_b - N_b} + \ln \frac{S - S_b - (N - N_b)}{N - N_b} = U. \quad (2.5)$$

Solving the above equation for number of bound receptors at equilibrium, we obtain

$$N_B = \frac{1}{2(e^{U/kT} - 1)} \left[e^{U/kT} N - N + S - S_B + e^{U/kT} S_B - \sqrt{-4e^{U/kT}(e^{U/kT} - 1)NS_B + (N - e^{U/kT}N - S + S_B - e^{U/kT}S_B)^2} \right]. \quad (2.6)$$

Thus, the number of receptor-ligand bonds for given NP size and wrapping frac-

2.3 The energetics of receptor-limited NP adsorption to RBCs

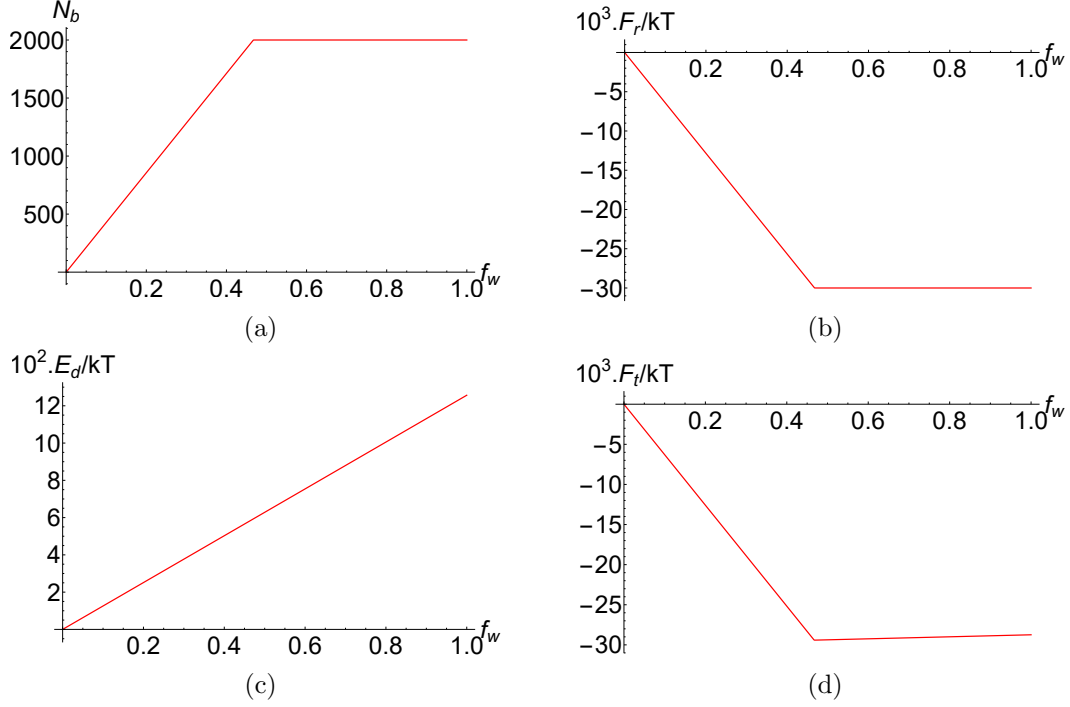


Figure 2.17: (a) Number of bound receptors N_b as function of the wrapping fraction f_w for $N = 2000$ and $U = 15$ kT. N_b saturates when all the receptors are bound. (b) Free energy for receptor binding, F_r as function of f_w for $N = 2000$ and $U = 15$ kT. F_r saturates when all the receptors are bound, (c) Membrane deformation energy E_d as function of f_w for $\kappa = 50$ kT. E_d increases linearly with f_w . (d) Total energy F_t as function of f_w for $N = 2000$ and $U = 15$ kT, and $\kappa = 50$ kT.

tion obtained from the free-energy calculations is

$$N_B = \frac{(A_{\text{RBC}})}{2N_{\text{NP}}A_r(e^{U/kT} - 1)} \left[e^{U/kT} \sigma - \sigma + 1 - f_w + e^{U/kT} f_w - \sqrt{-4e^{U/kT}(e^{U/kT} - 1)\sigma f_w + (\sigma - e^{U/kT}\sigma - 1 + f_w - e^{U/kT}f_w)^2} \right], \quad (2.7)$$

where $\sigma = N/S$ is the membrane receptor density and $f_w = S_b/S$. We plot N_b , F_r , E_d , and total free energy $F_t = E_d + F_r$ as a function of f_w (Fig. 2.17). Assuming that the carboxyl groups on the NPs act as ligands, we calculate areas per ligand of $r = 53 \text{ \AA}^2$ for the 27 nm NPs and $r = 29 \text{ \AA}^2$ for the 45 nm and the 100 nm NPs. We therefore use a typical area per ligand on the NP, $A_r = r = 60 \text{ \AA}^2$ (which corresponds to a circular patch with radius $R_r = 4.4 \text{ \AA}$), as area per site for our model [219]. If every lipid that is in contact with a NP binds to a ligand, the membrane bending energy per receptor is $E_d/N = 8\pi\kappa(R_r^2)/R^2$. The bending energy can be neglected for calculating the receptor free energy if $E_d/N \ll U$,

Nanoparticle-decorated red blood cells reveal that particle size controls adsorption, cell shape, and cell deformability

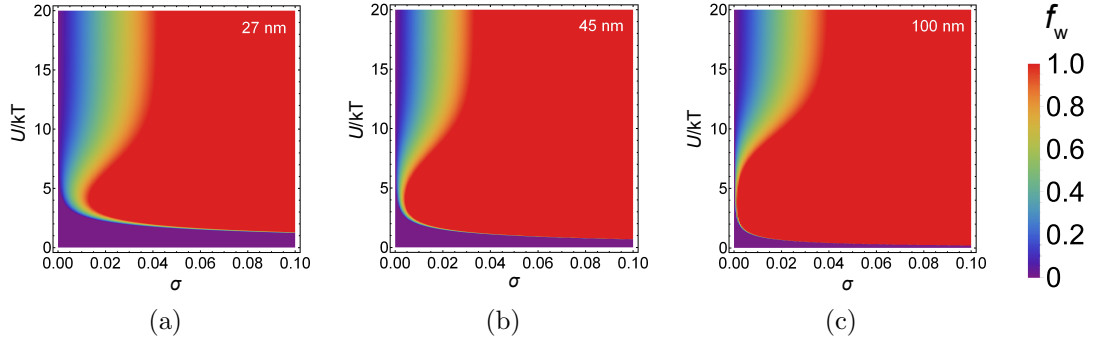


Figure 2.18: Wrapping fractions f_w for (a) 27 nm, (b) 45 nm, and (c) 100 nm NPs as function of the binding energy U and the receptor density σ obtained using Eq. 2.4. Non-wrapped states are obtained for low receptor densities and low binding energies, partial-wrapped states for low receptor densities and high binding energies, and complete-wrapped states for high receptor densities and high binding energies. The complete-wrapping regime extends most to low receptor densities for $U \sim 5$ kT. As U increases, in the low receptor-density regime receptors bind to free sites on particles as soon as they get available and the systems run out of free receptors already for partial-wrapped NPs.

i. e. $R_r/R \ll (U/8\pi\kappa)^{1/2}$. Using $U = 15$ kT [220, 221] and $\kappa = 50$ kT [222, 223], we find $(U/8\pi\kappa)^{1/2} \approx 0.1$ and $R_r/R \approx 0.01$ for the 27 nm NPs. We therefore do not take bending energy into account for calculating the receptor free energy. Minimization of the total free energy F_t as function of f_w with $c_0 = 0$ gives the optimal wrapping state of a NP.

Wrapping fractions of NPs for various receptor densities and receptor ligand-bond energies are shown in Fig. 2.18. The NPs remain unwrapped for small energies per receptor-ligand bond, which is in agreement with previous calculations for NP wrapping using a homogeneous adhesion strength [10, 85]. For very small densities of receptors, the NPs just attach to the membrane basically without any wrapping. Stable partial-wrapped states that we observe in our experiments are found for high receptor-ligand bond energies and for small receptor densities. Complete-wrapped states are found both for higher receptor densities on the membrane, as well as for small receptor-ligand bond energies. While the latter appears to be counter-intuitive, it can be explained by the fact that because of the competition of receptor entropy and receptor-ligand bond energy, the receptors do not bind densely to the NP surface, such that also a smaller amount of receptors is sufficient to wrap the NP completely.

2.4 NP-induced shape changes of RBCs

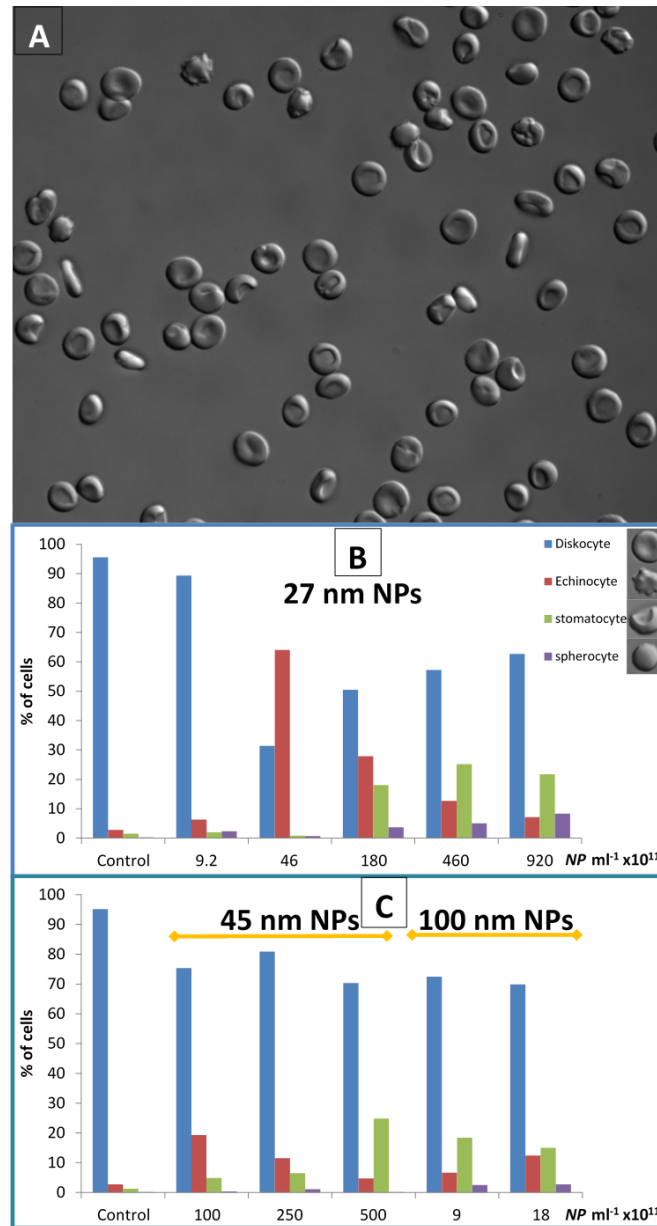


Figure 2.19: RBC shape changes after interaction with NPs of different sizes. (A) Various RBC shapes after adsorption of 27 nm NPs at $c_{\text{tot}} = 10^{14}/\text{ml}$ concentration. (B) Fractions of RBC shapes at various concentrations of 27 nm NPs. (C) Fractions of RBC shapes at various concentrations of 45 and 100 nm NPs.

2.4 NP-induced shape changes of RBCs

A typical shape distribution for RBCs from a healthy donor is 95.5% discocytes, 1.5% stomatocytes, 2.8% echinocytes, and 0.2% spherocytes (Fig 2.19, control).

Nanoparticle-decorated red blood cells reveal that particle size controls adsorption, cell shape, and cell deformability

The biconcave discocytic shape and the corresponding deformability of RBCs are essential for their biological function. This equilibrium shape is sensitive to various environmental and biochemical factors. RBCs undergo shape transformations to spiculated echinocytes, for example, if they are exposed to anionic amphiphilic molecules, and to cup-shaped stomatocytes if they are exposed to cationic amphiphilic molecules [203]. The examination of the consequences following exposure of RBCs to NPs reveals change in the shape distributions of RBCs (Fig. 2.19). The strongest effect is observed for 27 nm NPs: while for NP concentrations of $c_{\text{tot}} = 9.2 \times 10^{11}/\text{ml}$ still most of the cells are discocytes, for $c_{\text{tot}} = 4.6 \times 10^{12}/\text{ml}$ about 64% of the RBCs are echinocytes and only 31% of the cells are discocytes. Upon further increasing the NP concentration, the fraction of echinocytes decreases again, while the fraction of discocytes, stomatocytes, and spherocytes increases. At $c_{\text{tot}} = 9.2 \times 10^{13}/\text{ml}$, 62.8% of the RBCs are discocytes, 21.8% are stomatocytes, 8.3% are spherocytes, and 7.1% are echinocytes. For 45 nm NPs and for 100 nm NPs, about 20 – 30% of the RBCs are not discocytes at concentrations higher than $c_{\text{tot}} = 10^{13}/\text{ml}$ and $9 \times 10^{11}/\text{ml}$ respectively. As for 27 nm NPs, the fraction of echinocytes for 45 nm NPs decreases while the fraction of stomatocytes increases with increasing NP concentration. We have identified three mechanisms by which NP adsorption changes RBC shapes (Fig. 2.23).

2.4.1 NP-induced RBC shape changes via area-difference elasticity

Any mechanism that expands or contracts the inner or outer monolayers of the lipid bilayer relative to each other changes the shapes of RBCs. Substances that increase the area of the outer monolayer are crenators that favor echinocytes, while substances that increase the area of the inner monolayer are cup-formers that favor stomatocytes [81, 102, 203]. With the known relation between area difference of the two layers and membrane spontaneous curvature, we can write the energy of the vesicle determined by the ADE energy functional as [81, 102, 201]

$$F_{\text{ADE}} = \frac{\kappa}{2} \oint dA (2H - c_0)^2 + \frac{\bar{\kappa}\pi}{2AD^2} (\Delta A - \Delta A_0)^2, \quad (2.8)$$

where $D \sim 3$ nm is the distance between the neutral surfaces of the two monolayers [102, 201], A is the membrane area, ΔA_0 is the area difference that corresponds to the discocyte shape, ΔA is the actual area difference induced between the areas of the monolayers, and $\bar{\kappa}$ is the Gaussian saddle-splay modulus. The integral is taken over the entire membrane of the closed vesicle. The area difference between the outer and the inner layer that is induced by N NPs with radius R and wrapping fraction f_w is

$$\Delta A_{\text{NP}} = (4\pi(R + D)^2 - 4\pi R^2) f_w N_{\text{NP}}. \quad (2.9)$$

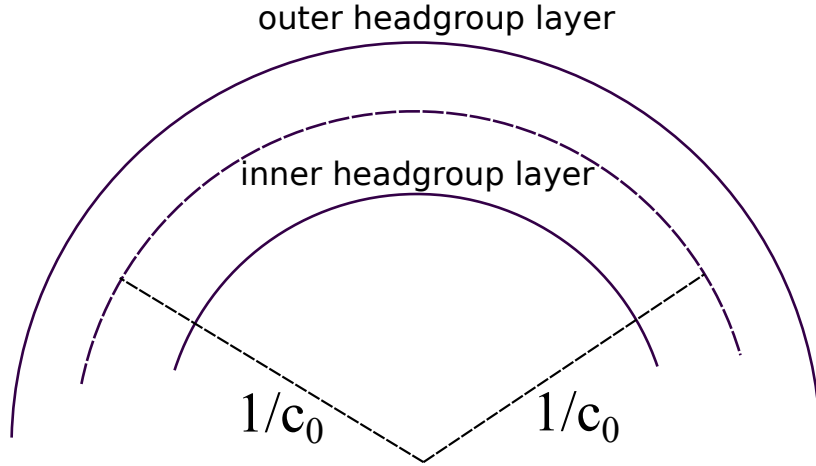


Figure 2.20: An area difference between the two monolayers tends to curve the bilayer membrane. We can fit a circle to the mean layer, the inverse of its radius is the induced spontaneous curvature.

Using $\bar{\kappa}/\kappa = 2/\pi$, we obtain the total spontaneous curvature of the NP-decorated membrane,

$$c_0^{\text{eff}} = c_0 + \frac{2\Delta A_0}{DA} + 16\pi f_w \sigma_{\text{NP}} R \left(1 + \left(\frac{D}{2R} \right) \right), \quad (2.10)$$

where c_0 is the spontaneous curvature of the RBC membrane. Thus, the spontaneous curvature that is induced by the NP-decoration of the RBC is

$$\Delta c_0^{\text{eff}} = 16\pi f_w \sigma_{\text{NP}} R \left(1 + \left(\frac{D}{2R} \right) \right). \quad (2.11)$$

Here, σ_{NP} is the density of NPs on the membrane. We show that the NP-induced spontaneous curvature increases with increasing f_w , σ_{NP} , and R for 45 nm NPs (Fig. 2.23 (b)). The NP-induced spontaneous curvatures for the other NP sizes differ by less than 10% from those plotted, because $0.01 \leq D/2R \leq 0.1$ for all cases. NPs that attach to the outside of RBCs take out more lipids from the inner monolayer than from the outer monolayer and are crenators. Figure 2.20 shows the configuration of the membrane.

2.4.2 NP-induced RBC shape changes via attached spherical caps

Attached spherical caps and conical proteins induce an effective membrane spontaneous curvature, and can aggregate and induce bud formation [59,210,211]. The partial-wrapped NPs in our experiments act as spherical caps and can therefore

Nanoparticle-decorated red blood cells reveal that particle size controls adsorption, cell shape, and cell deformability

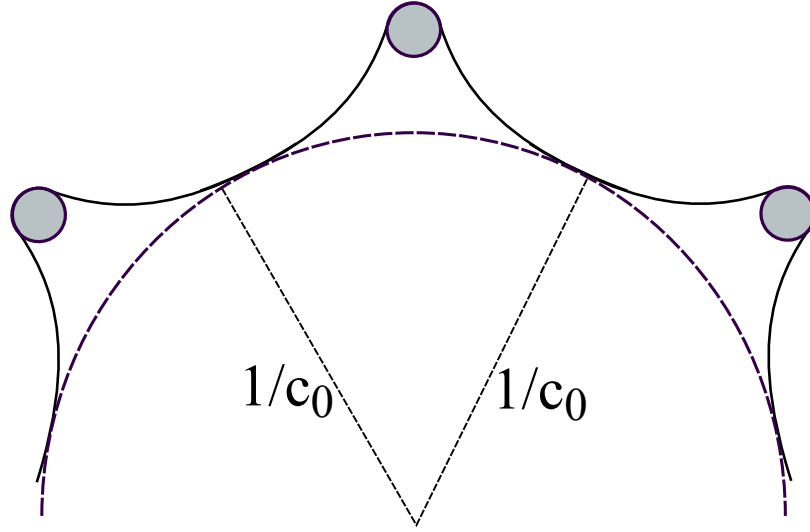


Figure 2.21: A membrane that is effectively curved by attached partial-wrapped NPs.

also induce RBC shape transitions. NPs that attach to the outside of RBCs effectively curve the membrane towards the outside. For small wrapping fractions, the spontaneous curvature that is induced by the NPs is given by [210]

$$\Delta c_0^{\text{eff}} = \frac{-4\pi f_w(1 - f_w)\sigma_{\text{NP}}R}{(1 - 2f_w)}. \quad (2.12)$$

For larger wrapping fractions of NPs, when the membrane cannot be considered to be almost flat anymore, the induced spontaneous curvature has to be calculated numerically. We predict an effective spontaneous curvature c_0 as function of the NP radius R , the wrapping fraction f_w , and the NP density σ_{NP} using geometrical calculations. Within a cylindrically-symmetric approximation, we calculate radius and slope of the outer boundary of the membrane patch. Fitting this to a sphere allows us to determine an effective spontaneous curvature for the NP-decorated membrane, as shown below.

Upon adsorption, the total area of the RBC membrane, $A_{\text{RBC}} \approx 137 \mu\text{m}^2$, can be separated into the wrapped membrane area and the catenoidal patches of the free membrane area around each NP (Fig. 2.21). The geometrical calculations to calculate an effective induced spontaneous curvature for the NP-decorated membrane is sketched in Fig. 2.22. The wrapping angle θ_{f_w} of a NP is determined by

$$\cos \theta_{f_w} = 1 - 2f_w. \quad (2.13)$$

Therefore, we can write the bound membrane area as

$$A_b = 2\pi r_{\text{NP}}^2(1 - \cos \theta_{f_w}). \quad (2.14)$$

2.4 NP-induced shape changes of RBCs

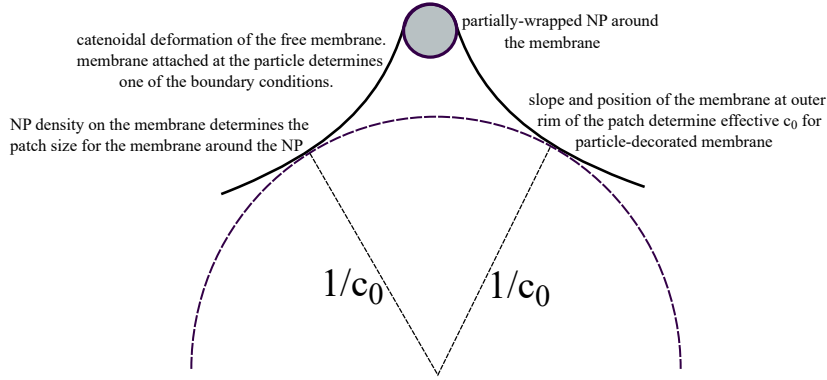


Figure 2.22: The area of a NP-decorated membrane can be divided into the wrapped membrane, and the catenoidal patches of free membrane around each NP. Using the spherical and catenoidal pieces, we can geometrically construct a NP-decorated vesicle and calculate the effective spontaneous curvature.

The total area of a membrane patch to that a NP on the RBC is adhered is $A_{\text{patch}} = A_{\text{RBC}}/N_{\text{NP}}$, where N_{NP} NPs are attached to the RBC. Hence, the free membrane area for each patch is $A_f = A_{\text{patch}} - A_b$. The equation of the spherical cap to which this NP is attached to is

$$f_{\text{cap}} = \sqrt{r_{\text{NP}}^2 - (x - r_{\text{NP}} \cos \theta_{\text{f}_w})^2}. \quad (2.15)$$

Assuming $x = 0$ where the membrane detaches from the NP, radius and slope of the cap at the detachment point are

$$r_{\text{cap}} = r_{\text{NP}} \sin \theta_{\text{f}_w}, \quad (2.16)$$

and

$$m_{\text{cap}} = \tan[\pi/2 - \theta_{\text{f}_w}], \quad (2.17)$$

respectively. We can describe the shape of the free membrane using a catenary,

$$y_c = a \cosh\left(\frac{x - x_0}{a}\right), \quad (2.18)$$

with the slope

$$y_c' = \sinh\left(\frac{x - x_0}{a}\right), \quad (2.19)$$

where a and x_0 are catenary constants. Equating the equation for the catenary equation to equation for the spherical cap at $x = 0$, and the catenary slope to the spherical cap slope, we obtain

$$a = \frac{r_{\text{cap}}}{\sqrt{1 + m_{\text{cap}}^2}}, \quad (2.20)$$

Nanoparticle-decorated red blood cells reveal that particle size controls adsorption, cell shape, and cell deformability

and

$$x_0 = -r_{\text{cap}} \operatorname{arcsinh} \left(\frac{m_{\text{cap}}}{\sqrt{1 + m_{\text{cap}}^2}} \right), \quad (2.21)$$

Furthermore, we calculate the surface area of the catenoidal patch and by integrating from the position where the membrane detaches from the NP, x_{NP} , to the position where it meets the vesicle, x_{patch} ,

$$A_c = \frac{\pi a}{2} \left(2x_{\text{patch}} + a \sinh \left(\frac{2(x_{\text{patch}} - x_0)}{a} \right) - a \sinh \left(\frac{-2x_0}{a} \right) \right). \quad (2.22)$$

Equating the catenoidal area A_c to the free membrane patch area A_f , we determine x_{patch} . Fitting a circle to the outer boundaries of the catenoidal membrane patch where the catenoid intersects the vesicle, and determining the position and the slope of the circle at the contact point, y_{patch} , and m_{patch} , we obtain r_{patch} , the radius of the fitted circle. The spontaneous curvature of the NP-decorated membrane is the inverse of r_{patch} ,

$$c_0 = \frac{2}{\left(\sqrt{1 + m_{\text{patch}}^2} y_{\text{patch}} \right)}, \quad (2.23)$$

where the factor 2 in the numerator has been introduced to be consistent with the Helfrich Hamiltonian. We show that the NP-induced spontaneous curvature is maximal for half wrapping, $f_w = 0.5$, and that it increases with increasing σ_{NP} and R (Fig. 2.23 (c)). The plot is universal and independent of the NP size, we have marked the spontaneous curvature contributions for the three NP sizes used for our experiments at their saturation density. Via the attached spherical-cap mechanism, partial-wrapped NPs act as cup-formers.

2.4.3 NP-induced RBC shape changes via reduced volume

Healthy RBCs have reduced volumes $v = 6\sqrt{\pi}V/A^{3/2} \approx 0.66$ with $V = 100 \mu\text{m}^3$ and $A = 137 \mu\text{m}^2$ [102].² Both, shape calculations that take into account the shear elasticity of the spectrin cytoskeleton and lipid bilayer-only calculations for vesicles predict shape transitions for changes of the reduced volume, e.g. for osmotic swelling of RBCs [79, 224, 225]. Upon complete uptake of NPs by wrapping, the volume of the erythrocyte increases while the area of its plasma membrane decreases. For partial uptake, we find an effective reduced-volume increase

$$v^{\text{eff}} = 6\sqrt{\pi} \frac{V + \Delta V}{(A - \Delta A)^{3/2}}, \quad (2.24)$$

²The reduced volume is the actual volume of a RBC divided by the volume of a sphere with the same surface area

2.5 NP-induced deformability changes of RBCs

with the effective volume increase

$$\Delta V = N_{\text{NP}} \frac{\pi}{3} 4R^3 f_w^2 (3 - 2f_w), \quad (2.25)$$

and the effective plasma membrane-area decrease

$$\Delta A = N_{\text{NP}} (A - 4\pi R^2 f_w^2)^{3/2}. \quad (2.26)$$

Here, N_{NP} is the number of NPs adsorbed to a RBC. Thus, upon NP adsorption, the effective reduced volume of a RBC,

$$v^{\text{eff}} = 6\sqrt{\pi} \frac{V_{\text{RBC}} + N_{\text{NP}} V_{\text{NP}} f_w^2 (3 - 2f_w)}{(A_{\text{RBC}} - N_{\text{NP}} A_{\text{NP}} f_w^2)^{3/2}}, \quad (2.27)$$

will increase because the membrane area effectively decreases while the volume effectively increases when partial-wrapped NPs protrude into the cytosol. NPs that attach to the outside of RBCs effectively increase their reduced volume and lead to spherocytes at sufficiently high densities (Fig. 2.23 (d)). The large increase of the effective spontaneous curvature predicted for the NP-induced area difference, as well as the small decrease predicted for the spherical-cap effect, are consistent with the spontaneous-curvature changes required to explain the observed shape changes in our experiments (Fig. 2.19) [102]. While the large increase of the effective spontaneous curvature due to area-difference elasticity can easily explain echinocytes, this effect is expected to dominate over the spherical-cap effect also for high NP concentrations. The decrease of echinocytes and the increase of stomatocytes with increasing NP concentrations therefore hint that the area difference relaxes due to flip-flop of lipids, possibly facilitated by the distortion of the bilayers by the NPs [226–228]. Spherocytes occur because of an increase of the volume and/or a decrease of the membrane area which may occur due to osmotic swelling [224, 229, 230], shedding of membrane [231], and endovesiculation [232]. Furthermore, spherocytes are the endpoints of both stomatocytic as well as echinocytic deformations and may occur via one of these shape-deformation pathways [233].

2.5 NP-induced deformability changes of RBCs

RBCs experience shear stresses during blood circulation with shear rates of the order of 100 – 1000 Hz and have to squeeze through small capillaries in order to deliver oxygen to body tissues [234–238]. Therefore, their ability to deform is crucial for proper physiological function. We have tested RBC deformability before and after NP adsorption at different concentrations using a hemorheometer (RheoScan AnD-300). The RBC suspension in a media containing polyvinylpyrrolidone (PVP) with a viscosity of about 33 mPa is flown

Nanoparticle-decorated red blood cells reveal that particle size controls adsorption, cell shape, and cell deformability

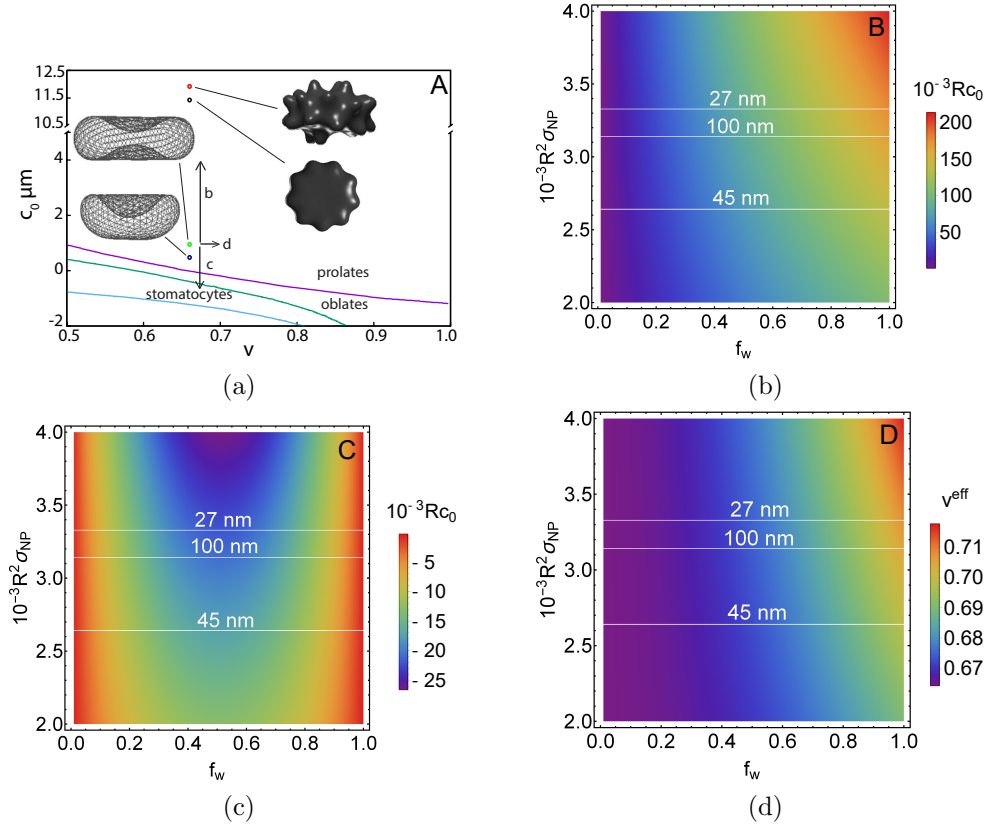


Figure 2.23: Mechanisms for shape changes of erythrocytes. (a) Shapes of erythrocytes and vesicles for various values of the spontaneous curvature c_0 and reduced volume v . The lines mark the boundaries between prolate, oblate, and stomatocytic vesicles based on Ref. [79]. We mark various RBC shapes for the parameters reported in Ref. [102]. The arrows b, c and d indicate the effect of c_0 and v on the RBC shape, respectively. The corresponding subfigures show (b) the NP-induced reduced spontaneous curvature Rc_0 as function of $R^2\sigma_{\text{NP}}$ and f_w from our area-difference elasticity calculations, (c) the NP-induced reduced spontaneous curvature Rc_0 as function of $R^2\sigma_{\text{NP}}$ and f_w induced by curved inclusions, and (d) the effective reduced volume v^{eff} as function of $R^2\sigma_{\text{NP}}$ and f_w , where R is the NP radius and σ_{NP} is the NP density on the RBC. Horizontal lines represent the sizes of NPs used in the experiments. The RBC shapes reproduced with permission from Ref. [102]. Copyright (2002) National Academy of Sciences.

through a thin chamber under altered pressure. The RBC deformation is estimated by measuring the geometry of the diffraction patterns of the RBC suspension (Fig. 2.24). Significant RBC stiffening was observed only for 27 nm NPs at very high concentrations of $c_{\text{tot}} = 5 \times 10^{13}/\text{ml}$ and $10^{14}/\text{ml}$. Larger NPs of 45 nm and 100 nm were almost without effect on RBC deformability even at the highest

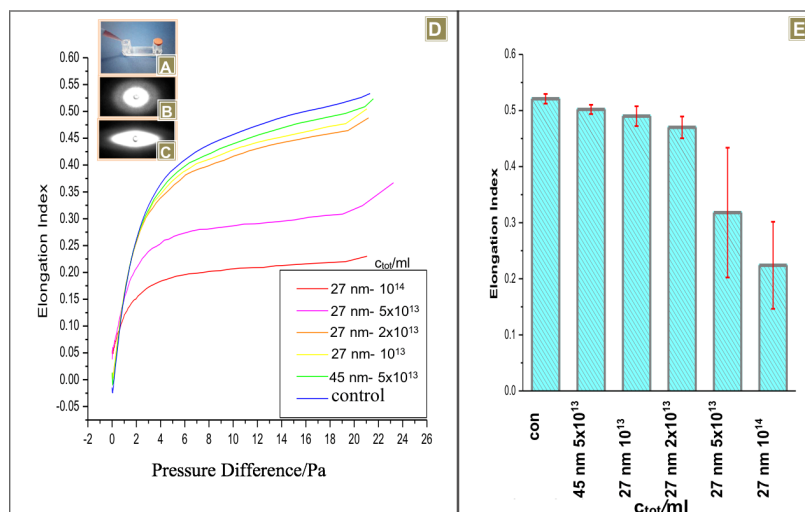


Figure 2.24: RBC deformability accessed by RheoScan AnD-300 hemorheometer as a function of NP concentration. A measurement chamber; B typical diffraction image of cells at low pressure; C typical diffraction image at 20 Pa. D RBC deformation curves at different NP concentrations. Each curve average of at least 3 independent experiments, each in triplicates. E Elongation Index of RBC at 20 Pa.

concentrations studied. This correlates with the shape transformations of RBCs where 27 nm NPs at high concentrations were most effective in inducing stomatocytes and spherocytes in RBC populations. In agreement with our findings, stomatocytes have been reported to be much less deformable than discocytes in experiments with optical tweezers [239, 240].

2.6 Conclusions and Outlook

Our combined experimental, theoretical, and computer-simulation work suggests that the NPs bind to adhesive sites on the RBC membrane. The experimentally observed lack of detachment of NPs hints that the concentration dependence is determined by a kinetic mechanism. Our Brownian dynamics simulations suggest that multivalent binding is required and that only a limited number of receptors can bind to a NP. The dependence of the number of bound NPs on the NP concentration in suspension can thus be described using both Langmuir isotherms and taking into account for the irreversible binding of the NPs observed in the experiments our Brownian dynamics simulations.

Partial-wrapped NP states may be further stabilized by hindrance of NP wrapping by the spectrin cytoskeleton. Both, the sparse coverage of RBCs with

Nanoparticle-decorated red blood cells reveal that particle size controls adsorption, cell shape, and cell deformability

NPs in the experiments and free-energy minimization support that in our system only a small number of adhesive sites which strongly bind to NPs is present in the membrane. Because the mechanics of RBCs has been studied in detail in the past, our experiments and theory furthermore allow to a quantitative prediction of mechanisms by which the attached NPs alter the spontaneous curvature of cell membranes. Partial-wrapped NPs that are attached to the outside of RBCs act as crenators via the area-difference elasticity mechanism, while they act as cup-formers via the spherical-cap mechanism. Furthermore, NPs that are attached to the outside of RBCs effectively decrease the area of the RBC membrane and increase the volume of the cell and thereby increase the reduced volume of the cell and make RBCs more spherical.

Our results are of direct relevance for understanding mechanisms that can be applied in drug delivery and nanotoxicology, and they provide also a solid and systematic basis to study more complex systems. Because NPs can be highly reactive in adsorbing small molecules and macromolecules from their immediate environment, the formation of a so-called protein corona has to be taken into account for most applications involving biological systems [153,241]. The chemical composition of a NP corona can be of temporal nature, as it is a function of the abundance and chemical affinities of competitive adsorbing entities to the NPs' surface [153]. Within our model, a corona can be taken into account through an effective NP size and effective NP-membrane adhesive interaction. Systematic experimental studies to identify these effective parameters for each system are required to connect our generic study with more complex biological environments. While red blood cells do not have active uptake mechanisms, quantitative studies that differentiate between passive adhesion and uptake, and active, metabolic uptake processes for the interaction of NPs with other mammalian cells is a challenge for future studies.

Chapter 3

Wrapping of polymeric nanostructures by neurons

Don't give up on your dreams, keep on sleeping.

– Higgs Boson (2012 – present)

Engineering of neural interfaces is crucial for the development of long-lasting neural prosthesis and brain-computer interfaces [242,243]. Microelectrodes would couple to cell membranes, and record electrical signals emanating from cells. A schematic of a microelectrode is shown in Fig. 3.1. The current will flow from inside the cell to the electrode as shown by the electronic circuit. An efficient microelectrode should have a high signal-to-noise ratio. Thus, the major aims are to maximize the current passing through the electrode and to minimize the current passing through the solution between the cell membrane and the electrode, in order to obtain the maximal signal-to-noise ratio for the neuronal signal [244]. The junctional membrane resistance R_j and the electrode resistance R_e should be low, while the seal resistance R_{seal} should be high [245]. How the cells couple to nanostructures, and how the electrode geometry influences cell adhesion and engulfment-like processes of the 3D structures are some of the important aspects to consider while designing optimal MEA geometries. Microelectrode arrays (MEAs) with spine-shaped, rod-shaped, or mushroom-shaped 3D electrodes are employed for electrophysiological recordings to improve cell adhesion [246,247].

The investigation of the cell-electrode interface remains a big challenge for understanding how cells attach and respond to the device surface. Different mechanisms mediate the interactions between the cell and the substrate, like surface topography and its chemico-physical properties, and cytoskeletal dynamics. Perhaps the simplest way in which substrate nanotopography influences the cell response is the increase of the available surface area [248]. Cells cultured on a nanostructured surface have to expose an increased proportion of their membrane creating a larger contact area for adhesion complexes to attach to and internalize the 3D structures.

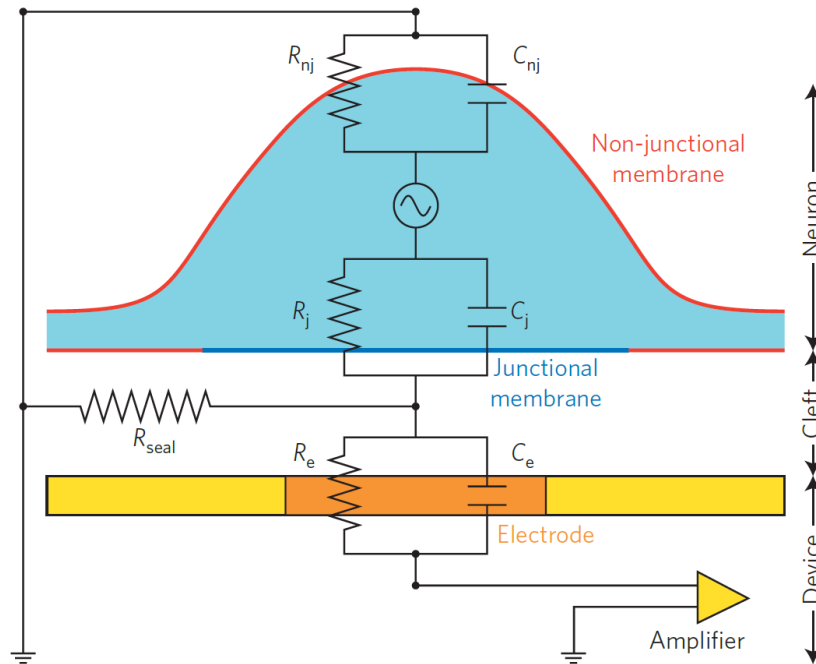


Figure 3.1: Schematic layout depicting the spatial relationships between a neuron and a substrate-integrated electrode and the analogous passive electrical circuit. The cell body of a neuron (light blue) resides on a sensing electrode (orange) integrated in the culture substrate (yellow). The electrode is coupled to an amplifier (yellow). A cleft filled by the culturing media (ionic solution) separates the cell membrane from the electrode substrate. The neuron's plasma membrane is subdivided into two regions: the area that faces the electrode (blue) is defined as the junctional membrane and is represented by the junctional membrane resistance (R_j) and the junctional membrane conductance (C_j). The rest of the membrane, defined as the non-junctional membrane (red), faces the bathing solution and the culture substrate. This part of the membrane is represented by the non-junctional resistance (R_{nj}) and the non-junctional capacitance (C_{nj}). The physiological solution within the cleft generates the seal resistance (R_{seal}) to ground. The electrode (orange) impedance is represented by the electrode resistance and capacitance (R_e and C_e , respectively). The electrode can be a passive element or a transistor. For simulation purposes of action potentials or intracellular current injections, current can be injected into the analogue cell-circuit in-between R_{nj} and R_j . Under physiological conditions current is generated by transient changes in the membrane conductances. Reproduced from Ref. [245].

Nanowire arrays and cylindrical pillars with and without a cap pose as potential candidates to study cell-substrate adhesion [249, 250]. It has been reported that stiffer cells have higher penetration efficiency, but are more sensitive to

Array design	Name	Diameter/ μm	Pitch/ μm
Arrays with pitch double the diameter	A0.25	0.25	0.5
	A0.5	0.5	1
	A0.75	0.75	1.5
	A1	1	2
	A2	2	4
Arrays with constant pitch	B0.25	0.25	1
	B0.5 = A0.5	0.5	1
	B0.75	0.75	1

Table 3.1: Dimensions of the nanostructure designs used in the experiments. The height of all nanopillars is 100 nm.

nanowire geometry, while softer cells have lower penetration efficiency, but are less sensitive to nanowire geometry [249]. However, a problem with nanowire arrays is that they penetrate the cell and thus pose a risk to the cell viability. Santoro *et al.* predict optimal shapes and dimensions of 3D microstructures for cell-chip coupling via a combination of electron microscopy and a continuum membrane deformation model [250]. The microstructures used in the study are large compared with the thickness of a cell membrane. Here, the microstructures do not penetrate the cell, but rather the membrane wraps them, thus avoiding the problem of cell penetration. However, they studied cell-substrate interaction at a single-pillar level, while we go one step beyond, because we look at nanopillar arrays. We use large arrays of three-dimensional (3D) vertically-aligned nano- and micropillars for a comprehensive *in vitro* study of the interactions of primary cortical neurons.

The interaction of cells with nano- and microstructured substrates can be investigated using standard techniques, such as fluorescence microscopy [251], surface plasmon resonance microscopy [252], or electron microscopy [253–255]. In particular, fluorescence microscopy, high-resolution Scanning Electron Microscopy (SEM), and Focused Ion Beam-Scanning Electron Microscopy (FIB-SEM) are used for quantification of neuronal adhesion, for surface characterization, and for studying cell-substrate interfaces. FIB-SEM is a powerful and efficient technique to image cell adhesion to substrates and its interaction with nanopillars in three dimensions. This work is done in collaboration with the Institute of Complex Systems: Bioelectronics (ICS-8) at Forschungszentrum Jülich. All the experiments, viz., fabrication and surface characterization of the MEAs, have been performed by Andreea Anamaria Belu, details can be found in Ref. [248].

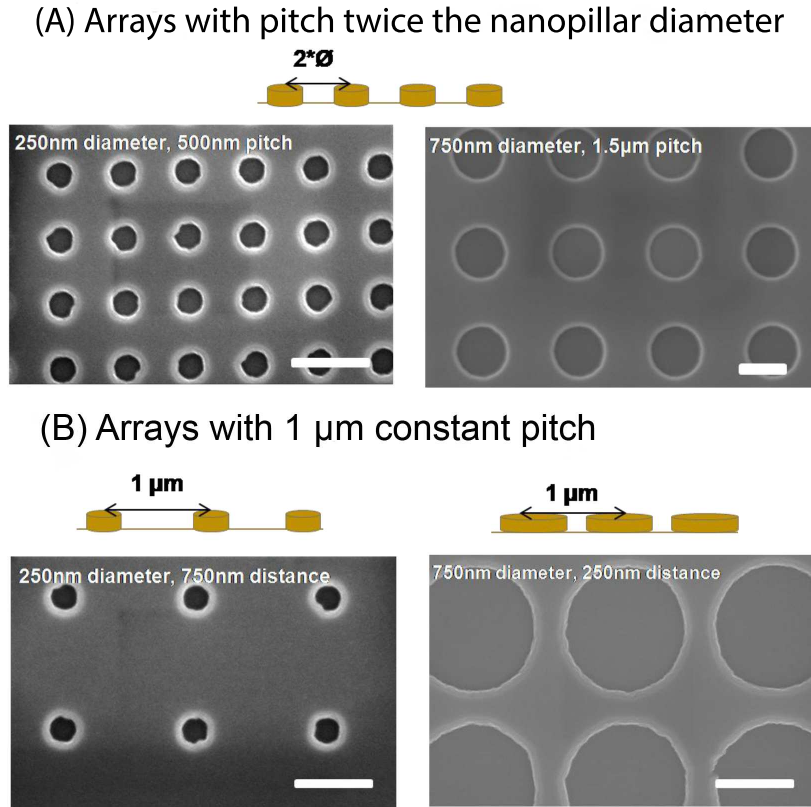


Figure 3.2: Representative schematic and SEM pictures for A) arrays with a pitch double the nanopillar diameter and B) arrays with a constant pitch of 1 µm. The scale bars correspond to 500 nm.

3.1 Exploring the cell-nanostructure interface

Nano- and micropillar arrays consisting of vertical pillars with 100 nm height are used for investigating structured surface-cell interactions. Arrays with two types of geometries are studied: (i) square arrays with the pitch twice as large as the diameter of the nanopillar, here referred to by “A” followed by the pillar diameter in µm, (ii) square arrays with a constant pitch of 1 µm and varying diameters of the nanopillars, here referred to by “B” followed by the pillar diameter in µm, see Tab. 3.1 for details. Representative schematics and SEM images for both types of arrays are shown in Fig. 3.2. The pitch is the interpillar distance measured from center to center. Neurons are cultured on an OrmoComp surface. Filopodia mainly interact with the top of the pillars and with the upper pillar edges (Fig. 3.3).

The nanopillars are cylinder-like and all calculations are performed assuming perfect cylindrical geometry. The relative increase of the surface area compared

3.1 Exploring the cell-nanostructure interface

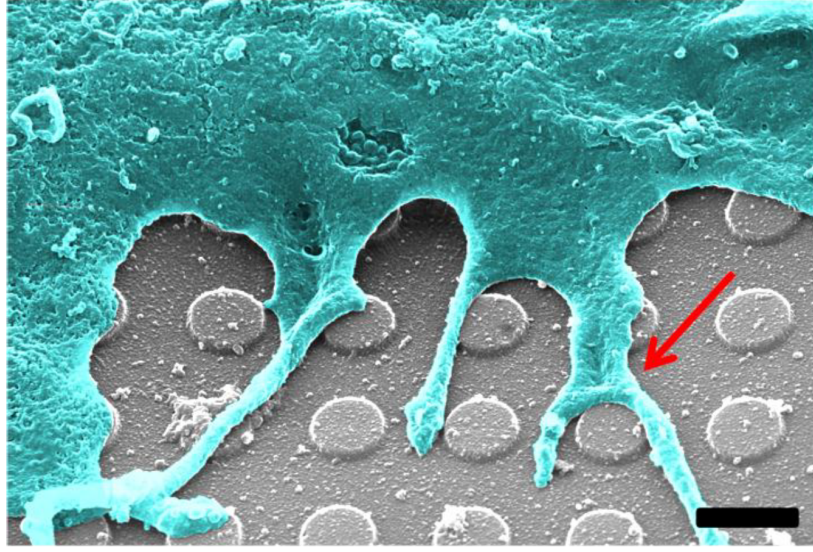


Figure 3.3: SEM micrograph of a neuron cultured on 100 nm high nanostructures. Wrapping of the nanopillars by the neuron is mostly observed at the top of the pillars (red arrow). The scale bar corresponds to 1 μm .

to the flat surface is

$$A_{\text{adh}} = \frac{A_{\text{nanostructure}}}{A_{\text{projected}}} = \frac{A_{\text{nanopillar}}}{l^2} + 1, \quad (3.1)$$

where l is the pitch, $A_{\text{nanopillar}} = 2\pi rh$, the lateral surface area of the pillars, and r and h denote radius and height of the nanopillars, respectively. As an example, the A1 pattern (1 μm diameter, 2 μm pitch) has a surface-area increase of 8% compared to the flat surface.

3.1.1 Arrays with pitch twice the nanopillar diameter

High-resolution FIB-SEM images of the cell-nanostructure interface are shown in Fig. 3.4. For the smallest dimensions (A0.25 array), the cell membrane does not bend into the space between the nanopillars, but rather attaches only to the top of the nanopillars. From A0.5 onwards, the cell membrane shows an increased interaction with the bottom surface.

A quantitative analysis of the cell-membrane interaction with several nanostructures is shown in Fig. 3.5. The cell membrane is divided into four categories: (i) membrane not in contact with the surface - “rest membrane”, (ii) membrane in contact with a pillar’s top face - “top contact”, (iii) membrane in contact with the flat surface between the pillars - “bottom contact”, and (iv) membrane between the pillars - “bending membrane”. “Bending membrane” can be in contact with a pillar’s sidewalls, or suspended between the pillars.

Wrapping of polymeric nanostructures by neurons

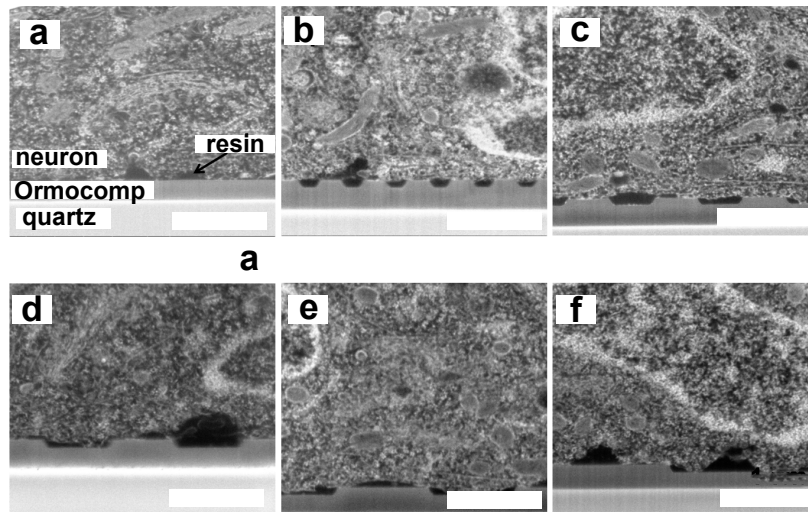


Figure 3.4: FIB-SEM images of (a) a flat surface and (b-f) nanostructures interacting with neurons. The cell-membrane interactions vary with the nanopillar dimensions: (b) A0.25, (c) A0.5, (d) A0.75, (e) A1, and (f) A2. For all structures, the pitch is double the diameter of the nanopillar. The scale bars correspond to 1 μm .

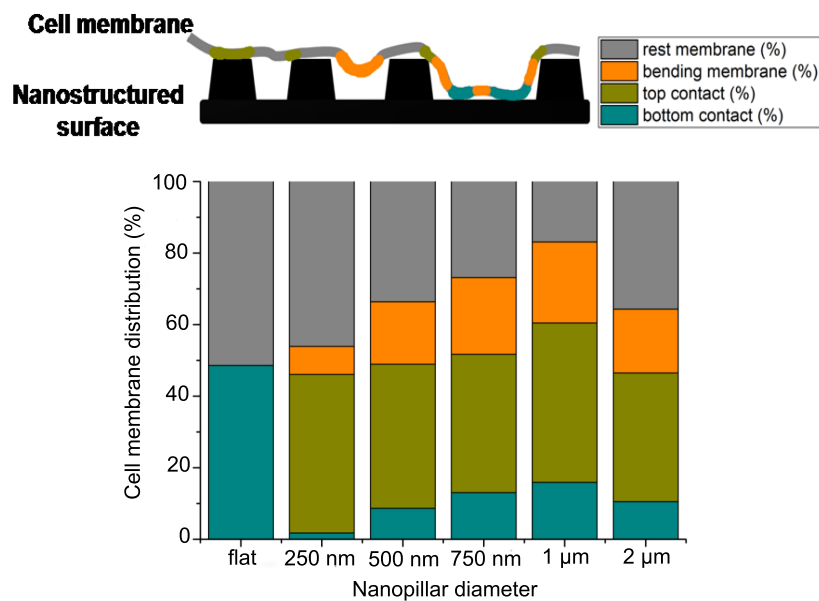


Figure 3.5: Quantification of the surface topography effects on the cell-surface adhesion contact. The cell-membrane interaction with the nanostructure is shown for different nanopillar radii. The pitch is twice the diameter of a nanopillar.

3.1 Exploring the cell-nanostructure interface

A different degree of wrapping of the nanostructure by the cell is found for different interface geometries. We find membrane-surface contact of 48.6% of the total membrane area for flat substrates. For $A0.25$ arrays, the membrane interacts preferentially with the top faces of the pillars (33.2%), exhibits low bending (7.8%) and rarely contacts the bottom surface between the pillars (1.7%). Also in the case of the $A0.5$ array the top contact dominates (26.7%), but we as well observe an increase in bending (17.4%) and bottom contact membrane area (8.6%). Increasing the structure size further, for $A0.75$ arrays we measure almost equal areas to the pillars' top contact area (26.5%) and bending membrane (21.5%). The contact with the bottom surface between the pillars also increases to 13%. For $A1$ nanostructures, we obtain the best membrane-surface interaction: 33.1% top contact, 15.9% bottom contact, 22.6% bending, and only 28.3% rest membrane. The fraction of the adhered membrane again decreases for the largest structure size, $A2$. Although the $A2$ array induced an equal distribution for the membrane contact (18.4% top contact, 17.8% bending, and 10.5% bottom contact), it does not increase the the cell-substrate contact area further because A_{adh} is less for $A2$ compared to $A1$.

3.1.2 Arrays with constant pitch of $1\ \mu\text{m}$

We now consider the second type of array geometry, nanopillars with increasing diameter but constant pitch of $1\ \mu\text{m}$. The contact of cell membranes with nanostructured surfaces is shown in Fig. 3.6. Small interpillar distances ($B0.75$) do not induce membrane bending (Fig. 3.6(b)), while large interpillar distances ($B0.25$) show distinct bending of the cell membrane between the pillars, and an increased bottom contact compared to the other two nano-patterned surfaces (Fig. 3.6(d)).

Figure 3.7 quantifies the cell-membrane interaction with the surface. We find the largest fraction of the adhered membrane for the $B0.25$ array: 15.1% top contact, 27.9% bottom contact, and 40.9% bent membrane. For $B0.75$, the membrane adheres mostly to the top part of the pillars (52.9%), while the bending (7.1%) and the bottom contact area (1.7%) are minimal. For the $B0.5$ array 26.7% top contact, 17.4% bending membrane and bottom contact 8.6%. Hence, cell adhesion is increased for $B0.25$ and $B0.75$ arrays, while $B0.5$ shows similar adhesion values as for a flat surface. Because of the membrane bending contributions to the membrane free energy, it is also interesting to characterize the bending membrane for the three topographies. The fraction of the bent membrane increases 17 times for $B0.25$ array compared to $B0.75$.

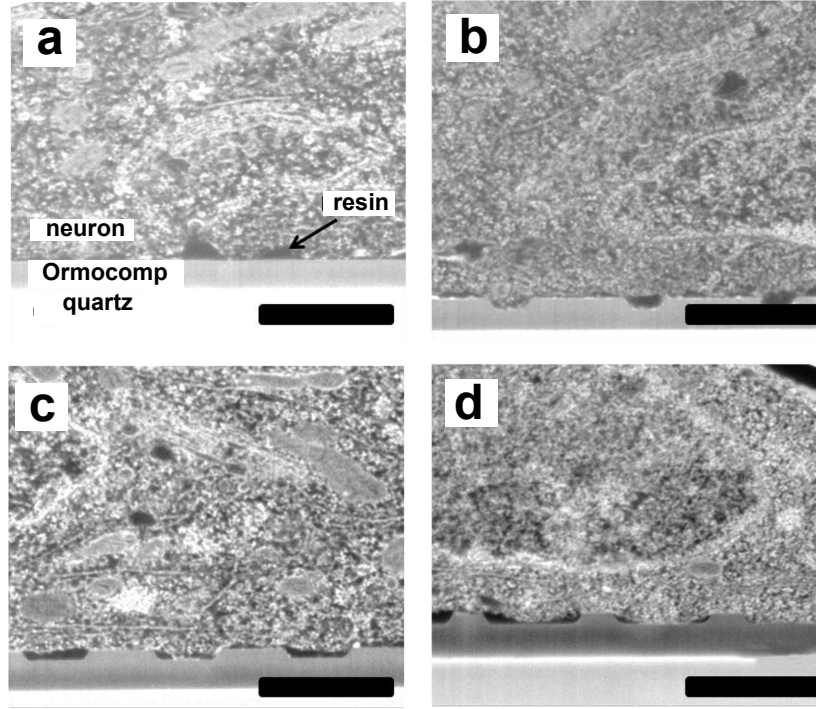


Figure 3.6: FIB-SEM images of (a) a flat surface and (b-d) nanostructures interacting with neurons. The cell-membrane interactions vary with the nanopillar dimensions: (b) $B0.75$, (c) $B0.5$, and (d) $B0.25$. The pitch is $1\ \mu\text{m}$ for all the structures. The scale bars correspond to $1\ \mu\text{m}$.

3.2 Theoretical modelling of nanostructure wrapping

We theoretically model the wrapping of the nanostructure by the cell membrane using the continuum membrane model introduced in Chap. 1. For this, we take into account nanopillar height, radius and pitch, and membrane bending energy, membrane-substrate adhesion strength, and surface- and line-tension contributions. The total energy of the lipid bilayer membrane is the sum of deformation energy E_d and adhesion energy E_{adh} [93],

$$E_d + E_{\text{adh}} = \left[\int_{A_{\text{total}}} dA \left(\frac{\kappa}{2} (2H - c_0)^2 + \sigma \right) + \gamma \int_{\text{line}} dl \right] - w \int_{A_{\text{adh}}} dA, \quad (3.2)$$

with line tension γ . The line tension contribution arises from the sharp membrane bending at the top as well as the bottom edge of the nanopillars. As usual, we assume that $c_0 = 0$. A contribution of the shear modulus of the cytoskeleton on nanopillar adhesion is neglected, as the sizes of our nanostructures are relatively small compared to the cytoskeletal mesh size for neurons [256, 257].

3.2 Theoretical modelling of nanostructure wrapping

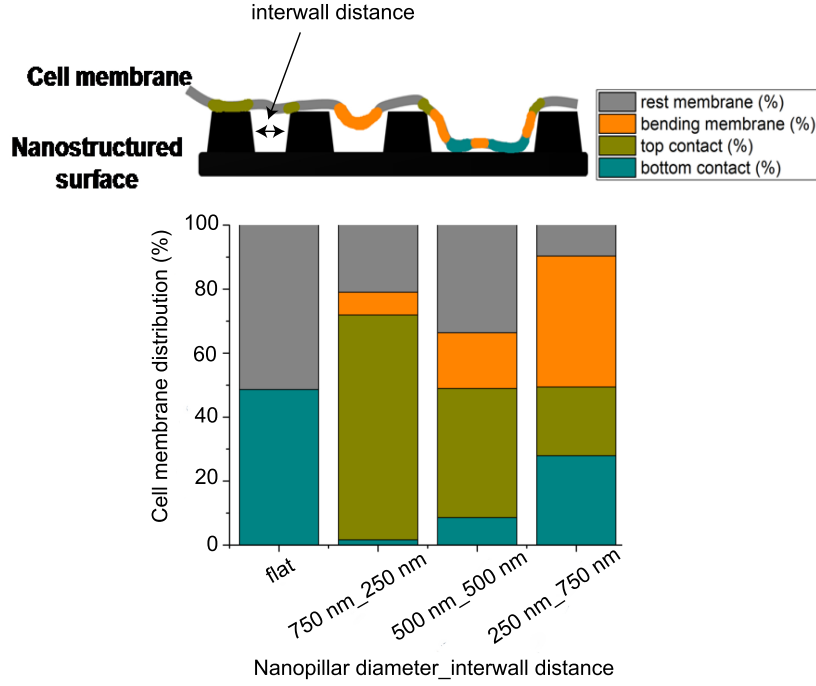


Figure 3.7: Quantification of the surface topography effects on the cell-surface adhesion contact. The cell-membrane interaction with the nanostructure is shown for different nanopillar radii. The pitch is $1 \mu\text{m}$ for all surfaces.

For a patch of the nanostructured substrate of size $l \times l$, radius r and height h of the nanopillar, pitch l , and wrapped nanopillar height z , we obtain (Fig. 3.8),

$$E_d = \frac{\pi\kappa z}{r} + \sigma(l^2 + 2\pi r z) + 4\pi r \gamma, \quad (3.3)$$

and

$$E_{\text{adh}} = \begin{cases} -w(\pi r^2 + 2\pi r z), & \text{for partial wrapping} \\ -w(l^2 + 2\pi r h), & \text{for complete wrapping} \end{cases}. \quad (3.4)$$

We include the deformation-energy contribution of the free membrane between pillars in the line tension term in Eq. 3.2. We further introduce the wrapping fraction f_w for the nanostructured surface, which is given by the ratio of the adhered nanopillar area to the total surface area of the nanostructured substrate,

$$f_w = \frac{\pi r^2 + 2\pi r z}{l^2 + 2\pi r h}. \quad (3.5)$$

By calculating membrane-deformation energy, adhesion energy, and membrane-tension and line-tension contributions, we obtain wrapping transitions from non-wrapped to partial-wrapped and to complete-wrapped states.

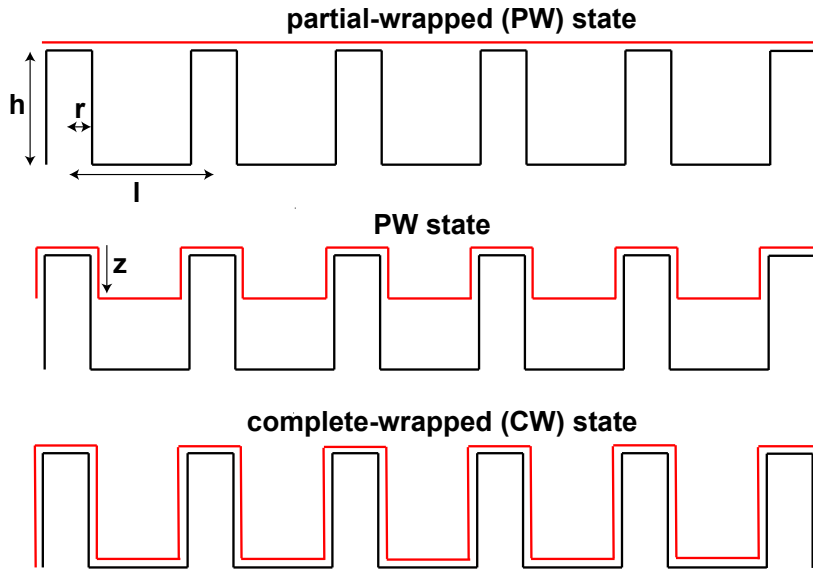


Figure 3.8: Schematic representation of a partial-wrapped (PW) and complete-wrapped (CW) states for nanopillar geometries, with radius r of the nanopillar, pitch l , height h , and wrapped nanopillar height z .

3.2.1 Wrapping transitions

Minimization of the total energy $E_t = E_d + E_{\text{adh}}$ as function of f_w gives the wrapping state of a nanopillar. For constant σ , l , r , h , and for vanishing γ (as the line tension contribution is minimal [258,259]), we first calculate deformation energies as function of f_w and then add the adhesion energies for various values of w . We obtain no wrapping for $w = 0$, where the membrane is hovering above the nanopillars. For small values of $w > 0$, the membrane covers only the top surface of the nanopillars, characteristic to a partial-wrapped (PW) state. Increasing the adhesion strength further leads to the envelopment transition from a PW state to the complete-wrapped (CW) state at adhesion strength w_2 . For $0 < w < w_2$, we obtain stable PW states. For $w > w_2$, a stable CW state is obtained. A schematic representation of a nanopillar array is shown in Fig. 3.8 for a PW and a CW state.

Figure 3.9 shows the wrapping energy as function of f_w . We find the envelopment transition W_2 , when the energy of the PW state is equal to the CW state at $f_w = 1$. The transition W_2 from a stable PW state to a stable CW state occurs at $w = w_2$, characterized by an energy barrier $\Delta E_{\text{barrier}}$. As w increases, the energy barrier between the PW state and the CW state vanishes, characterized by the spinodal S_{22} for adhesion strength w_{22} . For adhesion strengths $w \geq w_{22}$, the membrane spontaneously wraps the nanostructure completely.

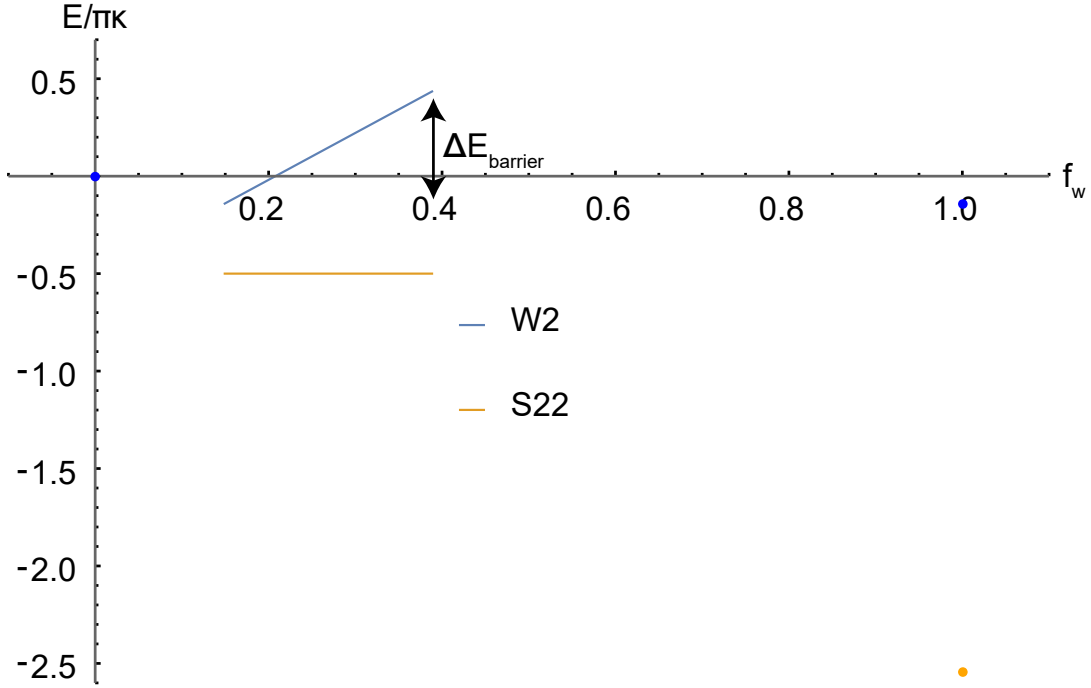


Figure 3.9: Wrapping energy E as a function of wrapping fraction f_w . The energy barrier $\Delta E_{\text{barrier}}$ is the difference between largest and smallest energies of the W_2 transition.

3.2.2 Wrapping diagrams for various σ and w

Wrapping diagrams can be used to characterize the effect of adhesion strength, membrane deformation, and line tension contributions on wrapping. We use line tension $\gamma = 1$ pN, calculated for lipid rafts on giant unilamellar vesicles [258, 259], and line tension $\gamma = 0$ as a reference system to calculate wrapping phase diagrams with transitions from PW to CW states for membrane tension σ and adhesion strength w for different surface structures (Fig. 3.10). The states for large membrane tensions are PW, and for small membrane tensions are CW for a given adhesion strength. Increasing the line tension shifts the transitions to larger membrane tensions, as line tension contributions add extra costs to the membrane free energy. For W_2 transition, the adhesion strength follows the relation

$$w_2 = \frac{\sigma + \frac{\kappa}{2r^2} + \frac{2\gamma}{h}}{1 + \frac{l^2}{2\pi r h} - \frac{r}{2h}}. \quad (3.6)$$

For fixed membrane tension σ , the nanostructures that require the lowest adhesion strengths w to get wrapped are the most favourable ones. We find that the

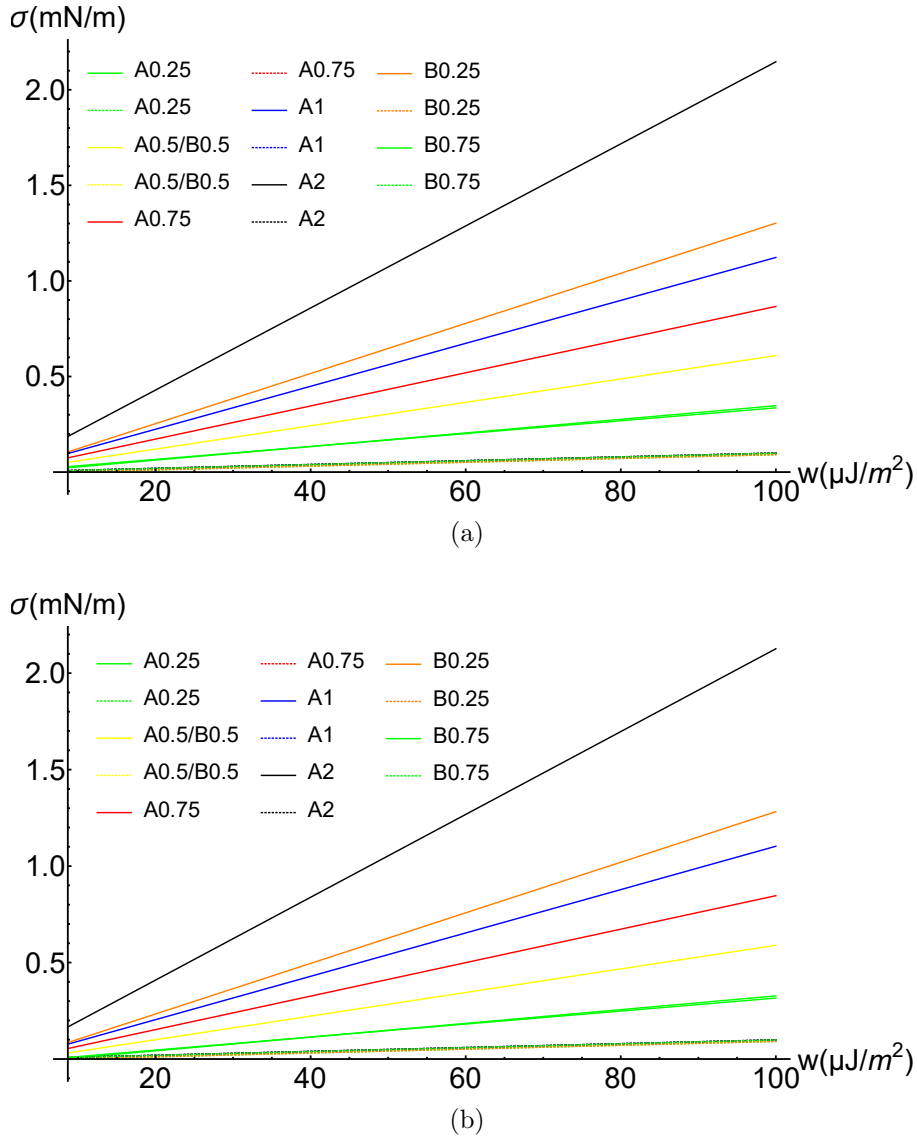


Figure 3.10: Wrapping transitions W_2 from partial- wrapped to complete- wrapped states for line tensions (a) $\gamma = 0$ and (b) $\gamma = 1$ pN, respectively, for different experimental geometries as discussed in Tab. 3.1. The bending rigidity $\kappa = 66 k_B T$, and height of the nanopillars $h = 100$ nm. The solid lines correspond to the W_2 transitions. The dotted lines represent S_{22} transitions.

nanostructure $A2$ is the easiest to wrap, followed by $B0.25$, $A1$, and so on. The geometries $A0.25$ and $B0.75$ are the least favourable geometries as these nanostructures require the largest adhesion strength w for the membrane to wrap them completely (Fig. 3.10).

Figure 3.11 shows the spinodals for the different W_2 transitions in Fig. 3.10.

3.2 Theoretical modelling of nanostructure wrapping

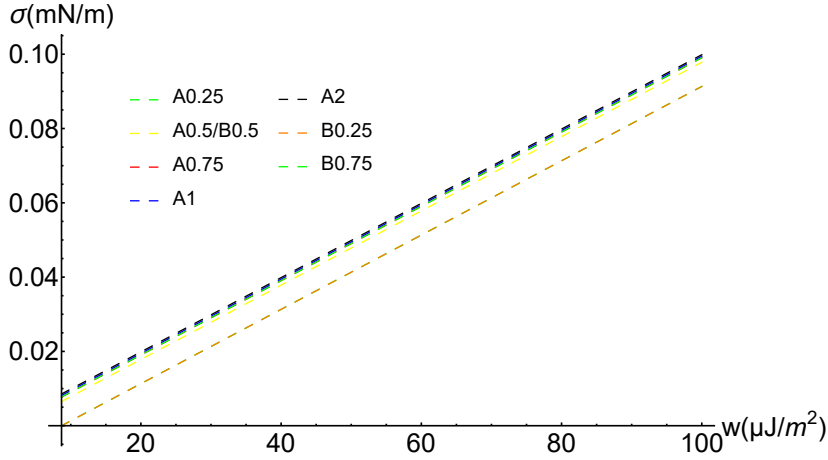


Figure 3.11: Spinodals corresponding to the W_2 transitions in Fig. 3.10 (a). Line tension $\gamma = 0$.

For larger nanopillar radii, the spinodals are shifted to smaller membrane tensions. This is due to the fact that the deformation-energy costs due to membrane bending are less for large nanopillar radii. For S_{22} , the adhesion strength follows the relation

$$w_{22} = \sigma + \frac{\kappa}{2r^2}. \quad (3.7)$$

Thus, the adhesion strengths for the spinodals of the nanostructures $A0.25$ and $B0.25$, $A0.5$ and $B0.5$, and $A0.75$ and $B0.75$ coincide.

For a value of the line tension $\gamma = 1$ pN, the line tension contributes only little to the wrapping transition W_2 . Spontaneous wrapping does not occur for any finite value of the line tension. We estimate different energy contributions for typical values of the parameters. For $\kappa = 66$ $k_B T$ [260], $\sigma = 0.12$ mN/m [261,262], $z = h = 100$ nm [248], $r = 250$ nm [248], $l = 1$ μm [248], $w = 7.3 \times 10^{-3}$ $k_B T/nm^2$ [249,263,264], and $\gamma = 0$, the deformation energy cost for wrapping is $\Delta E_d = 4,670$ $k_B T$, and for $\gamma = 1$ pN is $\Delta E_d = 5,434$ $k_B T$. Thus, the line tension contribution to ΔE_d is 764 $k_B T$, which is much smaller than the bending energy contribution and thus does not affect our results significantly. For the same values of the parameters, the adhesion energy gain is $\Delta E_{adh} = -8,447$ $k_B T$.

3.2.3 Wrapping diagrams for various r and w

We plot envelopment transitions for various nanopillar radii r and adhesion strengths w for different pitches l (Fig. 3.12). For all our calculations, we use membrane tension $\sigma = 0.03$ $k_B T/nm^2$ [261,262], and bending rigidity $\kappa = 66$ $k_B T$ [260]. For very small radii, the membrane bending contribution dominates

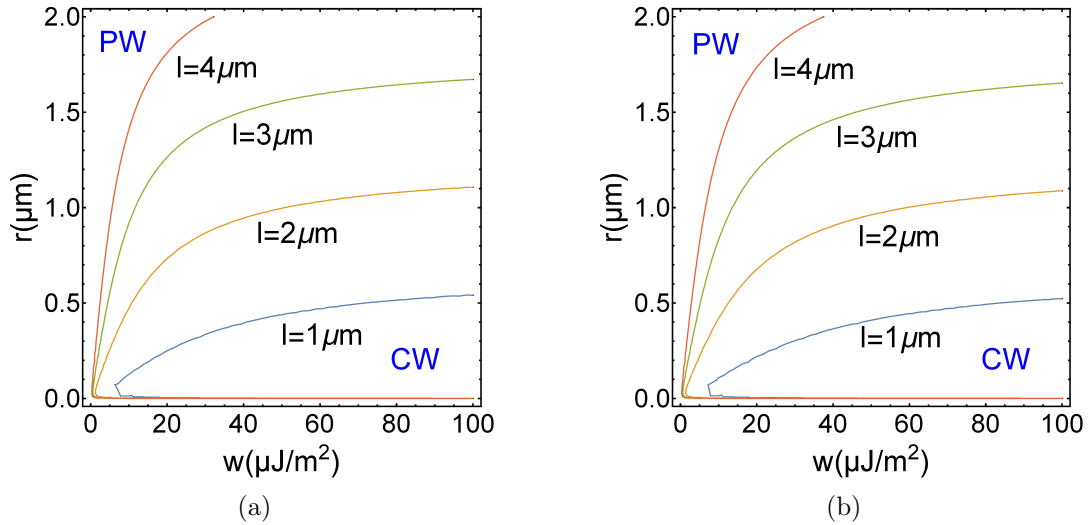


Figure 3.12: Wrapping transitions from PW to CW states for nanopillar radii r and adhesion strengths w for different pitches l , and for line tensions (a) $\gamma = 0$, and (b) $\gamma = 1$ pN, respectively. The membrane tension $\sigma = 0.12$ mN/m, bending rigidity $\kappa = 66$ $k_B T$, and height of the nanopillar $h = 100$ nm. Below each line is a complete-wrapped state and above is a partial-wrapped corresponding to that particular l .

for the cylindrical nanopillars, and it scales as $1/r$. Thus, we find that the transitions for various pitches $l = 1$ μm , $l = 2$ μm , $l = 3$ μm , and $l = 4$ μm coincide. For fixed pitch l , we predict CW states for small r and large w , and PW states for large r . For constant w , as we increase r , or for constant r , as we decrease w , we require larger pitches for the pillars to still get completely wrapped. Small r and large l are thus the most favourable geometries for complete wrapping. For $\gamma = 0$ and $\gamma = 1$ pN, we do not observe a significant difference in our results.

3.2.4 Wrapping phase diagrams for w , l , and r of the nanopillar

Figure 3.13 shows the adhesion strength w as function of pitch l and radius r of the nanopillar. Lines of fixed adhesion strength therefore are transitions in wrapping diagrams. The states for small r and large l are CW states, while the states for large r and small l are PW states. With increasing w , the W_2 transitions shift to larger r and smaller l values.

For $\gamma = 0$, and for $w = 10$ $\mu\text{J}/\text{m}^2 = 2.4 \times 10^{-3}$ $k_B T/\text{nm}^2$, only $B0.25$ is complete-wrapped, while all the other geometries are partial-wrapped. For $w = 30$ $\mu\text{J}/\text{m}^2 = 7.3 \times 10^{-3}$ $k_B T/\text{nm}^2$, as reported in Ref. [263], we predict complete wrapping for $B0.25$, $A0.5/B0.5$, and $A0.75$, and partial wrapping for the other geometries, as seen in the experiments. For $w = 100$ $\mu\text{J}/\text{m}^2 = 24.3 \times 10^{-3}$ $k_B T/\text{nm}^2$,

3.2 Theoretical modelling of nanostructure wrapping

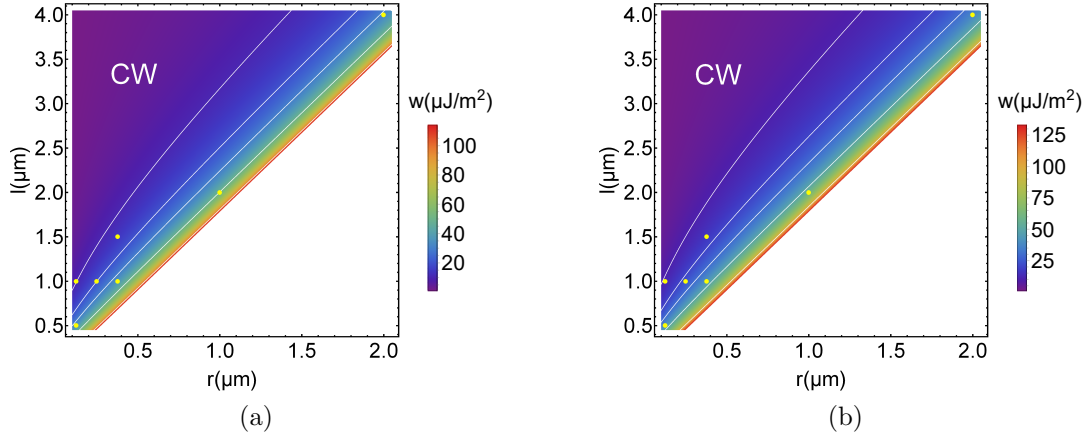


Figure 3.13: Adhesion strength w for different pitches l , and radii r of the nanopillar, for line tensions (a) $\gamma = 0$, and (b) $\gamma = 1$ pN, respectively. The membrane tension $\sigma = 0.12$ mN/m, bending rigidity $\kappa = 66$ $k_B T$, and height of the nanopillars $h = 100$ nm. The white lines represent equal energy contours for different w values, viz., $w = 10, 20, 30, 50, 100 \mu\text{J}/\text{m}^2$, from left to right respectively, indicating the partial-wrapped and the complete-wrapped states in the wrapping diagram. The marked yellow points are the combinations of l and r values used in the experiments. The minimum distance between two nanopillars is $2r$, making the area for $l < 2r$ inaccessible, indicated by the white region in the plot.

the adhesion energy is large enough that the membrane completely wraps the nanopillar for all geometries used in the experiments. For line tension $\gamma = 1$ pN, we observe a shift in the wrapping states. Some envelopment transitions observed for $\gamma = 0$, characterised by the intersection of the equal energy contours for different w values with the geometries used in the experiments, shift to partial-wrapped states for $\gamma = 1$ pN. For example, for $\gamma = 1$ pN, for $w = 10 \mu\text{J}/\text{m}^2$ all the geometries used in the experiments are partially wrapped. The shifts in the wrapping transitions occur due to the fact that for $\gamma = 1$ pN, the membrane requires a larger adhesion strength to wrap the nanopillar completely compared to $\gamma = 0$. In the experiments, complete wrapping is only observed for *B0.25*, *A0.5/B0.5*, and *A0.75*. Comparing our analytical predictions with the experimental observations, we conclude that the adhesion strength w for the neuron is $30 \mu\text{J}/\text{m}^2$, Fig. 3.13, in agreement with Ref. [263].

3.2.5 Nanopillar-adhered area relative to the flat surface area

Although Fig. 3.13 provides us an insight into optimal nanopillar geometries to obtain complete wrapping for known values of w , σ , and γ , but it is incomplete on its own, as it does not take into account the relative nanopillar-adhered area

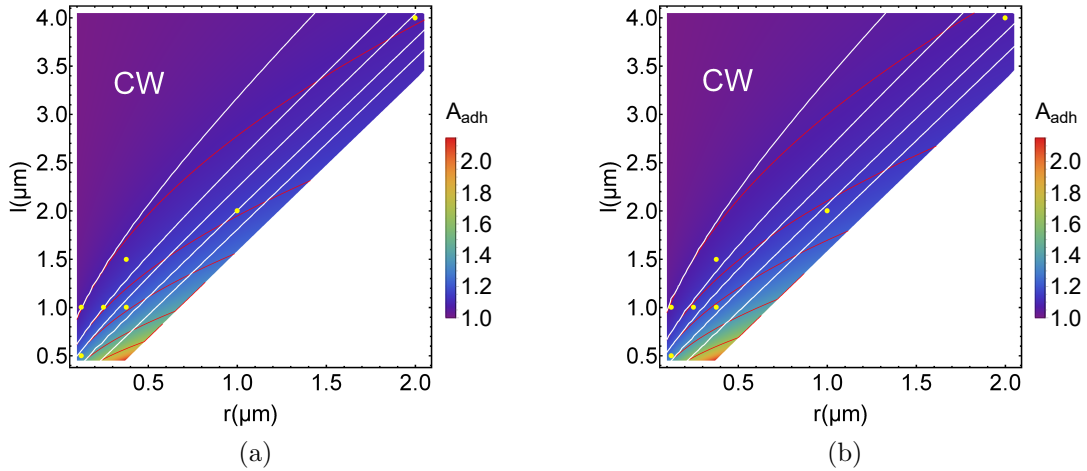


Figure 3.14: Nanopillar adhered area relative to the flat surface area A_{adh} , for different pitches l , and r , for line tensions (a) $\gamma = 0$, and (b) $\gamma = 1$ pN, respectively. The membrane tension $\sigma = 0.12$ mN/m, bending rigidity $\kappa = 66$ k_BT, and height of the nanopillars $h = 100$ nm. The white lines represent equal energy contours for different w values, viz., $w = 10, 20, 30, 50,$ and 100 $\mu\text{J}/\text{m}^2$, from left to right respectively, similar to Fig. 3.13. The marked yellow points are the combinations of l and r values used in the experiments. For white regions in the plots, large nanopillar radius r and small pitch l are inaccessible. The red lines correspond to maximal A_{adh} contours for each of the w values, respectively.

gained upon complete wrapping. For example, for $w = 30$ $\mu\text{J}/\text{m}^2$, we obtain three geometries $B0.25$, $A0.5/B0.5$, and $A0.75$, with complete-wrapped states, but we cannot predict the structure with the largest adhered area for complete wrapping. Including relative nanopillar adhered area provides us a complete picture of the wrapping process, and in turn lets us predict the best geometries for a neuron with a particular w , σ , and γ .

We plot A_{adh} as function of r and l , for constant nanopillar height $h = 100$ nm (Fig. 3.14). The interactions for the contour lines for the envelopment transitions for fixed adhesion strength and for the maximal relative adhered area represent ideal surface structures. On one hand, the relative adhered area increases with increasing radius, and decreases with increasing pitch of the nanostructure array. On the other hand, CW states are found for small radii and large pitches. For increasing r and l , we approach the flat surface regime.

Comparison with the experimental data shows that for $\gamma = 0$ and $w = 30$ $\mu\text{J}/\text{m}^2$, $B0.25$, $A0.5/B0.5$, and $A0.75$ arrays are completely wrapped; $A0.5/B0.5$ has the maximum A_{adh} , followed by $B0.25$ and $A0.75$. For the partial-wrapped states, $A0.25$ array has the maximum A_{adh} .

3.3 Conclusions and Outlook

We systematically investigated wrapping of nanopillar arrays by membranes. We use SEM and FIB-SEM to characterize the membrane into rest membrane, bending membrane, top contact membrane, and bottom contact membrane, for different nanopillar geometries. The four energy contributions to continuum-model calculations for the wrapping are bending energy, adhesion energy, membrane tension, and line tension. For given bending rigidity, adhesion strength, and membrane and line tension, small nanopillar radii and large pitches for the arrays favour complete wrapping of the nanopillars. Increasing line tension hinders wrapping, as it opposes the membrane to bend along the corners of the nanopillars. However, for a small finite line tension, the line tension contribution does not affect the results significantly. The wrapping spinodals are independent of the pitch. Large nanopillar radii reduce the energy barrier between partial-wrapped and complete-wrapped states, and thus facilitate complete wrapping of the nanostructures. The relative nanopillar-adhered area increases with increasing radius and height of the nanopillar, and decreases with increasing pitch of the arrays, keeping other parameters fixed.

The intersections of equal energy and maximal relative adhered-area contours for different adhesion strengths and comparison with the nanostructure geometries used in the experiments provides us the optimal geometries for the nanostructures. We obtain three combinations of radii and pitches of the nanostructures ($r = 0.125 \mu\text{m}$, $l = 1 \mu\text{m}$), ($r = 0.25 \mu\text{m}$, $l = 1 \mu\text{m}$), and ($r = 0.375 \mu\text{m}$, $l = 1.5 \mu\text{m}$) for which the membrane wraps the nanopillars completely. Amongst them, the nanostructure geometry with $r = 0.25 \mu\text{m}$, and $l = 1 \mu\text{m}$ has the maximum relative adhered area. In case of the neuronal cells used in the experiments, by comparing experimental results and theoretical calculations, our theoretical model predicts an adhesion strength of $w = 30 \mu\text{J}/\text{m}^2$ for the cell membrane, which is in agreement with literature. If one were to construct different geometries for MEAs, our model thus provides an informed estimate for optimal geometries to maximize the cell-electrode contact.

Chapter 4

Effect of red blood cell cytoskeleton on particle uptake

Be the change you wish to see in the world.

– M. K. Gandhi

In chapter 2, we focused on nanoparticle (NP) wrapping by a red blood cell (RBC) membrane, where we studied NPs of different sizes. We considered receptor-mediated adhesion of NPs to cells and found wrapping transitions from non-wrapped (NW) to partial-wrapped (PW) and complete-wrapped (CW) states. In this chapter, we consider a different aspect, the effect of RBC spectrin network on particle wrapping.

Both wrapping of a particle by the RBC membrane without cytoskeletal contributions, and modelling of a RBC with cytoskeleton and quantification of its elastic properties without a particle have been studied comprehensively [163, 165, 172, 265, 266]. The focus of most of the above studies concerning modelling of RBCs has been continuum and coarse-grained simulations of entire RBCs, and quantification of their elastic properties. We go a step further, include a spectrin network along with the RBC membrane, and revisit the particle-wrapping problem.

4.1 The RBC spectrin network as a network of entropic springs

We model the RBC spectrin network by a network of entropic springs, with and without an ankyrin complex in the middle of each spectrin filament (Fig. 4.1) [172, 267]. The ankyrin attaches the spectrin network to the lipid bilayer membrane. Each node represents an actin junction complex, and each entropic spring represents a spectrin filament. Each spectrin filament consists of n spherical spectrin beads connected by $n - 1$ unbreakable springs. Each node is connected to six

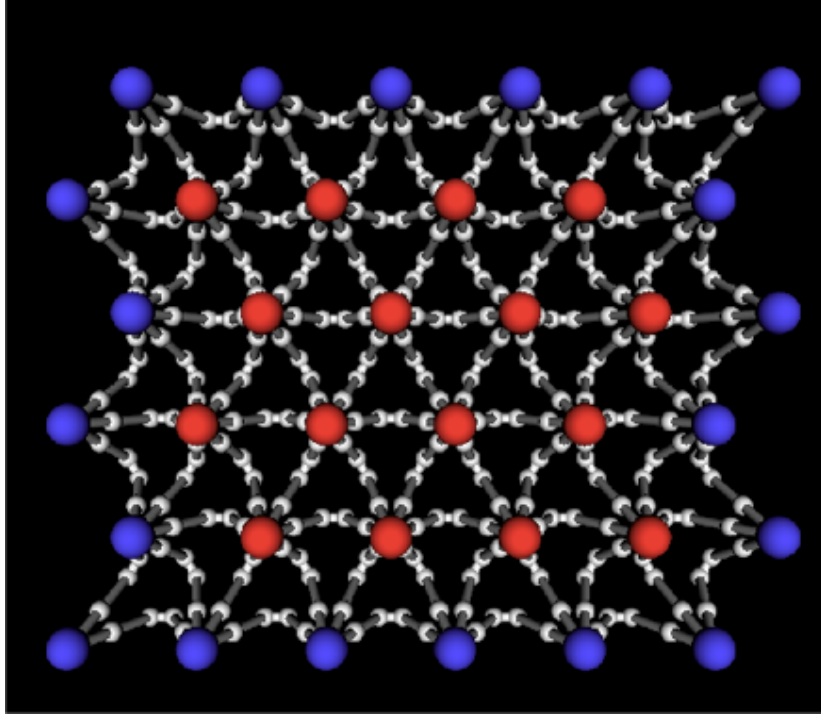


Figure 4.1: Top view of the spectrin network showing $z = 0$ membrane plane. The axis pointing in the plane is the $-z$ direction. The red balls are the actin nodes representing Band-3 complexes attached to the membrane, which diffuse in 2D, white beads are the spectrin beads, which diffuse in 3D, and the blue balls are the edge points held fixed. If ankyrin complexes are present, they are in the middle of the spectrin polymer attached to the membrane.

other nodes, resulting in a hexagonal arrangement of the network. We simulate a rectangular spectrin network with dimensions of 12×12 squared simulation units (su), where $1 \text{ su} = 80 \text{ nm}$, spectrin bond length $l_{\text{actin}} = 80 \text{ nm}$ [268, 269], and spectrin contour length $l_c = 200 \text{ nm}$ [174]. The nodes at the edges of the spectrin network are fixed. The force exerted by each spring between two spectrin beads F_{sp} is given by Hooke's law,

$$F_{\text{sp}} = -k_{\text{sp}}(l - l_{\text{eq}}), \quad (4.1)$$

where l is the length of the spring and l_{eq} the equilibrium length. The spring constant k_{sp} of each individual spring is chosen such that the contour length $l_c = 2.5 l_{\text{actin}} = 200 \text{ nm}$ remains constant throughout the simulation. The particle is modelled by a sphere with radius R , and the nodes of the spring network are modelled by point particles that are subject to frictions $\zeta_p = k_B T / D_p$ and $\zeta_{\text{sp}} = k_B T / D_{\text{sp}}$, respectively.

We first benchmark our system by calculating the effective spring constant of

4.1 The RBC spectrin network as a network of entropic springs

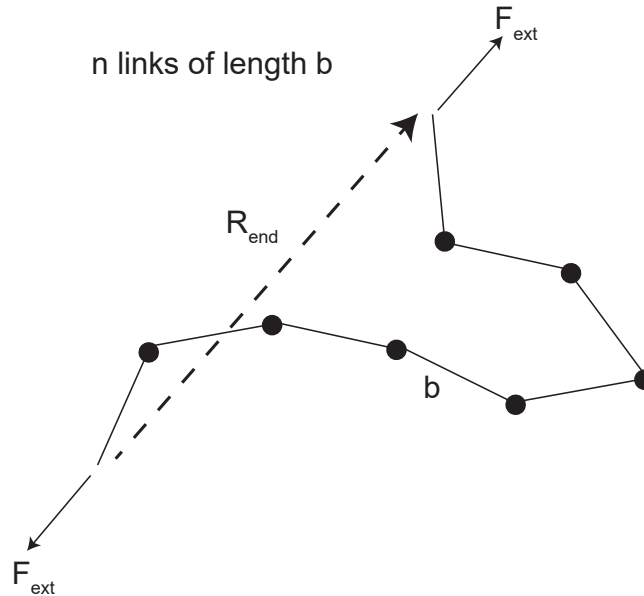


Figure 4.2: Schematic of an entropic spring. Freely jointed chain model of a polymer with n links of length b , and end-to-end distance R_{end} . An external force F_{ext} stretches the chain.

a single entropic spring and comparing it with theory.

4.1.1 Spring constant of an entropic spring

The freely jointed chain (FJC) model

We model the entropic spring as a polymer using the freely-jointed chain (FJC) model (Fig. 4.2) [270]. In an entropic spring, there are fewer ways to arrange the chain the more it is extended, leading to a decrease in entropy and thus an increase in free energy. In other words, the restoring force increases as the length increases. In this model, the chain is allowed to cross itself, and the direction of each link is random and independent of all the others, including its neighbours. The freely jointed chain can be modelled as a random walk with n links, each of equilibrium length b . The end-to-end distance for such a chain is $R = b\sqrt{n}$, and the contour length $l_c = nb$.

Applying a force F_{ext} to the ends of the chain, and measuring its end-to-end distance R_{end} in the direction of the applied force, one can write the relation between F_{ext} and R_{end} [270],

$$F_{\text{ext}} = \frac{3k_{\text{B}}T}{nb^2}R_{\text{end}} + O(R_{\text{end}}^3). \quad (4.2)$$

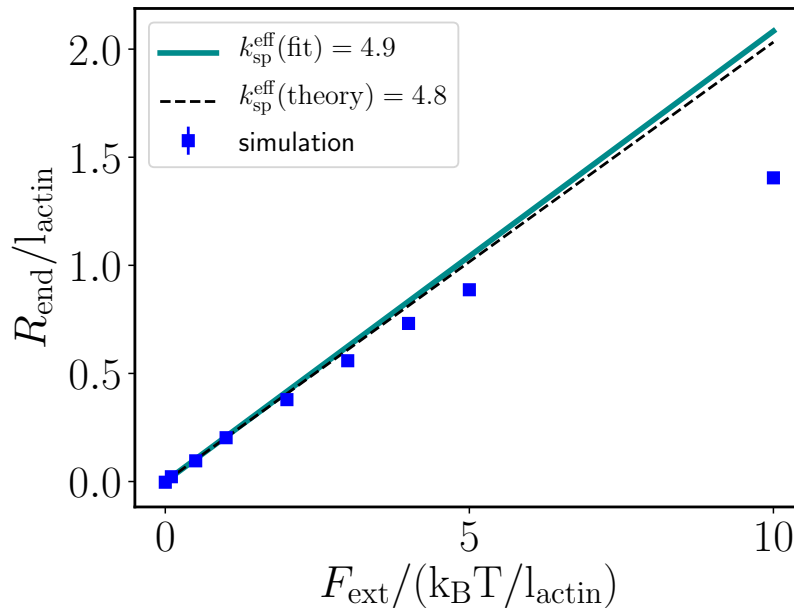


Figure 4.3: End-to-end distance R_{end} as function of external force F_{ext} applied along the ends of the chain. The blue squares depict simulation points. Inverse of the slopes of the fit (dark cyan) and theory (dashed black) lines determines the effective spring constant $k_{\text{sp}}^{\text{eff}}$ (Eq. 4.3).

Equation 4.2 holds only for the small-force regime. Ignoring terms of the order $O(R_{\text{end}}^3)$, we can extract an effective spring constant

$$k_{\text{sp}}^{\text{eff}} = \frac{3k_B T}{nb^2}. \quad (4.3)$$

For $n = 10$, $b = l_c/n$, and $k_B T = 1$, $k_{\text{sp}}^{\text{eff}} = 4.8 k_B T / l_{\text{actin}}^2$. Figure 4.3 shows the end-to-end distance R_{end} as function of the external force F_{ext} that is applied to the ends of the chain. For small F_{ext} , the simulations agree with the theory. We fit a straight line to the simulation for small F_{ext} and extract $k_{\text{sp}}^{\text{eff}} = 4.9 k_B T / l_{\text{actin}}^2$, which is almost equal to the theoretical spring constant for a polymer with 10 monomers and contour length $l_c = 2.5 l_{\text{actin}}$, $k_{\text{sp}}^{\text{eff}} = 4.8 k_B T / l_{\text{actin}}^2$. Figure 4.4 shows $k_{\text{sp}}^{\text{eff}}$ for various numbers of bonds, n . As n increases, for given contour length the persistence length of the polymer decreases, leading to an increased stiffness of the entropic spring. For various values of n , the simulations for single springs agree very well with the theory, see Figs. 4.3 and 4.4.

4.1.2 The model

The particle is modelled by a sphere with radius R , and the spectrin beads by spheres with radii $R_{\text{sp}} = 2.5 \text{ nm}$ [174]. They experience frictions ζ_p and

4.1 The RBC spectrin network as a network of entropic springs

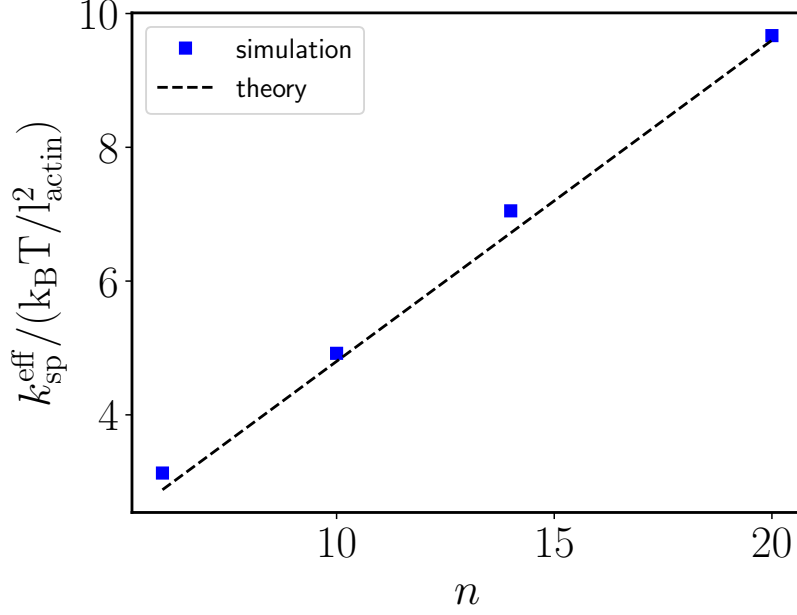


Figure 4.4: Effective spring constant k_{sp}^{eff} for different number n of spectrin beads. The blue squares depict simulation points, and the dashed black line is the theoretical estimate based on Eq. 4.3.

ζ_{sp} , respectively. The repulsive interaction force between the particle and each spectrin bead is the modified truncated Lennard-Jones potential,

$$F_{lj} = \begin{cases} \frac{12\epsilon}{r-(R-R_{sp})} \left[\left(\frac{r_{min}}{r-(R-R_{sp})} \right)^{12} - \left(\frac{r_{min}}{r-(R-R_{sp})} \right)^6 \right], & r \leq r_{min} \\ 0, & r > r_{min} \end{cases} \quad (4.4)$$

with interparticle distance r , distance $r_{min} = 2^{7/6}R_{sp}$ at which the potential reaches its minimum, and Lennard-Jones force strength ϵ . We use $\epsilon = 1 \text{ k}_B\text{T}$. In addition, the spectrin beads experience a repulsive Lennard-Jones force from the membrane

$$F_{ljsp} = \begin{cases} \frac{12\epsilon}{z-z_0} \left[\left(\frac{r_{min}}{z-z_0} \right)^{12} - \left(\frac{r_{min}}{z-z_0} \right)^6 \right], & z \leq r_{min} \\ 0, & z > r_{min} \end{cases} \quad (4.5)$$

with $z_0 = 0.0641714 \text{ l}_{actin}$, which confines them to the region $z < 0$.

The adhesion force between the particle and the membrane is modelled as constant force

$$F_{ad} = 2\pi R w_{eff} \quad (4.6)$$

acting on the particle in $-z$ direction, with the effective particle-membrane adhesion strength $w_{eff} = w - \kappa/A$, where κ is the bending rigidity of the membrane, w

is adhesion strength between the particle and the membrane, and A is the surface area of the particle.

The dynamics of the particle and the spectrin beads is calculated using Brownian dynamics,

$$\begin{aligned}\zeta_p \partial_t r_p &= -F_{\text{ad}} + F_{\text{lj}} + \sqrt{2\zeta_p kT} \eta_p(t), \\ \zeta_{\text{sp}} \partial_t r_{\text{sp}} &= F_{\text{sp}} - F_{\text{lj}} - F_{\text{ljsp}} + \sqrt{2\zeta_{\text{sp}} kT} \eta_{\text{sp}}(t)\end{aligned}\tag{4.7}$$

with the friction coefficients ζ_p and ζ_{sp} for the particle in solution and for the spectrin beads, respectively. The Gaussian white noises $\eta_p(t)$ and $\eta_{\text{sp}}(t)$ have zero mean $\langle \eta(t) \rangle = 0$, and $\langle \eta(t) \eta(t') \rangle = 2B\delta(t - t')$, where B is the strength of the random noise. Following the Fluctuation-dissipation theorem, $B = \zeta k_B T$. Using Stokes friction for spherical particles, $D = kT/\zeta$, we can express the above equations in terms of the diffusion coefficients for particle and spectrin beads. The lengths in simulation and water are connected via the particle diameters, d_p and d_{sim} . The time scales in simulations and experiments are connected using $t_p = (D_{\text{sim}} d_p^2) / (D_p d_{\text{sim}}^2) t_{\text{sim}}$, for typical values for the particle diffusion coefficients, D_p calculated using the Stokes friction for a spherical particle in water, and D_{sim} for the particle in simulation units. The equations of motion for NPs and receptors are integrated using Euler algorithm and the time step corresponds to $\Delta t = 6.4$ ns for particles with $R = 40$ nm [206]. Experimentally measured diffusion coefficients for proteins and lipids in RBC membranes and in model lipid bilayers are in the range of $0.25 \mu\text{m}^2/\text{s} \leq D_{\text{sp}} \leq 13.2 \mu\text{m}^2/\text{s}$, see Section 2.3 in Chapter 2. We assume $D_p/D_{\text{sp}} = 1$, and $\zeta_p/\zeta_{\text{sp}} = 1$.

4.2 Free energy of a particle crossing the spectrin network

We calculate the quasistatic energy contribution E_{sp} of the spectrin cytoskeleton for various positions of the particle; $E_{\text{sp}} = 0$ if the particle does not interact with the spectrin. The particle is pushed through the network with a length increment $dz = 0.013 l_{\text{actin}}$ at each time step. Figure 4.5 shows simulation snapshots for an unperturbed spectrin network and for the spectrin network deformed around a particle. The particle pushes the spectrin beads away in order to make way for itself to pass through the network. Figure 4.6 shows E_{sp} as function of wrapping fraction f_w for different radii R of the particle, different numbers n of spectrin beads in the filament, and with and without ankyrin. The spectrin energy difference E_{sp} relative to the non-wrapped state increases with particle radius R . In the absence of ankyrin, larger n hinders the particle more as there are more spectrin beads that interact with the particle (Fig. 4.6 (a), (c)). The presence of ankyrin adds a geometric constraint on the possible spectrin filament

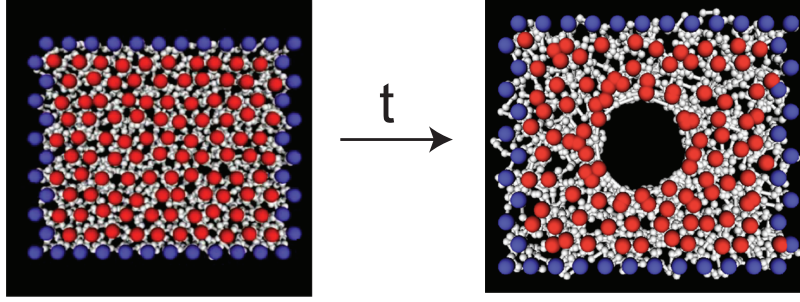


Figure 4.5: Snapshots of a particle crossing a spectrin network. The red beads depict the actin junction complexes, and white beads depict the spectrin beads of the spectrin filament. The blue beads are held fixed throughout the simulation. The particle is depicted by a hole and the spectrin network is pushed away to make way for the particle.

configurations, thus reducing the entropy of the filament. This effectively makes the filament softer [271] and therefore reduces its interaction with the particle. Hence, larger n hinders the particle less (Fig. 4.6 (b), (d)). Figure 4.7 explains this argument pictorially. In the absence of ankyrin, the filament is like a 3D chain and can have any conformation in the half space bounded by the membrane, whereas the ankyrin attachment restricts the filament conformations, and reduces the entropy of the filament. This in turn results in a softer effective spring constant in 2D compared to 3D: $k_{\text{sp},2\text{D}} = (2/3)k_{\text{sp},3\text{D}}$ [271].

For $n = 6$, $R = 0.25 l_{\text{actin}}$, and with ankyrin, E_{sp} is smaller than for $n = 10$ and $n = 14$. The radius of the particle is smaller than the inradius ($R_{\text{in}} = \sqrt{3}/6 l_{\text{actin}} \approx 0.29 l_{\text{actin}}$) of the spectrin filament triangle as well as smaller than the bond length $b = 0.417 l_{\text{actin}}$ for $n = 6$; therefore in some instances the particle does not ‘see’ the spectrin beads, which results in smaller values of E_{sp} .

4.2.1 Wrapping-energy calculations

The total energy of a wrapped particle is $E = E_{\text{sp}} + E_{\text{d}} + E_{\text{ad}}$, where E_{d} is the membrane deformation energy of the lipid bilayer, and E_{ad} is the adhesion energy. Using the Helfrich Hamiltonian introduced in Chap. 1, we can write E_{d}

$$\frac{E_{\text{d}}}{\pi\kappa} = 8f_{\text{w}}. \quad (4.8)$$

We use $\kappa = 50 \text{ k}_B\text{T}$ for a RBC [163, 265, 272, 273]. The adhesion energy is

$$\frac{E_{\text{ad}}}{\pi\kappa} = -2\tilde{w}f_{\text{w}}, \quad (4.9)$$

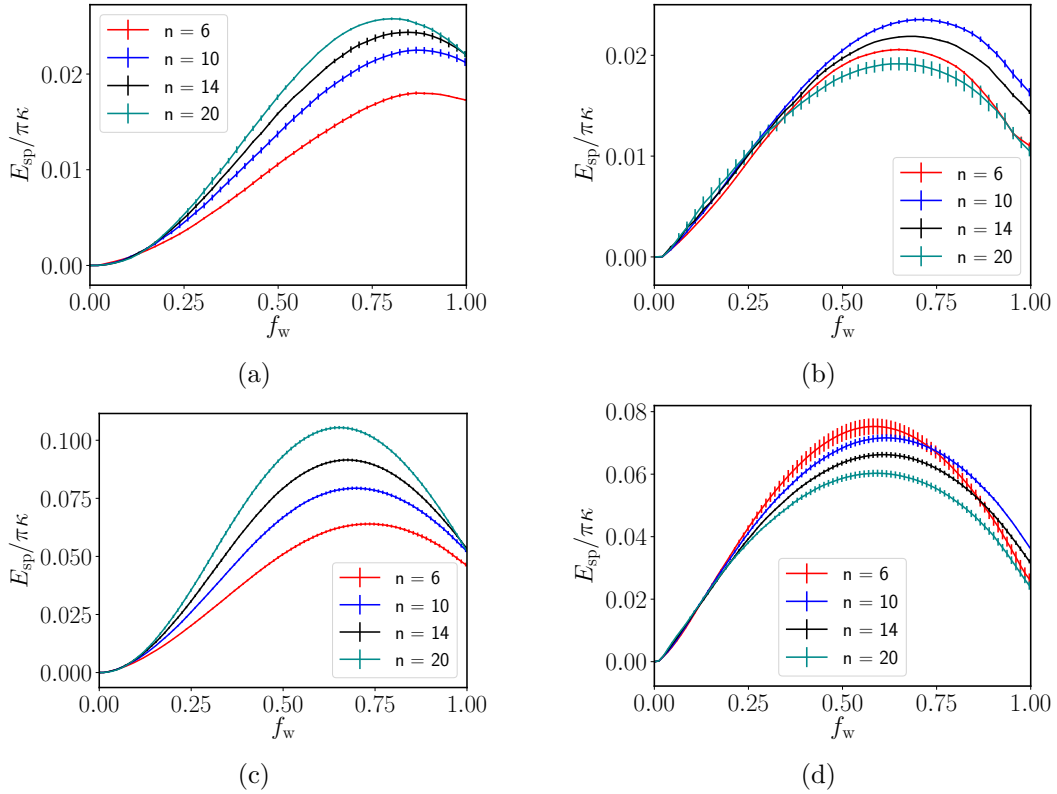


Figure 4.6: Energy contribution E_{sp} at equilibrium due to the spectrin network as function of wrapping fraction f_w for different number n of spectrin beads in the filament, and for (a) $R = 0.25 l_{\text{actin}}$ without ankyrin, (b) $R = 0.25 l_{\text{actin}}$ with ankyrin, (c) $R = 0.5 l_{\text{actin}}$ without ankyrin, and (d) $R = 0.5 l_{\text{actin}}$ with ankyrin.

where $\tilde{w} = 2R^2w/\kappa$ is the reduced adhesion strength [85]. The total energy E is

$$\frac{E}{\pi\kappa} = \frac{E_{\text{sp}}}{\pi\kappa} + (8 - 2\tilde{w})f_w. \quad (4.10)$$

For the calculations of the wrapping transitions, the numerical data for the spectrin energy in Fig. 4.6 are fit by a 17th order polynomial function

$$g(f_w) = \sum_{q=0}^{17} a_q f_w^q. \quad (4.11)$$

Figure 4.8 shows the total energy E as function of wrapping fraction f_w for $n = 10$, and $R = 0.5 l_{\text{actin}}$ without ankyrin. For all adhesion strengths $\tilde{w} < 4$, we predict no wrapping; the stable state for the particle is the non-wrapped (NW) state. The onset of wrapping occurs for $\tilde{w}_1 = 4$ at the binding transition W_1 for that the bending and the spectrin energy costs equal the adhesion-energy gain at the contact point. This binding transition is determined by the mean curvature of the

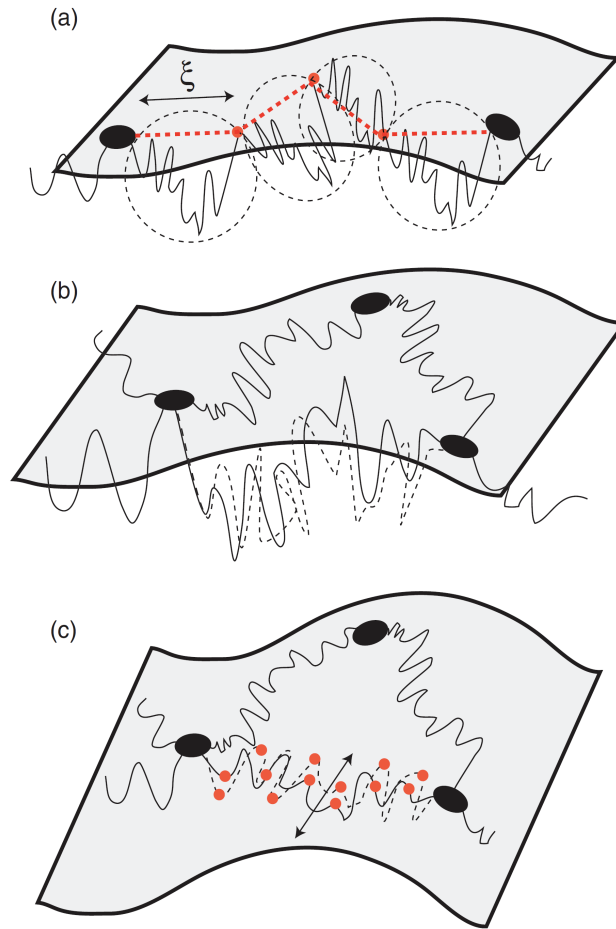


Figure 4.7: Schematic picture of the spectrin filament in the RBC network. (a) A filament attached to a fluid bilayer has 3D blobs (black dashed circles) along a 2D chain (red dashed line). (b) when there are no band-3/ankyrin attachments the filament can have any conformation in 3D, indicated by the dashed line. (c) In the limit of many mobile band-3/ankyrin attachments (red circles), the filament can only have 2D conformations inside the plane of the membrane (arrow and dashed line). Reproduced from Ref. [271]

membrane at the contact point and is independent of surface tension [10,85]. For a membrane with cortical cytoskeleton, the particle does not experience significant pressure at the point of contact with the membrane, and thus W_1 occurs at the same adhesion strength as for a lipid bilayer membrane that is not supported by a cytoskeleton. Increasing the adhesion strength further, we find the envelopment transition W_2 from the partial-wrapped (PW) to the complete-wrapped (CW) state at adhesion strength w_2 . For adhesion strengths $w_1 < w < w_2$, we find a global minimum of the wrapping energy for small wrapping fractions $0 < f_w < 1$.

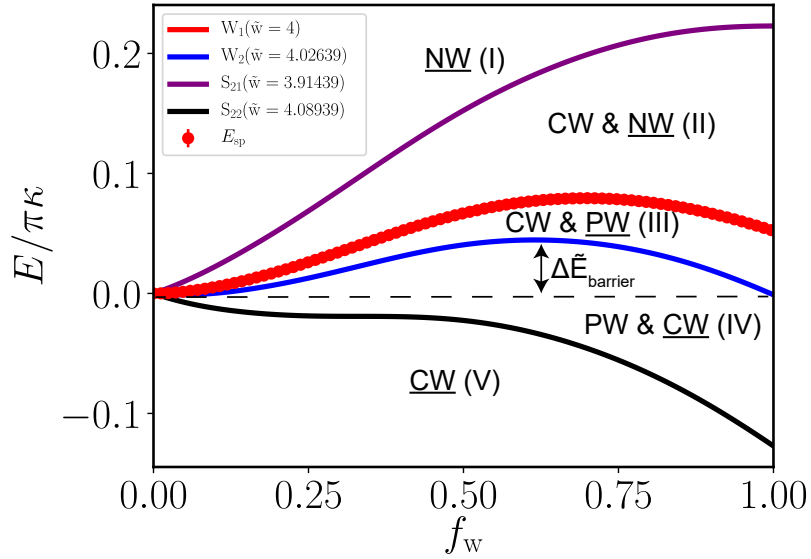


Figure 4.8: Energies $E/\pi\kappa$ for wrapping a spherical particle as function of the wrapping fraction f_w for $R = 0.5 l_{\text{actin}}$, $n = 10$ without ankyrin. The figure shows the wrapping profiles for four adhesion strengths: the numerically calculated data and the binding transition W_1 between the NW and the PW state ($\tilde{w} = 4$), the envelopment transition W_2 between the PW and the CW state ($\tilde{w} = 4.02639$), and the spinodals S_{21} and S_{22} that are associated with W_2 (for $\tilde{w} = 3.91439$ and $\tilde{w} = 4.08939$, respectively). We see five regimes in the plot with stable and metastable non-wrapped (NW), partial-wrapped (PW), and complete-wrapped (CW) states. The stable states are underlined. The energy barrier $\Delta\tilde{E}_{\text{barrier}}$ between the metastable PW state and the stable CW state is marked.

For adhesion strengths $w > w_2$, we find a stable CW state.

The binding transition between the NW to a PW state is continuous, while the envelopment transition between the PW and CW state is discontinuous with an energy barrier, $\Delta\tilde{E}_{\text{barrier}}$. For $w_1 < w < w_2$, in addition to the stable PW state at small wrapping fraction, a metastable CW state is found; similarly at higher adhesion strengths, in addition to the stable CW state a metastable PW state is found. The energy barrier between the metastable PW state and the stable CW state vanishes at an adhesion strength larger than w_2 , indicated by the wrapping spinodal S_{22} associated with W_2 . Starting from a CW state and continuously decreasing the adhesion strength, we observe a spontaneous transition between the CW state and the NW state below a threshold value w_1 , indicated by the unwrapping spinodal for W_2 , S_{21} . The energy barrier between the PW and the CW state, $\Delta\tilde{E}_{\text{barrier}}$, is indicated in Fig. 4.8.

4.2 Free energy of a particle crossing the spectrin network

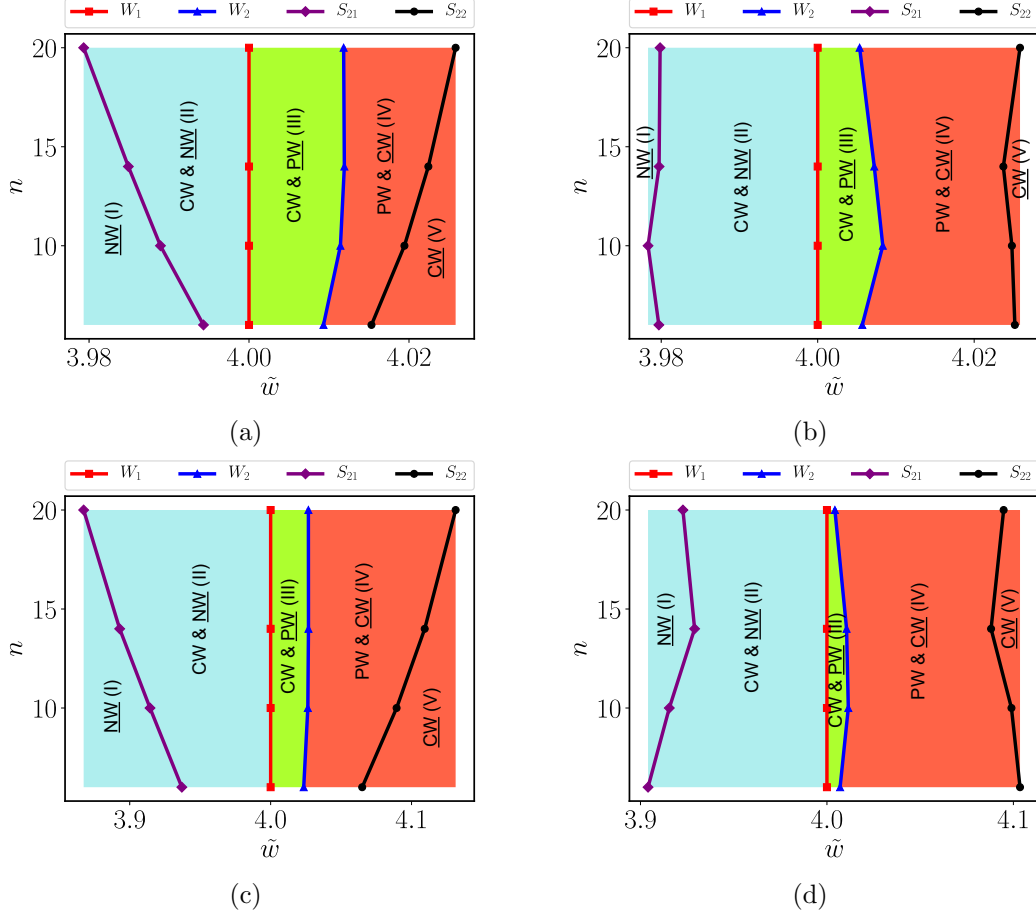


Figure 4.9: Wrapping states for the particle with reduced adhesion strengths \tilde{w} and for different numbers n of spectrin beads in a spectrin bond for (a) $R = 0.25 l_{\text{actin}}$ without ankyrin, (b) $R = 0.25 l_{\text{actin}}$ with ankyrin, (c) $R = 0.5 l_{\text{actin}}$ without ankyrin, and (d) $R = 0.5 l_{\text{actin}}$ with ankyrin. Non-wrapped (NW, turquoise), partial-wrapped (PW, yellow), and complete-wrapped (CW, crimson) states are found, stable and metastable states are indicated, and stable states are underlined.

4.2.2 Wrapping diagrams

Wrapping diagrams for various numbers n of spectrin beads and reduced adhesion strengths \tilde{w} are shown in Fig. 4.9. We identify five regimes with different combinations of stable and unstable NW, PW, and CW states. For small adhesion strengths, a stable NW state (NW(I)) is found. In addition to the stable NW state, we find a metastable CW state between the spinodal S_{21} for the spontaneous transition between the CW and the NW state, and the binding transition W_1 (CW & NW(II)). The binding transition W_1 occurs at $\tilde{w} = 4$ and is independent of n , and of the presence of ankyrin. Beyond W_1 , a stable PW state

Effect of red blood cell cytoskeleton on particle uptake

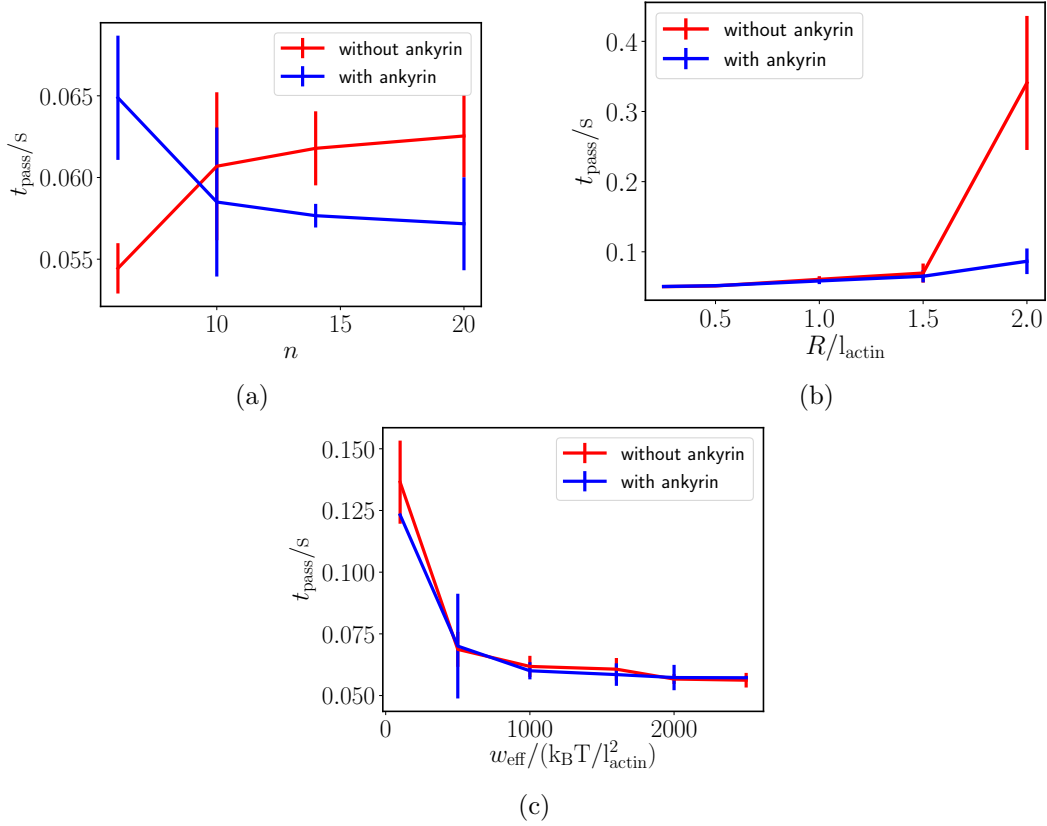


Figure 4.10: First-passage times t_{pass} for (a) different numbers n of spectrin beads with and without ankyrin, (b) different radii R of the particle with and without ankyrin, and different effective adhesion strengths (w_{eff}) with and without ankyrin. We use $R = l_{\text{actin}}$, $w_{\text{eff}} = 1600 \text{ k}_B T / l_{\text{actin}}^2$ in (a), $n = 10$, $w_{\text{eff}} = 1600 \text{ k}_B T / l_{\text{actin}}^2$ in (b), and $R = l_{\text{actin}}$, and $n = 10$ in (c).

coexists with the metastable CW state (CW & PW(III)). For adhesion strengths beyond those for the envelopment transition W_2 , we find a stable CW state and a metastable PW state (PW & CW(IV)). Finally, beyond the the spinodal S_{22} , the energy barrier between the CW and the PW state vanishes, and we find a stable CW state (CW(V)).

Increasing R increases the adhesion strengths required for a particle to cross the spectrin network. The presence of ankyrin enlarges the metastable PW areas for both radii ($R = 0.25 l_{\text{actin}}$ and $R = 0.5 l_{\text{actin}}$) compared to without ankyrin, as the presence of ankyrin helps in particle wrapping.

4.3 Particle dynamics and first-passage times

We investigate the dynamics of the particle crossing the spectrin network. A particle diffusing under a constant adhesion force F_{adh} interacts with the spectrin network. We calculate the particle first-passage time t_{pass} as the time required for the particle to transit from a NW to a CW state. We benchmark our system where we calculate t_{pass} using theory and compare it with our simulations, see Appendix A.

Figure 4.10 shows the particle first-passage times for different numbers of spectrin beads in the filament, radii of the particle, and effective adhesion strengths. In the absence of ankyrin, t_{pass} increases with n as more spectrin beads provide more resistance to the particle to cross the spectrin network. With ankyrin present, the entropy of the filament is reduced, which leads to less filament conformations and hence shorter t_{pass} for larger n (Fig. 4.10 (a)). We use $R = l_{\text{actin}} = 80$ nm, and $w_{\text{eff}} = 1600 \text{ k}_B\text{T}/l_{\text{actin}}^2 = 0.25 \text{ k}_B\text{T}/\text{nm}^2$ [145].

The first-passage time increases with radius of the particle because of the stronger interaction of larger particles with the spectrin network, thus requiring more time to pass through the network. The time without ankyrin is equal to or less than with ankyrin (Fig. 4.10 (b)). We use $n = 10$, which corresponds to a spectrin persistence length of 20 nm, and $w_{\text{eff}} = 1600 \text{ k}_B\text{T}/l_{\text{actin}}^2 = 0.25 \text{ k}_B\text{T}/\text{nm}^2$ [145].

Increasing the effective adhesion strength reduces the first-passage time for the particle. Larger adhesion strengths mean larger forces pushing the particle through the spectrin network, resulting in shorter first-passage times. The time without ankyrin is equal to or more than with ankyrin (Fig. 4.10 (c)). We use $n = 10$, and $R = l_{\text{actin}}$.

4.4 Conclusions and Outlook

We investigated the wrapping of a nanoparticle by the RBC membrane with an underlying spectrin network modelled by a hexagonal network of entropic springs, with and without ankyrin. At equilibrium, the quasistatic energy contribution E_{sp} due to the spectrin network is large for larger particles, because larger particles interact more with the spectrin network. This leads to a large energy barrier. For particles of the same size, E_{sp} increases with n in the absence of ankyrin, while it decreases with n in the presence of ankyrin. The ankyrin complex attaches the spectrin network to the lipid bilayer membrane and reduces the entropy of the spectrin filaments. A reduced number of filament conformations results in a reduced interaction of the particle with the spectrin network, thus the presence of ankyrin favours wrapping.

In order for the particle to get wrapped, the costs due to the spectrin network and membrane deformations have to be overcome by the adhesion energy gains.

We obtain five wrapping regimes for different adhesion strengths. For small adhesion strengths, we obtain no wrapping and find a stable NW state. As we increase the adhesion strength further, we find a metastable CW state along with a stable NW state between the unwrapping spinodal S_{21} for the spontaneous transition between the CW and the NW state, and the binding transition W_1 . The continuous binding transition W_1 occurs at $\tilde{w} = 4$, as for a bare lipid bilayer membrane [10, 85]. It does not change with the number of spectrin beads in the filament, and the presence of the ankyrin, as the particle does not experience any pressure from the spectrin network if it just touches the membrane. For adhesion strengths $w_1 < \tilde{w} < w_2$, we obtain a metastable CW state along with a stable PW state. At $\tilde{w} = w_2$, we find the discontinuous envelopment transition W_2 , characterized by an energy barrier $\Delta\tilde{E}_{\text{barrier}}$. For adhesion strengths larger than w_2 , we find a stable CW state along with a metastable PW state. Increasing \tilde{w} further, $\Delta\tilde{E}_{\text{barrier}}$ between the CW and the PW state vanishes, and we find a stable CW state with a spinodal S_{22} . The presence of ankyrin increases the PW areas, and thus favours wrapping. Our theoretical calculations predict an enhanced stability of PW states for particles interacting with an intact spectrin network of a healthy cell that is also attached to the lipid bilayer via ankyrin.

The first-passage times for the particle to be wrapped completely by the membrane increase with the number of spectrin beads and decrease with the spectrin bead number, without and with ankyrin, respectively. The presence of ankyrin makes the filaments softer, thus they hinder wrapping of large particles less. Increasing the effective adhesion strength favours wrapping and the first-passage times decrease. Larger particles take longer times to pass through the cytoskeletal network. The ankyrin thus facilitates the membrane to wrap the particle.

Larger micron-sized particles can rupture the spectrin network when they pass through it. This rupturing could help the microparticles to enter RBCs. We will discuss spectrin network rupturing by a particle in the next chapter.

Chapter 5

Malaria-like particle-red blood cell interactions

Mathematics is like a whore. She is everywhere, and is easy to enter.

– Karandeep Singh

At least one third of the world's population is at risk of malaria infection, with over 300 million people developing the clinical disease each year and at least 2 million deaths [274]. The malaria parasite is the most important member of the Apicomplexa, a large and highly successful phylum of intracellular parasites [275]. The infection of red blood cells (RBCs) is caused by *Plasmodium* parasites, which are responsible for all malaria disease pathology. The invasion into the RBC by the blood-stage parasite, merozoite is an essential step, and rapid and efficient entry into the host cell is important in the evolutionary success of these pathogens [275]. The merozoite uses an internal molecular motor based on actin and myosin to drive itself into the RBC [276].

The different stages of merozoite invasion are schematically represented in Fig. 5.1. The initial contact between the merozoite and RBC is a crucial step, as the parasite must distinguish between RBCs competent for invasion and other cells. The invasion commences with non-directional binding of the RBC by the merozoite [277]. Primary attachment of the polar merozoite appears to occur at any point on the RBC surface and with any merozoite orientation at this invasion stage (Fig. 5.1 (A)). Reorientation then ensues, such that the merozoite apex directly contacts the target cell [278] (Fig. 5.1 (B)). A short-ranged attraction (4 nm or less) is established, leading to the RBC-merozoite tight junction [279, 280] (Fig. 5.1 (B)). An anchored myosin motor inside the parasite (directly tethered to a cytoskeletal compartment within the cell pellicle) transmits force via short actin filaments, which are linked to surface-bound adhesin [278]. The binding of surface adhesins to RBC receptors and their combined passage towards the base of the merozoite (through the fluid plasma membrane) generates a rearward force driving the parasite forward [275, 278, 281, 282] (Fig. 5.1 (C) and (D)).

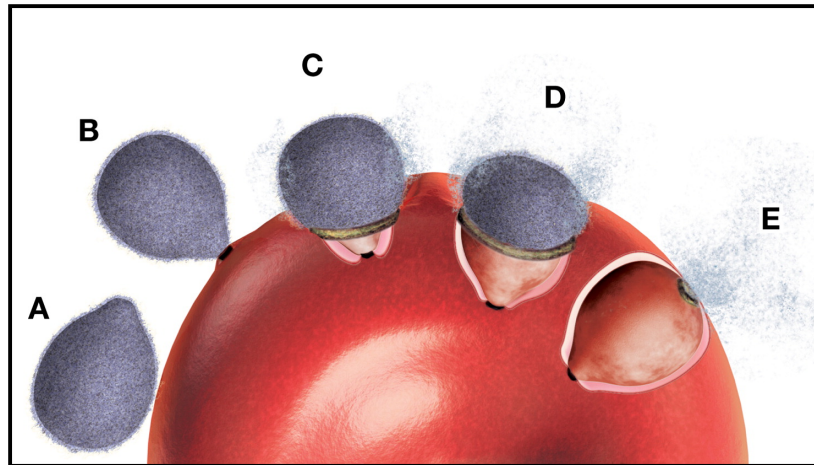


Figure 5.1: Merozoite invasion of red blood cells. Invasion involves an initial long-distance recognition of surface receptors (A) followed by a reorientation process whereby these low affinity contacts are maintained. Once the apical end is adjacent to the erythrocyte (B), a tight junction is formed involving high-affinity ligand receptor interactions. This tight junction then moves from the apical to posterior pole (C and D) powered by the parasite’s actin-myosin motor. The surface coat is shed at the moving junction by a serine protease, or “sheddase.” Upon reaching the posterior pole, the adhesive proteins at the junction are also proteolytically removed (E), this time by a resident protease, most likely a rhomboid, in a process that facilitates resealing of the membrane. By this process, the parasite does not actually penetrate the membrane but invades in a manner that creates a parasitophorous vacuole. Reproduced from Ref. [275].

One of the most conspicuous events is the removal or “shedding” of the fuzzy coating covering the merozoite surface, a proteolytic event involving SUB2, a serine protease localized in the apical microneme organelles [283]. Finally, upon entry into the RBC, the adhesive proteins at the junction are proteolytically removed, which facilitates resealing the membrane [284, 285] (Fig. 5.1 (E)). As the parasite pushes its way into its host cell, it creates a parasitophorous vacuole to seal itself from the host-cell cytoplasm and forms an environment hospitable for its development.

An in-depth view of what happens at the parasite level depicting its motor forces is shown in Fig. 5.2 (left). The parasite breaks or moves aside the RBC cytoskeleton at the site of invasion (to allow entry) [278]. At the specific site of entry, we assume that the cytoskeleton of the RBC gets disassembled, which is experimentally supported by evidence that there is ATP required in the RBC for invasion [286, 287] and later the cytoskeleton reassembles itself via ATP hydrolysis [268, 288]. For mechanically-driven local disassembly of the cytoskeleton, a

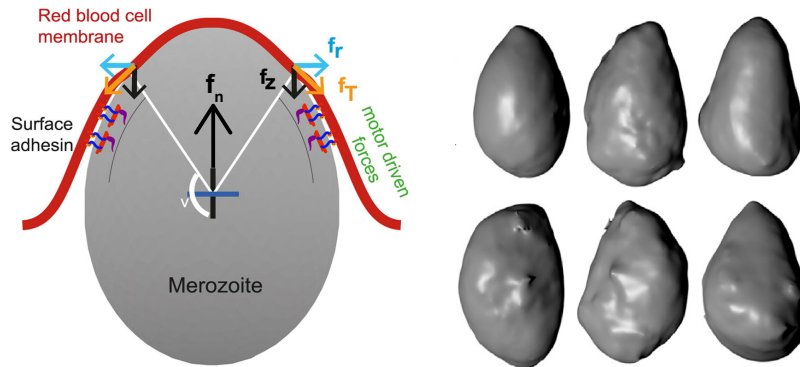


Figure 5.2: Actomyosin force supports merozoite invasion. (left) f_T is the force acting tangentially along the membrane-cortex surface as it wraps along the particle, whereas the f_z is the component of this tangential force along the z axis whose role is to push the particle through the membrane while the component f_r is balanced by an equal magnitude force acting along the other side of the membrane. The component of actomyosin force f_n normal to the membrane pushes the particle through the RBC membrane. Reproduced from Ref. [278]. (right) Isosurface rendered merozoites from cryo-x-ray imaged free *P. falciparum* merozoites cryopreserved in a capillary. Reproduced in part from Ref. [278].

stretching force is required that may be contributed by motor activity.

There have been numerous attempts to understand malaria parasite invasion into RBCs, including models incorporating the breadth of molecular and cellular events. This include models using the identification of two parasite proteins, RON2 and AMA1, essential to trigger junction formation [289], using specific interactions between host receptors and parasite ligands [290], and using fluorescence, three-dimensional structured illumination, and analysis of cellular and molecular events underlying each discrete step of invasion using immunoelectron microscopy of filtered merozoites [291]. However, studies that take into consideration biophysical interactions between host and parasite cells, specifically the role of the RBC membrane and the underlying cytoskeleton, have been scarce [292]. A widely accepted view is that activity of the parasite actomyosin motor alone defines successful host-cell entry. This has been the major reason for ignoring other biophysical interactions [293,294]. Its broad acceptance relies heavily on the general perceived inactivity of mature RBCs [295]. Similarly, the related apicomplexan parasite, *Toxoplasma gondii*, until recently, was believed to invade independently of host-cell remodeling processes [296]. However, a residual level of invasion has been observed in the absence of myosin and actin in *Toxoplasma* [297]. Recently, there have been studies showing that host cell cytoskeletal rearrangements occur during *Toxoplasma* and nonerythroid *Plasmod-*

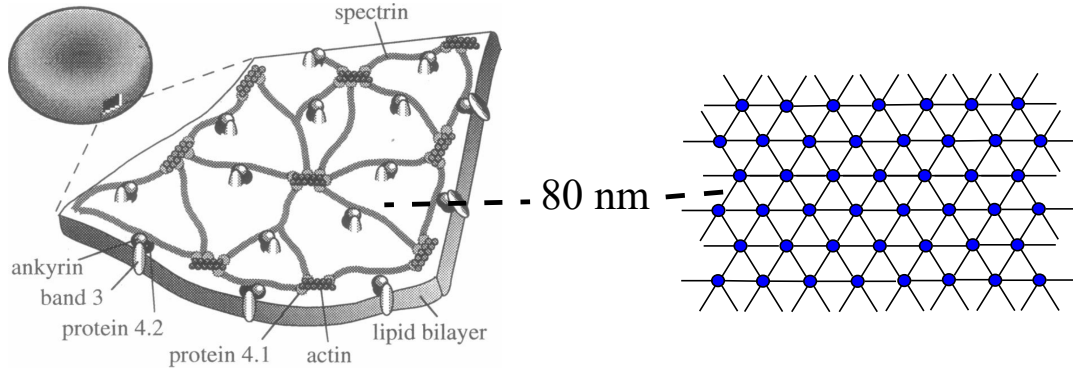


Figure 5.3: Arrangement of the major components of the RBC membrane skeleton (left), and its one-to-one mapping using our RBC spectrin model (right). Left picture reproduced from Ref. [165].

ium invasion [298]. These studies clearly suggest that besides motor-driven force production, host-centered processes are also important. In this chapter, we take into account a combination of RBC membrane dynamics along with motor forces to investigate the complex process of malaria parasite invasion.

The sizes of the particles used in our model vary from 320 nm to 2.4 μm , and the size of a malaria parasite is 1-2 μm (Fig. 5.2 (right)) [299]. We model the RBC cytoskeleton by a network of springs, and *Plasmodium* is modelled using a sphere. We first revisit the RBC cytoskeleton network and discuss the parameters involved in the wrapping process.

5.1 Simulating the particle-spectrin interaction

We perform Brownian Dynamics simulations to investigate the interaction of a particle that is large compared with the length of a spectrin bond with the RBC spectrin network. We model the RBC spectrin cytoskeleton by a network of Hookean springs, where each node represents a junction complex, and each spring represents a spectrin bond (Fig. 5.3). Each node is connected to six other nodes, resulting in a hexagonal network. We simulate a rectangular patch of spectrin network with dimensions 50×50 squared simulation units (su), where $1 \text{ su} = 80 \text{ nm}$, the spectrin bond length is $l_{\text{actin}} = 80 \text{ nm}$ [268,269], and the spectrin contour length is $l_c = 200 \text{ nm}$ [174].¹ The force exerted by a spring on each node

¹The bending rigidity of the spectrin network, a highly flexible structure with bending rigidity $\kappa \approx 0.024 - 0.24 \text{ k}_B\text{T}$ [300,301], is two orders of magnitude smaller than the bending rigidity of the lipid bilayer $\kappa \approx 50 \text{ k}_B\text{T}$ [174,302]. Therefore it does not have to be modeled explicitly. Moreover, the in-plane shear energy that a RBC can store is $\approx 10^5 \text{ k}_B\text{T}$, which far exceeds the total bending energy it stores ($\approx 10^3 \text{ k}_B\text{T}$) for bending modulus $\kappa \approx 50 \text{ k}_B\text{T}$

5.1 Simulating the particle-spectrin interaction

F_{sp} is given by Hooke's law,

$$F_{\text{sp}} = -k_{\text{sp}}(l - l_{\text{eq}}), \quad (5.1)$$

where l is the actual length of the spring, l_{eq} is its equilibrium length, and k_{sp} is its spring constant. For a uniform network of springs that are connected at six-fold coordinated junctions, the shear modulus is [174]

$$\mu = \frac{\sqrt{3}k_{\text{sp}}}{4}. \quad (5.2)$$

This applies for small deformations of an unstretched network. We benchmark our simulations by calculating the shear modulus of the network and comparing it with Eq. 5.2, see Appendix B. For our particle-wrapping calculations, we choose the spring constant $k_{\text{sp}} = 96 \text{ k}_B\text{T}/l_{\text{actin}}^2$ for the spectrin bonds, which falls in the range of spring constant values reported in the literature [268, 303–305].

The particle is modelled by a sphere with radius R , and the nodes of the spring network by spheres with radii $R_{\text{sp}} = 16 \text{ nm}$ [174]. They experience frictions ζ_{p} and ζ_{sp} , which correspond to diffusion coefficients D_{p} and D_{sp} , respectively. The repulsive interaction force between the particle and each spring node is the modified truncated Lennard-Jones potential,

$$F_{\text{ij}} = \begin{cases} \frac{12\epsilon}{r-(R-R_{\text{sp}})} \left[\left(\frac{r_{\text{min}}}{r-(R-R_{\text{sp}})} \right)^{12} - \left(\frac{r_{\text{min}}}{r-(R-R_{\text{sp}})} \right)^6 \right], & r \leq r_{\text{min}} \\ 0, & r > r_{\text{min}} \end{cases} \quad (5.3)$$

with interparticle distance r , distance $r_{\text{min}} = 2^{7/6}R_{\text{sp}}$ at which the potential reaches its minimum, and Lennard-Jones force strength ϵ . We use $\epsilon = 1 \text{ k}_B\text{T}$.

The actomyosin motors push the particle through the membrane. We identify neighbours of vertices in contact with the particle as motor vertices, see Fig. 5.4. Thus the net motor force on the particle in $-z$ direction is

$$F_{\text{m}} = f_{\text{m}}N_{\text{m}}, \quad (5.4)$$

with force f_{m} per motor vertex, and N_{m} motor vertices. Figure 5.5 indicates the positive z direction for the system.

The adhesion force between the particle and the membrane is modelled as constant force

$$F_{\text{ad}} = 2\pi R w_{\text{eff}} \quad (5.5)$$

acting on the particle in $-z$ direction, with the effective particle-membrane adhesion strength $w_{\text{eff}} = w - \kappa/A$, where κ is the bending rigidity of the membrane, w is adhesion strength between the particle and the membrane, and A is the surface area of the particle. According to Newton's third law, the particle adhesion force

[163, 265, 272, 273].

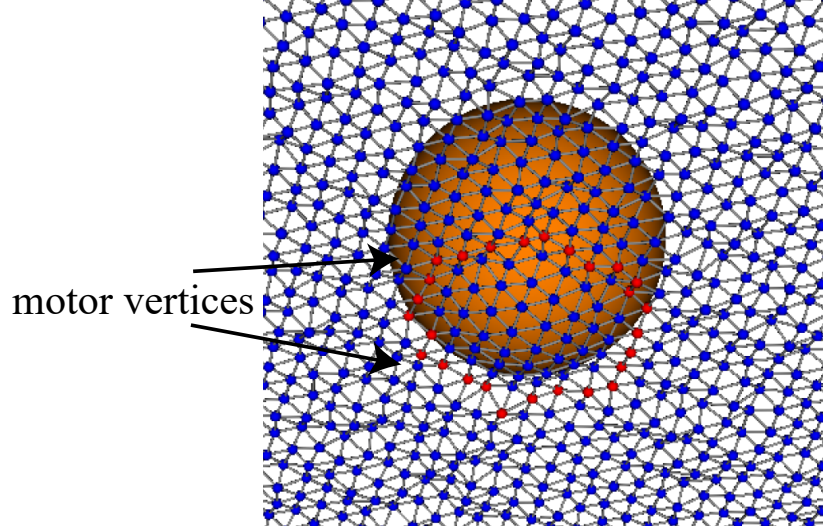


Figure 5.4: A particle interacting with a spectrin network. The marked red points are the motor vertices.

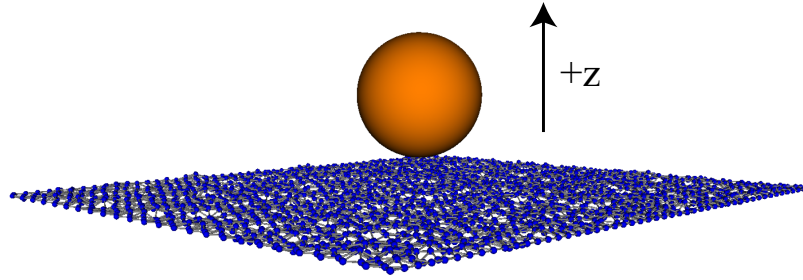


Figure 5.5: A particle next to a spectrin network, with the $+z$ direction marked.

F_{ad} acts on the motor vertices in the opposite direction as on the particle, equally distributed over the N_m motor vertices.

The dynamics of the particle and the spring nodes is calculated using Brownian dynamics,

$$\begin{aligned}\zeta_p \partial_t r_p &= -F_{\text{ad}} - F_m + F_{\text{lj}} + \sqrt{2\zeta_p kT} \eta_p(t), \\ \zeta_{\text{sp}} \partial_t r_{\text{sp}} &= F_{\text{sp}} + f_m + \frac{F_{\text{ad}}}{N_m} - F_{\text{lj}} + \sqrt{2\zeta_{\text{sp}} kT} \eta_{\text{sp}}(t)\end{aligned}\tag{5.6}$$

with the friction coefficients ζ_p and ζ_{sp} for the particle in solution and for the spring nodes, respectively. The Gaussian white noises $\eta_p(t)$ and $\eta_{\text{sp}}(t)$ have zero mean $\langle \eta(t) \rangle = 0$, and $\langle \eta(t) \eta(t') \rangle = 2B \delta(t - t')$, where B is the strength of the random noise. Following the Fluctuation-dissipation theorem, $B = \zeta k_B T$. Using Stokes friction for spherical particles, $D = kT/\zeta$, we can express the above

equations in terms of the diffusion coefficients for the particle and the springs, D_p and D_{sp} , respectively. For the particle sizes used in our simulations, the particle diffusion coefficients in water are $D_p = 1.27 \mu\text{m}^2/\text{s}$ for 320 nm particles, $D_p = 0.51 \mu\text{m}^2/\text{s}$ for 800 nm particles, $D_p = 0.25 \mu\text{m}^2/\text{s}$ for 1.6 μm particles, and $D_p = 0.17 \mu\text{m}^2/\text{s}$ for 2.4 μm particles. Experimentally measured diffusion coefficients for proteins and lipids in RBC membranes and in model lipid bilayers are in the range of $0.25 \mu\text{m}^2/\text{s} \leq D_{sp} \leq 13.2 \mu\text{m}^2/\text{s}$, see Section 2.3 in Chapter 2. We assume $D_p/D_{sp} = 1$, and $\zeta_p/\zeta_{sp} = 1$. The lengths in simulations and experiments are connected via the particle diameters, d_p and d_{sim} . The time scales in simulations and water are connected using $t_p = (D_{sim}d_p^2)/(D_p d_{sim}^2)t_{sim}$ for typical values of particle diffusion coefficients, D_p calculated using the Stokes friction for a spherical particle in water and D_{sim} for the particle in simulation units. The equations of motion for NPs and receptors are integrated using the Euler algorithm and the time step corresponds to $\Delta t = 25.6$ ns for particles with $R = 800$ nm [206].

5.2 Particle-membrane interactions

We systematically study the effects of the force per motor vertex f_m , the effective adhesion strength w_{eff} , and the particle radius R on wrapping of the particle by the membrane. The particle breaks through the spring network, as a malaria parasite breaks through the spectrin cytoskeleton, in order to allow the particle to pass through the membrane. We study two different spring breaking lengths, $l_{bsp} = 1.5 l_{actin}$, and $l_{bsp} = l_c = 2.5 l_{actin}$, and investigate how it affects the particle wrapping by the membrane. We identify two different wrapping mechanisms depending on the breaking length of a spring. Simulation snapshots for a particle passing through the spectrin network for two different breaking lengths l_{bsp} are shown in Figs. 5.6 and 5.7. A particle interacts with the spectrin network and breaks through it. For $w_{eff} = 0$, f_m required in order that we obtain a completely-wrapped (CW) state for all particle sizes, $R = 2, 5, 10, 15 l_{actin}$ is $75 k_B T/l_{actin}^2$. In the case of $l_{bsp} = 1.5 l_{actin}$ (Fig. 5.6), the springs break as the particle is traversing through the network. Whereas in the case of $l_{bsp} = 2.5 l_{actin}$ (Fig. 5.7) the particle is initially stuck inside the network in a partial-wrapped (PW) state. It constantly pushes against the springs, and eventually breaks through the spectrin network, resulting in a CW state.

5.2.1 Particle wrapping fraction versus time

We plot f_w as function of time for different radii of the particle, and for different spring breaking lengths, for constant adhesion force (Fig. 5.8). For $f_m = 0$, w_{eff} required to obtain a CW state for all the particle sizes is $85 k_B T/l_{actin}^2$. The particle passage time for $l_{bsp} = 1.5 l_{actin}$ is shorter compared to $l_{bsp} = 2.5 l_{actin}$,

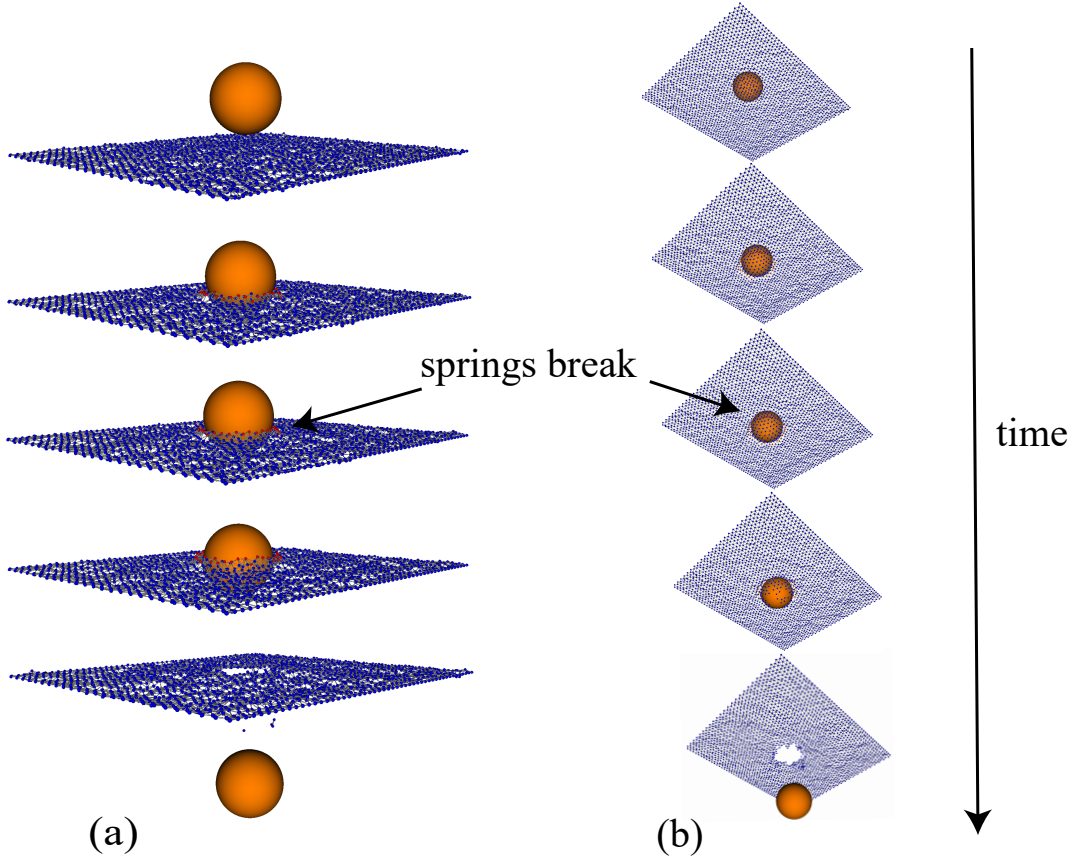


Figure 5.6: Simulation snapshots of particle passage through the spectrin network. (a) Side view and (b) bottom view of the network. Effective adhesion strength $w_{\text{eff}} = 0$, force per motor vertex $f_m = 75 k_B T / l_{\text{actin}}^2$, and $l_{\text{bsp}} = 1.5 l_{\text{actin}}$.

as the springs break easier in the former compared to the latter. We identify two different partial-wrapped (PW) states for $l_{\text{bsp}} = 1.5 l_{\text{actin}}$: partial wrapping with an intact spring network $\underline{\text{PW}}$, and partial wrapping with a broken spring network $\overline{\text{PW}}$. For $l_{\text{bsp}} = 2.5 l_{\text{actin}}$, the $\overline{\text{PW}}$ state is almost non-existent, and partial wrapping is mostly dominated by $\underline{\text{PW}}$. The particle is initially stuck in a $\underline{\text{PW}}$ state, and as soon as the first spring in the network breaks, the particle is able to push through the spectrin network, and jumps to a CW state. The particle passage time through the spectrin network for smaller particles is shorter, as compared to the larger ones, and the threshold f_w at which the particle escapes the spectrin network, occurs at larger wrapping fractions for smaller particles (Fig. 5.8). A characteristic of the $l_{\text{bsp}} = 2.5 l_{\text{actin}}$ case is the plateau in the wrapping fraction (Fig. 5.8 (b)), which depicts a trapped particle in the spectrin network, before it is finally released; we do not observe a plateau in the wrapping fraction for the $l_{\text{bsp}} = 1.5 l_{\text{actin}}$ case.

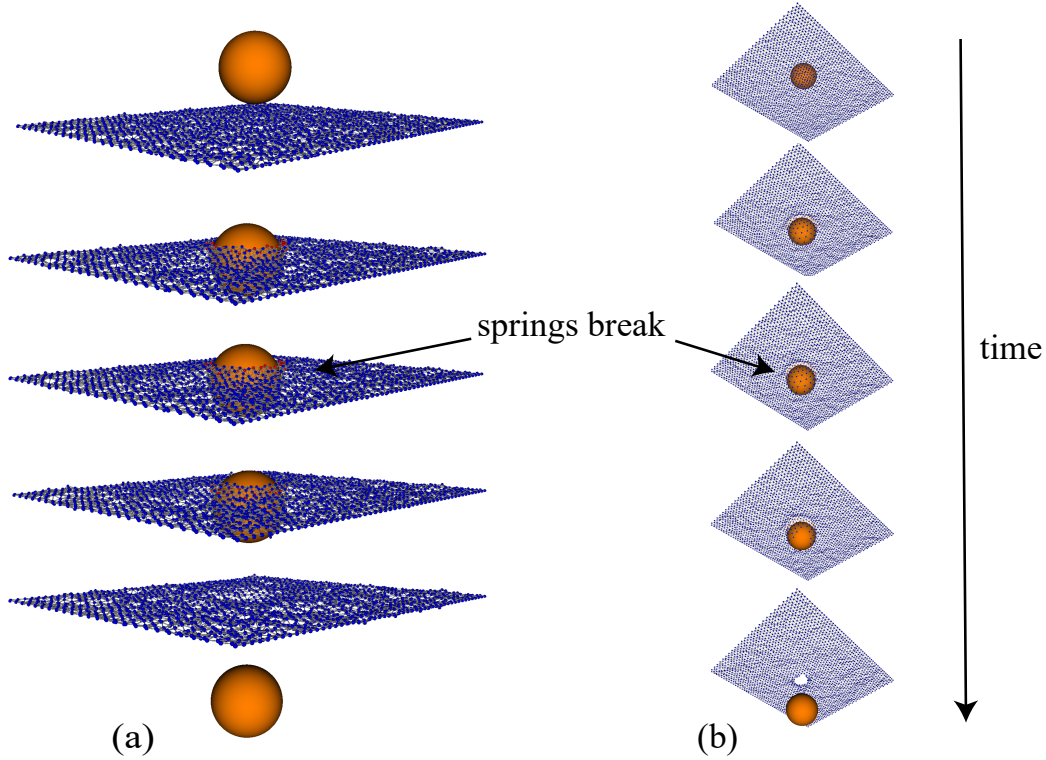


Figure 5.7: Simulation snapshots of particle passage through the spectrin network. (a) Side view and (b) bottom view of the network. Effective adhesion strength $w_{\text{eff}} = 0$, force per motor vertex $f_m = 75 \text{ k}_B \text{T} / l_{\text{actin}}^2$, and $l_{\text{bsp}} = 2.5 l_{\text{actin}}$.

5.2.2 Varying adhesion strength and motor forces

We plot f_w for stable PW and CW states versus w_{eff} for vanishing f_m , and for different spectrin breaking lengths $l_{\text{bsp}} = 1.5 l_{\text{actin}}$ (Fig. 5.9 (a)) and $l_{\text{bsp}} = 2.5 l_{\text{actin}}$ (Fig. 5.9 (b)). The radius R of the particle is $5 l_{\text{actin}}$. For small adhesion strengths, the wrapping fraction f_w of stable partial-wrapped (PW) states increases with w_{eff} . We find power laws for the f_w increase at small adhesion strengths, $f_w = 0.04 w_{\text{eff}}^{0.7}$ and $f_w = 0.06 w_{\text{eff}}^{0.54}$ for $l_{\text{bsp}} = 1.5 l_{\text{actin}}$ and $l_{\text{bsp}} = 2.5 l_{\text{actin}}$, respectively. The exponent for $l_{\text{bsp}} = 1.5 l_{\text{actin}}$ is larger than the exponent for $l_{\text{bsp}} = 2.5 l_{\text{actin}}$. For the same adhesion force, the springs for $l_{\text{bsp}} = 1.5 l_{\text{actin}}$ will break faster compared to $l_{\text{bsp}} = 2.5 l_{\text{actin}}$, thus resulting in a larger power law exponent in former compared to the latter. Increasing w_{eff} further, we reach a critical adhesion strength $w = w_{\text{eff}}^*$ at which the spectrin bonds break, and we observe a wrapping transition from PW state to a CW state via a PW state. As seen before, for $l_{\text{bsp}} = 2.5 l_{\text{actin}}$, partial wrapping is mostly dominated by PW, and the particle directly jumps to a CW state. We obtain $w_{\text{eff}}^* = 13 \text{ k}_B \text{T} / l_{\text{actin}}^2$ and $w_{\text{eff}}^* = 80 \text{ k}_B \text{T} / l_{\text{actin}}^2$, for $l_{\text{bsp}} = 1.5 l_{\text{actin}}$, and $l_{\text{bsp}} = 2.5 l_{\text{actin}}$, respectively. Thus, in the absence of motor

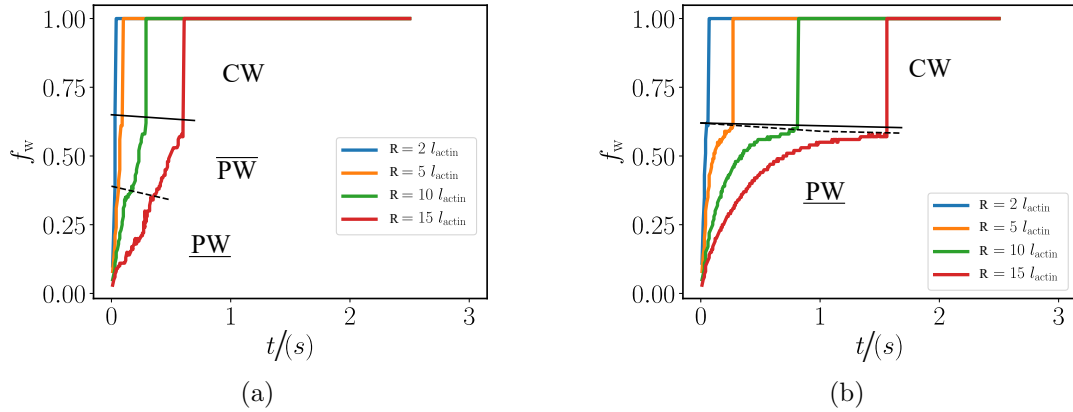


Figure 5.8: Particle wrapping fraction f_w as function of time for particle radii $= 2, 5, 10,$ and $15 l_{\text{actin}}$ for (a) $l_{\text{bsp}} = 1.5 l_{\text{actin}}$ and (b) $l_{\text{bsp}} = 2.5 l_{\text{actin}}$. We use effective adhesion strength $w_{\text{eff}} = 85 k_B T / l_{\text{actin}}^2$, and motor force $f_m = 0$ in both the cases. The dashed black line indicates the wrapping fraction f_w when the first spring breaks, and the solid black line the wrapping fraction when the particle transits to a CW state.

forces, the adhesion strength between the particle and the membrane must be at least $w = w_{\text{eff}}^*$, in order for the membrane to wrap around the particle.

Further, we plot the wrapping fraction f_w versus f_m for vanishing w_{eff} , and for spectrin breaking lengths $l_{\text{bsp}} = 1.5 l_{\text{actin}}$ (Fig. 5.10 (a)) and $l_{\text{bsp}} = 2.5 l_{\text{actin}}$ (Fig. 5.10 (b)). The radius R of the particle is $5 l_{\text{actin}}$. We obtain very similar behaviours for varying f_m , as in the case of changing w_{eff} . For small forces per motor vertex, the wrapping fraction f_w increases with f_m , and the particle is partially wrapped (PW). We find power laws for the f_w increase at small adhesion strengths; $f_w = 0.03 f_m^{0.9}$ and $f_w = 0.07 f_m^{0.49}$ for $l_{\text{bsp}} = 1.5 l_{\text{actin}}$ and $l_{\text{bsp}} = 2.5 l_{\text{actin}}$, respectively. The exponent for $l_{\text{bsp}} = 1.5 l_{\text{actin}}$ is larger than the exponent for $l_{\text{bsp}} = 2.5 l_{\text{actin}}$, similar to the case of vanishing f_m . We obtain critical forces per motor vertex $f_m^* = 10 k_B T / l_{\text{actin}}^2$ and $f_m^* = 67 k_B T / l_{\text{actin}}^2$, for $l_{\text{bsp}} = 1.5 l_{\text{actin}}$, and $l_{\text{bsp}} = 2.5 l_{\text{actin}}$, respectively.

The wrapping fraction f_w of the particle increases for small adhesion strengths $w_{\text{eff}} < w_{\text{eff}}^*$ and small motor forces $f_m < f_m^*$ resulting in stable PW states (PW). All the spectrin bonds are still intact. At $w_{\text{eff}} = w_{\text{eff}}^*$ for $f_m = 0$, and $f_m = f_m^*$ for $w_{\text{eff}} = 0$, the first spectrin bond breaks. The difference in the wrapping fractions when the first spectrin bond breaks and when the particle jumps to a CW state is larger for $l_{\text{bsp}} = 1.5 l_{\text{actin}}$ compared to $l_{\text{bsp}} = 2.5 l_{\text{actin}}$, as the spectrin bonds break faster for former compared to the latter.

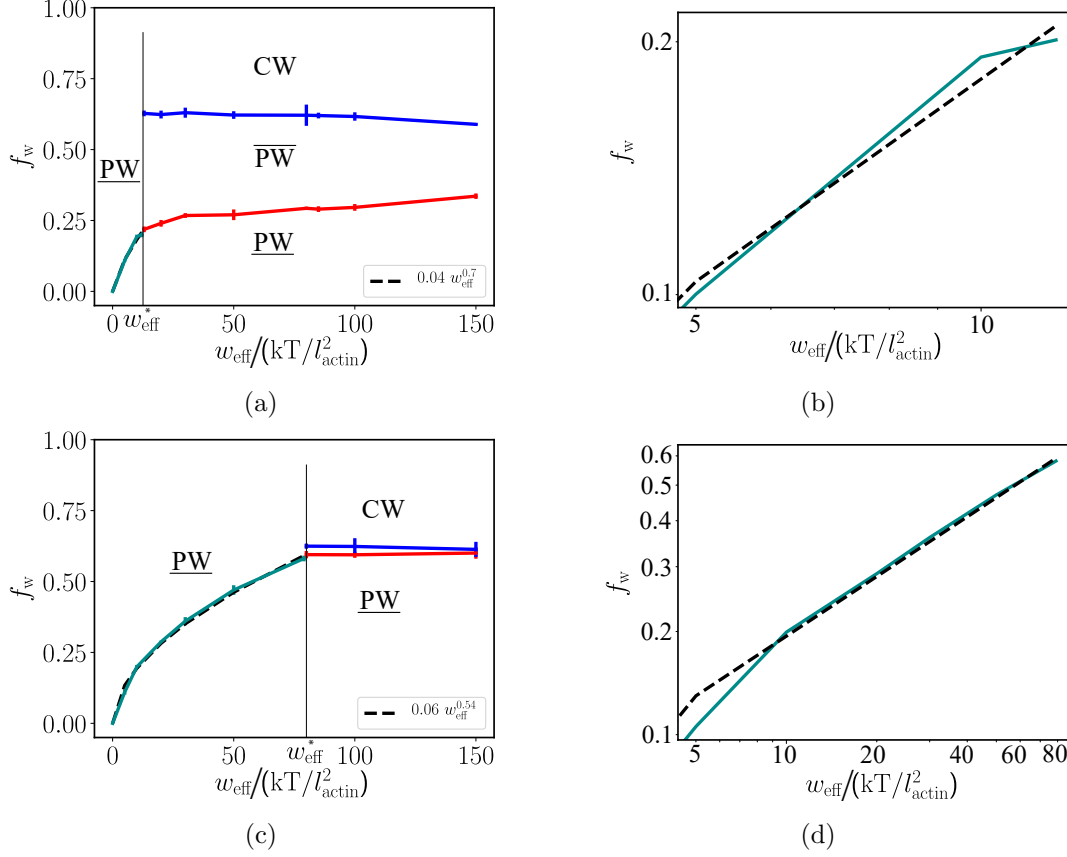


Figure 5.9: Particle wrapping fraction f_w as function of effective adhesion strength w_{eff} for vanishing f_m , $R = 5 l_{\text{actin}}$, and for (a-b) $l_{\text{bsp}} = 1.5 l_{\text{actin}}$ and (c-d) $l_{\text{bsp}} = 2.5 l_{\text{actin}}$. The plots (b) and (d) correspond to the power law fits for the corresponding PW states. The cyan lines along with the power law fits (black dashed lines) characterise the wrapping fractions for small effective adhesion strengths. The red lines characterise the particle f_w when the first spectrin bond breaks. The blue lines correspond to the particle wrapping fraction f_w before the particle jumps from a partial-wrapped state to a complete-wrapped state. The solid black vertical line marks the critical adhesion strength w_{eff}^* , at which the spectrin bonds break and the particle jumps from a PW state to a CW state.

5.2.3 Particle wrapping fraction versus particle radius

We plot f_w of stable PW and CW states as function of R for spectrin breaking lengths, $l_{\text{bsp}} = 1.5 l_{\text{actin}}$ (Fig. 5.11 (a)) and $l_{\text{bsp}} = 2.5 l_{\text{actin}}$ (Fig. 5.11 (b)). We use an effective adhesion strength $w_{\text{eff}} = 85 k_B T / l_{\text{actin}}^2$, and force per motor vertex $f_m = 0$ in both the cases. For $l_{\text{bsp}} = 1.5 l_{\text{actin}}$, we observe both partial-wrapped states, PW and $\overline{\text{PW}}$, as the particle passes through the membrane. There is a large difference between the wrapping fractions when the first spring breaks and when the particle escapes. On the contrary, for $l_{\text{bsp}} = 2.5 l_{\text{actin}}$, the particle is

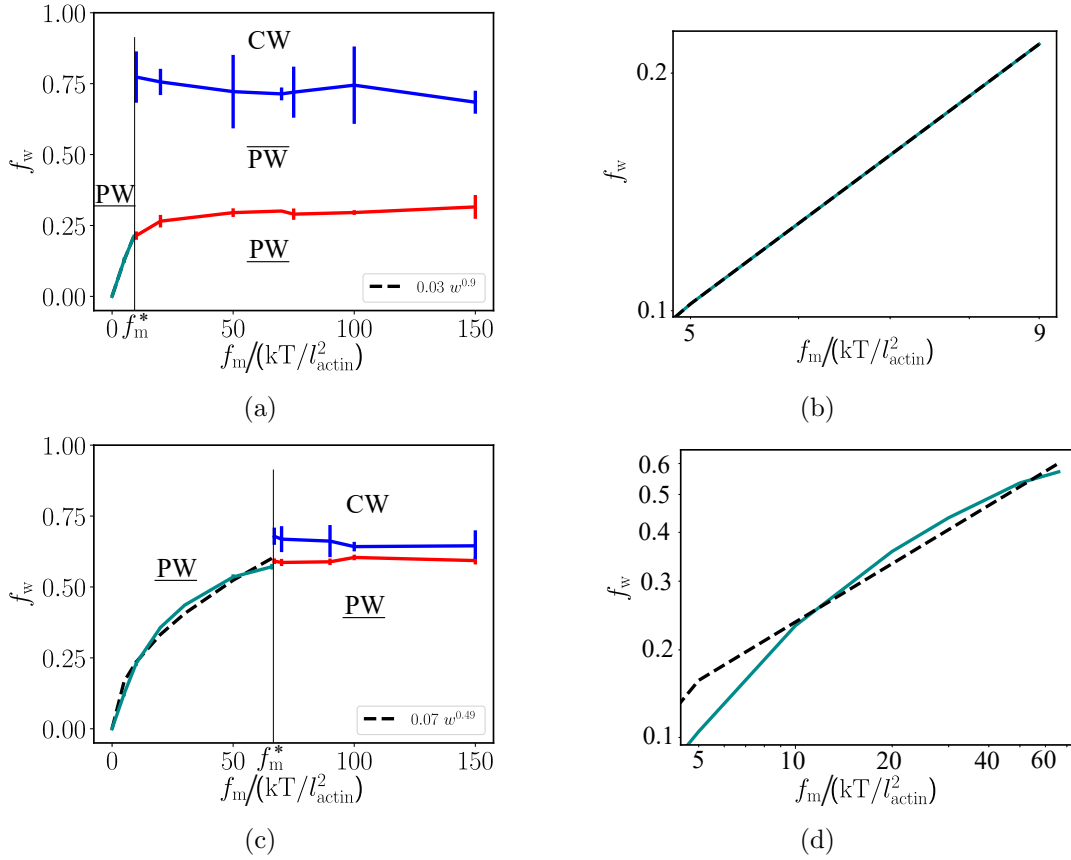


Figure 5.10: Particle wrapping fraction f_w as function of force per motor vertex f_m for vanishing effective adhesion strength w_{eff} , $R = 5 l_{\text{actin}}$, and for (a-b) $l_{\text{bsp}} = 1.5 l_{\text{actin}}$ and (c-d) $l_{\text{bsp}} = 2.5 l_{\text{actin}}$. The plots (b) and (d) correspond to the power law fits for the corresponding $\overline{\text{PW}}$ states. The cyan lines along with the power law fits (black dashed lines) characterise the wrapping fractions for small effective adhesion strengths. The red lines characterise the particle f_w when the first spectrin bond breaks. The blue lines correspond to the particle wrapping fraction f_w before the particle jumps from a partial-wrapped state to a completely-wrapped state. The solid black vertical line marks the critical adhesion strength f_m^* , at which the spectrin bonds break and the particle jumps from a PW state to a CW state.

stuck in a $\overline{\text{PW}}$ state for wrapping fractions $0 < f_w \leq 0.6$, before the first spectrin bond breaks, and the particle escapes from the spectrin network, characterised by a jump from a $\overline{\text{PW}}$ to a CW state. The $\overline{\text{PW}}$ regime is very small compared with the PW regime. We do not observe two different PW states, as the difference between the wrapping fractions when the first spring breaks and when the particle escapes is almost negligible, compared to the former. The wrapping fraction f_w decreases with R , as smaller particles stretch the network less for the same f_w ,

5.3 Particle wrapping phase diagrams

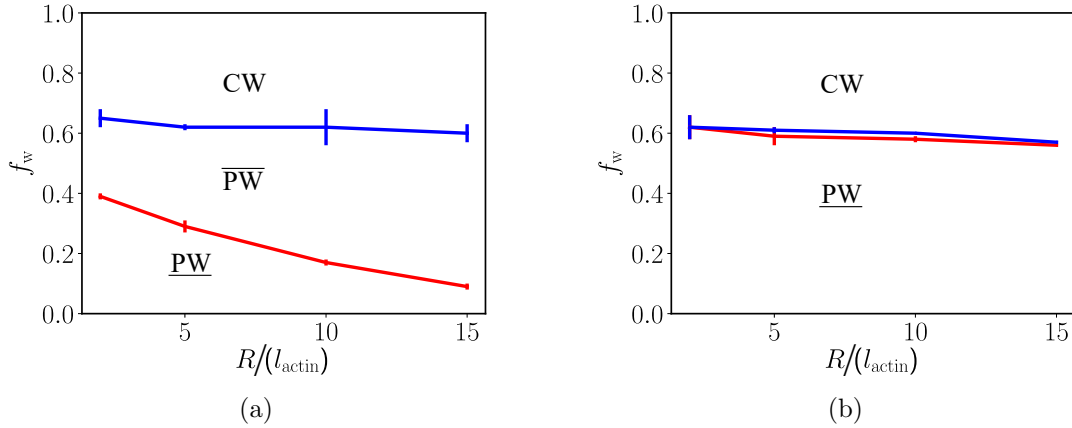


Figure 5.11: Particle wrapping fraction f_w as function of radius R of the particle for (a) $l_{\text{bsp}} = 1.5 l_{\text{actin}}$ and (b) $l_{\text{bsp}} = 2.5 l_{\text{actin}}$. The effective adhesion strength $w_{\text{eff}} = 85 k_B T / l_{\text{actin}}^2$, and motor force $f_m = 0$ for both the cases. The red lines characterise the particle f_w when the first spectrin bond breaks. The blue lines correspond to the particle wrapping fraction f_w before the particle jumps from a partial-wrapped state to a complete-wrapped state.

compared to larger particles.

5.3 Particle wrapping phase diagrams

We obtain partial wrapping of the particle by the RBC membrane for small f_m and w_{eff} , and complete wrapping of the particle for large f_m and w_{eff} , see Figs. 5.12 and 5.13. For $l_{\text{bsp}} = 1.5 l_{\text{actin}}$ (Fig. 5.12), the particle requires only a small force to push it through the membrane in order to be completely wrapped by the membrane, resulting in a small partial-wrapped region compared to $l_{\text{bsp}} = 2.5 l_{\text{actin}}$ (Fig. 5.13). We obtain the envelopment transitions at $w_{\text{eff}} \approx 0.0031 k_B T / \text{nm}^2$ and $f_m \approx 0.0023 k_B T / \text{nm}^2$ for $l_{\text{bsp}} = 1.5 l_{\text{actin}}$; for $l_{\text{bsp}} = 2.5 l_{\text{actin}}$, we obtain the transitions at $w_{\text{eff}} \approx 0.012 k_B T / \text{nm}^2$ and $f_m \approx 0.011 k_B T / \text{nm}^2$. Increasing the particle radius R makes it difficult for the particle to pass through the cortical cytoskeleton as more spectrin bonds need to be broken, thus requiring larger forces pushing the particle.

5.4 Cytoskeletal crack patterns

The crack patterns for the RBC spectrin network after the particle has traversed through it show broken spectrin bonds (Fig. 5.14). We use an effective adhesion strength $w_{\text{eff}} = 0$, and force per motor vertex $f_m = 75 k_B T / l_{\text{actin}}^2$. We obtain very different crack patterns for different spectrin breaking lengths and particle

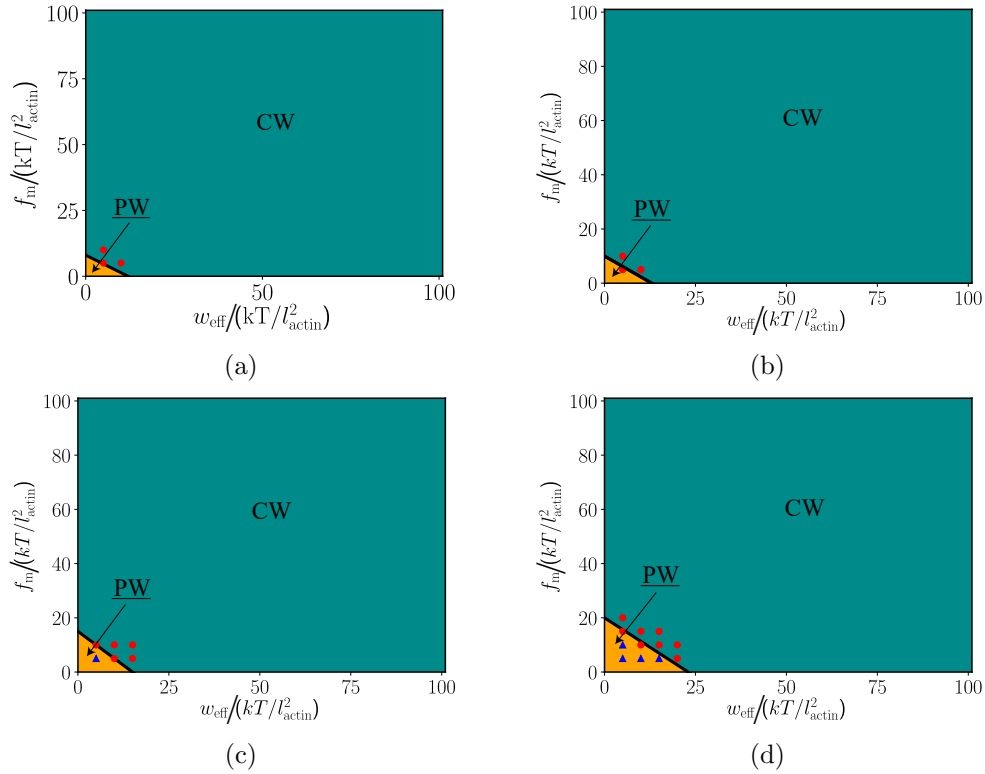


Figure 5.12: Wrapping phase diagram as function of force per motor vertex f_m , effective adhesion strength w_{eff} for (a) $R = 2 l_{\text{actin}}$, (b) $R = 5 l_{\text{actin}}$, (c) $R = 10 l_{\text{actin}}$, and (d) $R = 15 l_{\text{actin}}$. Spectrin breaking length $l_{\text{bsp}} = 1.5 l_{\text{actin}}$. The orange area represents PW region and dark cyan area CW region. The blue triangles denote simulation data with PW states, and red points denote simulation data with CW states.

radii. For $l_{\text{bsp}} = 1.5 l_{\text{actin}}$ (Figs. 5.14 (a-d)), the number of broken springs is much larger compared to $l_{\text{bsp}} = 2.5 l_{\text{actin}}$ (Figs. 5.14 (e-h)). For short l_{bsp} , the springs break earlier while the particle is traversing through the spectrin network and the cracks are distributed throughout the particle projected area on the network. For longer l_{bsp} , the particle is stuck in a PW state, until a small number of springs will break, just enough to allow the network to relax and to let the particle pass through the network. For fixed l_{bsp} , increasing particle radius results in increased number of broken springs in the RBC spectrin network.

The smaller number of broken spectrin bonds for long breaking length might facilitate ‘healing’ of the cytoskeleton network after wrapping of the particle/invasion of the parasite [306]. It has been hypothesized that the RBC shape is controlled by ATP-induced cytoskeletal defects [268, 269, 288, 307], and RBCs recover their shapes after deformation by optical tweezers [272, 308–310]. These observations hint to RBC cytoskeleton remodelling. The broken cytoskeletal network after par-

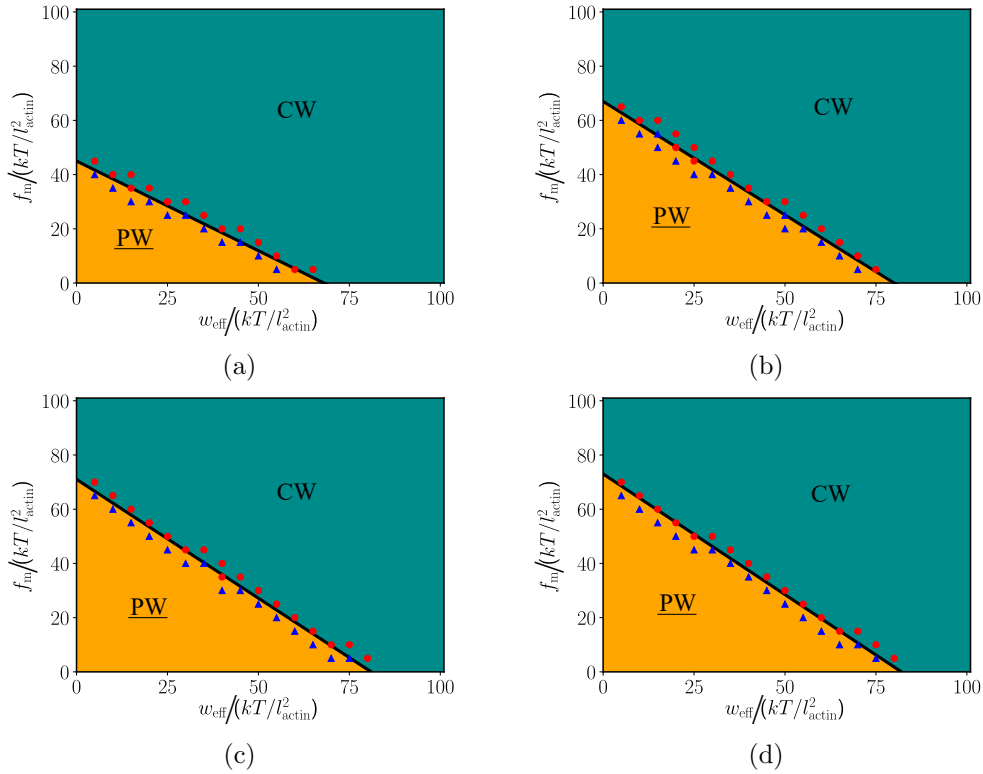


Figure 5.13: Wrapping phase diagram as function of force per motor vertex f_m , effective adhesion strength w_{eff} for (a) $R = 2 l_{\text{actin}}$, (b) $R = 5 l_{\text{actin}}$, (c) $R = 10 l_{\text{actin}}$, and (d) $R = 15 l_{\text{actin}}$. Spectrin breaking length $l_{\text{bsp}} = 2.5 l_{\text{actin}}$. The orange area represents PW region and dark cyan area CW region. The blue triangles denote simulation data with PW states, and red points denote simulation data with CW states.

ticle uptake (shown by the crack patterns), could thus undergo remodelling. For $l_{\text{bsp}} = 1.5 l_{\text{actin}}$, the spectrin network needs to reform a larger number of spectrin bonds compared to the $l_{\text{bsp}} = 2.5 l_{\text{actin}}$ where less number of bonds are broken. If the RBC cytoskeleton ‘heals’ itself after the particle uptake, the ‘healing’ process will be most efficient for a long spectrin breaking length ($l_{\text{bsp}} = 2.5 l_{\text{actin}}$) and a small particle radius ($R = 2 l_{\text{actin}}$).

5.5 Conclusions and Outlook

We investigate malaria-like particle-RBC interactions with an underlying spectrin network. We model the RBC cytoskeleton by a hexagonal network of springs, where each node is connected to six other nodes. Large forces per motor vertex and large adhesion strengths facilitate wrapping of the particle by the membrane, and the time required for a particle to pass through the spectrin network

is shorter. The spectrin bonds could detach from the actin complexes at breaking lengths shorter than the contour length. For short spectrin breaking length, the spectrin bonds break while the particle is traversing through the network, while for longer breaking length, the spectrin bonds break after the particle is already stuck in a PW state, leading to different wrapping dynamics in both the cases. We thus identify two different PW states: partial wrapping with intact spring network $\underline{\text{PW}}$, and partial wrapping with broken spring network $\overline{\text{PW}}$. For long spectrin breaking length, the particle only attains the $\underline{\text{PW}}$ state, whereas for shorter breaking length, we observe both $\underline{\text{PW}}$ and $\overline{\text{PW}}$ states. Small particles reach partial-wrapped states with broken bonds at large wrapping fractions compared with larger particles. Also, small particles traverse faster through the RBC spectrin network compared with larger particles. We identify critical adhesion strengths for vanishing motor forces, and critical motor forces for vanishing adhesion strengths beyond which the particle gets completely wrapped by the membrane.

The wrapping phase diagrams for varying motor forces and effective adhesion strengths for different particle radii and spectrin breaking lengths show that for short breaking lengths, the particles require smaller motor forces and adhesion strengths in order to get completely wrapped by the membrane, thus resulting in a smaller PW region compared with longer breaking length. For fixed spectrin breaking length, increasing particle sizes increases the PW region in the phase diagram. The cytoskeletal crack patterns after complete wrapping of particles with broken spectrin bonds show that large particles break more bonds compared to smaller particles. For short breaking length, there are more broken spectrin bonds compared to longer breaking length. This suggests that ‘healing’ of the cytoskeleton after complete wrapping is more efficient for small particle radii and long spectrin breaking length via cytoskeleton remodelling, where spectrin bonds break and reconnect.

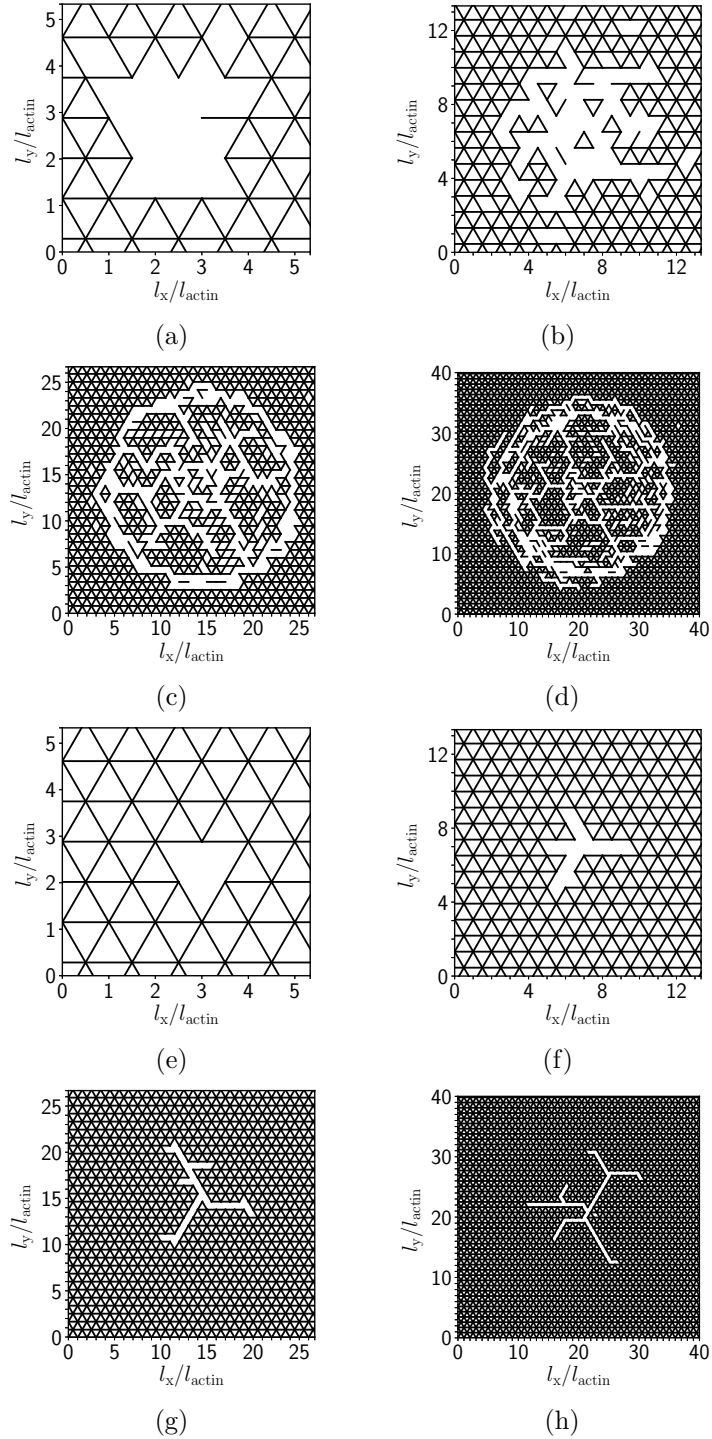


Figure 5.14: Break patterns for the RBC spectrin network after the particle has passed through it. Spectrin breaking length $l_{\text{bsp}} = 1.5 l_{\text{actin}}$ for (a) $R = 2 l_{\text{actin}}$, (b) $R = 5 l_{\text{actin}}$, (c) $R = 10 l_{\text{actin}}$, and (d) $R = 15 l_{\text{actin}}$. Spectrin breaking length $l_{\text{bsp}} = 2.5 l_{\text{actin}}$ for (e) $R = 2 l_{\text{actin}}$, (f) $R = 5 l_{\text{actin}}$, (g) $R = 10 l_{\text{actin}}$, and (h) $R = 15 l_{\text{actin}}$. We use an effective adhesion strength $w_{\text{eff}} = 0$, and force per motor vertex $f_m = 75 \text{ k}_B\text{T}/l_{\text{actin}}^2$. The sizes of the network patches that are plotted are $2.67R$ in all cases. 109

Chapter 6

Conclusions and Outlook

A little magic can take you a long way.

– Roald Dahl

In this work, I have studied the interaction of nano- and microstructures with cells, particularly red blood cells (RBCs). The plasma membrane of red blood cells is supported only by a cortical cytoskeleton similar to other mammalian cell membranes, but RBCs have been characterized extensively. This makes them ideal model systems to study nanoparticle (NP)-cell membrane interactions. The particle-RBC interaction depends on the membrane deformation energy, the particle-membrane adhesion energy, and the energy contribution due to the spectrin network. For inhomogeneous adhesion, e. g. mediated via receptor-ligand bonds between membrane and particle, free-energy contributions due to the receptor entropy also have to be taken into account for.

Nanoparticle-decorated RBCs reveal that particle size controls adsorption, cell shape, and cell deformability. The NP adsorption on the RBC surface saturates at high NP concentrations in bulk for the same adhered membrane area irrespective of NP size: only up to 2 % of the RBC surface is covered with NPs for three sizes of NPs, 27 nm, 45 nm, and 100 nm. The experimentally observed lack of detachment of NPs from the RBCs hints that the concentration dependence is determined by a kinetic mechanism rather than Langmuir isotherms. Both, the sparse coverage of RBCs with NPs in the experiments and free-energy minimization support that in our system only a small number of adhesive sites (receptors) that strongly bind to NPs is present in the membrane. Due to the limited receptor availability on the RBC membrane, the NPs are partially wrapped. Furthermore, my Brownian dynamics simulations suggested that multivalent binding is required to reproduce the experimental data and that only a limited number of receptors can bind to each NP. Partial-wrapped NPs that are attached to the outside of RBCs act as crenators via the area-difference elasticity mechanism, while they act as cup-formers via the spherical-cap mechanism. Furthermore, NPs that are attached to the outside of RBCs effectively decrease the area of the RBC membrane and

Conclusions and Outlook

increase the volume of the cell, thereby increase the reduced volume of the cell, and make RBCs more spherical. Because the mechanics of RBCs has been studied in detail in the past, the combination of experiments and theory furthermore allows us to quantitatively predict mechanisms by which the attached NPs alter the spontaneous curvature of cell membranes.

The adhesion of primary cortical neurons to 2D arrays of nano- and micropillars depends on the nanostructure of the substrates. My continuum-model membrane calculations reproduce experimental observations using SEM and FIB-SEM. I characterize the envelopment transition, the transition between the partial-wrapped (PW) and complete-wrapped (CW) state, and the energy barrier. For sufficiently high adhesion strength, the energy barrier between the PW and the CW state vanishes and wrapping occurs spontaneously, characterized by the wrapping spinodal. Nanostructured surfaces with small nanopillar radii r and large pitches l are the most favourable geometries to wrap. In case of the neuronal cells used in the experiments by my collaboration partner, three combinations of radii and pitches have been found ($r = 0.125 \mu\text{m}, l = 1 \mu\text{m}$), ($r = 0.25 \mu\text{m}, l = 1 \mu\text{m}$), and ($r = 0.375 \mu\text{m}, l = 1.5 \mu\text{m}$) for which the membrane wraps the nanopillars completely. Amongst them, the nanostructure geometry with $r = 0.25 \mu\text{m}$, and $l = 1 \mu\text{m}$ has the maximum relative nanopillar adhered area. By comparing experimental results and theoretical calculations, my theoretical model predicts an adhesion strength of $w = 30 \mu\text{J}/\text{m}^2$ for the cells to the substrate.

I studied in more detail the wrapping of a spherical particle by a RBC membrane, and consider as new aspect for NP-cell interaction, the underlying spectrin network explicitly in my calculations. Here the RBC cytoskeleton has been modelled using a hexagonal network of entropic springs with and without ankyrin complexes attached to the membrane. I measured the quasistatic particle energy contributions at equilibrium E_{sp} from the spectrin network for varying persistence lengths of the spectrin filament and radii of the particles. In the absence of ankyrin, E_{sp} increases with decreasing persistence lengths of the filaments, because the filaments are more flexible, which increases the spring constant of the entropic springs. Increasing the particle radius R also increases E_{sp} as the cytoskeleton hinders particle wrapping more for large particles. In the presence of ankyrin, I observed that the spectrin energy E_{sp} increases for increasing persistence lengths as the ankyrin reduces the entropy of the filaments, effectively make them softer and "explore" a larger area parallel to the membrane surface. Vice versa, the shorter the persistence length of the filaments, the closer they are to the membrane and hence particle wrapping is hindered less by the cytoskeleton. Overall, the presence of ankyrin assists particle wrapping and the wrapping transitions occur at lower adhesion strengths compared to the case with no ankyrin.

I investigated the wrapping of malaria-sized particles by RBC membranes with underlying spectrin networks. In order to access larger scales, I replaced the entropic springs by effective Hookean springs. There are two main forces at

play that drive wrapping, forces exerted on the particle due to molecular motors, and forces exerted due to particle-membrane adhesion. When particles pass through the spectrin network, the spring network is stretched, and if the stretching force provided by motor activity and adhesion strength is large enough that the cytoskeletal network breaks, the particle gets wrapped. For short spectrin breaking lengths, the spectrin bonds break while the particle is traversing through the network, while for long spectrin breaking lengths spectrin bonds break after the particle is already stuck in a PW state, leading to different wrapping dynamics in both the cases. Furthermore, I identified two different PW states for short spectrin breaking lengths; partial wrapping with intact spring network $\underline{\text{PW}}$, and partial wrapping with broken spring network $\overline{\text{PW}}$. I identified critical adhesion strengths and critical motor forces beyond which a particle is completely wrapped by the membrane, smaller for shorter spectrin breaking lengths and larger for longer spectrin breaking lengths, respectively. For short spectrin breaking length, the particles require small motor forces and adhesion strengths in order to get completely wrapped by the membrane, thus resulting in a smaller PW region compared to a longer spectrin breaking length. For a fixed spectrin breaking length, increasing particle size hinders wrapping. The crack patterns after complete wrapping of the particle show that the larger particles break more bonds compared to the smaller particles. Furthermore, for short spectrin breaking length, there are more broken spectrin bonds compared to the longer breaking length. This suggests that ‘healing’ of the cytoskeleton after complete wrapping is more efficient for small particle radii and long spectrin breaking lengths via cytoskeleton remodelling where spectrin bonds break and reconnect.

My calculations for the wrapping of particles by membranes with a cortical cytoskeleton consider a new aspect of particle-membrane wrapping. This is a step further from the previous works, where I have taken into account both a particle and the RBC spectrin network. It helps in our understanding of how nano- or malaria-sized particles enter RBCs, which could help in future studies related to NP drug discovery, or effective treatment of malaria. My results for the adsorption of NPs on RBCs are also of direct relevance for understanding mechanisms that can be applied in drug delivery and nanotoxicology, but they also provide a solid and systematic basis to study more complex cells by considering the RBCs as well-characterized cells. Because NPs can be highly reactive in adsorbing small molecules and macromolecules from their immediate environment, the formation of a so-called protein corona has to be taken into account for most applications involving biological systems [153,241]. The chemical composition of a NP corona can be of temporal nature, as it is a function of the abundance and chemical affinities of competitive adsorbing entities to the NPs’ surface [153]. Within my model, a corona can be taken into account through an effective NP size and an effective NP-membrane adhesive interaction. Systematic experimental studies to identify these effective parameters for each system are required to connect my generic study to specific experimental systems.

Conclusions and Outlook

My calculations for the wrapping of nanostructures by membranes show how a complex wrapping problem can be approached from a simple energetics point of view. They let us predict the optimal nanostructure geometries for experimental applications. If one were to construct different geometries for MEAs, my model provides an informed estimate of the membrane and geometric parameters on wrapping. One caveat in my approach could be that I neglect cytoskeletal contributions, which might help or hinder the wrapping process. Also, membrane fluctuations between the adjacent nanopillars have been neglected, which is out of the scope of the present work.

My work combines theoretical, experimental, and computational approaches, and captures the underlying physics of the particle wrapping process by the membrane. The natural extension would be to model the RBC membrane and use an explicit membrane model also for the lipid bilayer membrane, and investigate the interaction of nano- and microparticles with such a complex membrane. One could also study the effect of membrane fluctuations on the wrapping process, as well as the effect of the cytoskeleton on wrapping of cells by nanostructures. Finally, whole red blood cells do not have active uptake mechanisms, quantitative studies that differentiate between passive adhesion and uptake, and active, metabolic uptake processes for the interaction of NPs with other mammalian cells is a challenge for future studies.

Appendix A

First-passage time calculations

We define the first-passage time for a particle crossing the Red Blood Cell (RBC) membrane to be the time taken by the particle to go from wrapping fraction $f_w = 0$ to $f_w = 1$. For a particle with mass m diffusing in z direction in a medium with friction coefficient ζ , we can write the equations of motion [311]

$$\frac{dz}{dt} = v, \quad (\text{A.1})$$

$$\frac{m}{\zeta} \frac{dz}{dt} = -v + \frac{1}{\zeta} F(z) + \frac{1}{\zeta} \eta(t), \quad (\text{A.2})$$

where $F(z) = -U'(z)$ is the force exerted on the Brownian particle in the external potential $U(z)$ with the Gaussian white noise $\eta(t)$. This force is the adhesion force $F_{\text{adh}} = 2\pi R w_{\text{eff}}$ as mentioned in chapter 4.

For an overdamped system, $m/\zeta \ll 1$, and we obtain

$$\frac{dz}{dt} = \frac{1}{\zeta} F(z) + \frac{1}{\zeta} \eta(t). \quad (\text{A.3})$$

Using Einstein's relation $D = k_B T / \zeta$, the corresponding Fokker-Planck equation is the Smoluchovski equation

$$\partial_t P(z, t_{\text{pass}} | z_0, 0) = -\partial_z \left(\frac{1}{\zeta} F(z) P(z, t_{\text{pass}} | z_0, 0) \right) + D \frac{\partial^2 P(z, t_{\text{pass}} | z_0, 0)}{\partial z^2}. \quad (\text{A.4})$$

The average first-passage time satisfies the equation

$$\frac{1}{\zeta} F(z) \frac{d}{dz} t_{\text{pass}} + D \frac{d^2}{dz^2} t_{\text{pass}} = -1. \quad (\text{A.5})$$

Solving Eq. A.5 with $F(z) = F_{\text{adh}}$ for $R = 0.5 l_{\text{actin}}$ and $w_{\text{eff}} = 1 k_B T / l_{\text{actin}}^2$, and $D\gamma = 1 k_B T$, and plotting it along with the simulations, we obtain Fig. A.1, where we have used the boundary conditions $t_{\text{pass}}(z = R) = 0$, and $t_{\text{pass}}(z = -R) = t$. The simulations agree well with the theoretical line, and thus we benchmark our system for calculating the first-passage times for the particles passing through the spectrin network.

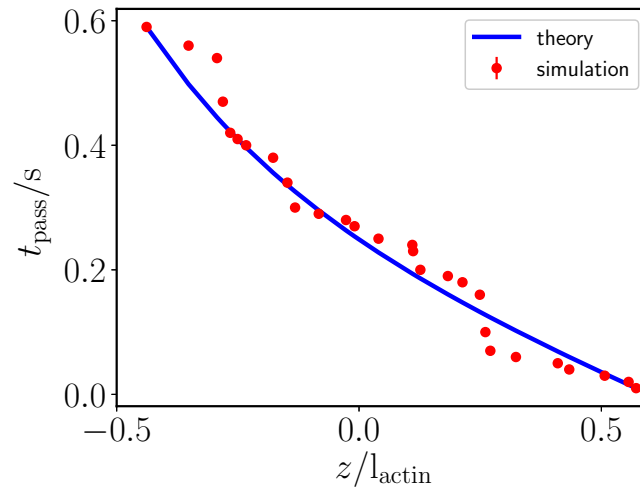


Figure A.1: First-passage time t_{pass} as function of z . The red points are the simulation points and the blue line is the theoretical line obtained by solving Eq. A.5.

Appendix B

Shear modulus of the RBC spectrin network

For a uniform network of springs with springs connected at six-fold coordinated junctions, the shear modulus μ [174],

$$\mu = \frac{\sqrt{3}k_{\text{sp}}}{4}. \quad (\text{B.1})$$

Equation B.1 applies only for small deformations of an unstretched network at zero temperature. We apply a shear force to the spring network, and calculate the deformation, which determines the shear modulus μ for the network (Fig. B.1). We plot shear modulus as function of the external force applied to the network F_{sp} along with the shear modulus obtained from Eq. (5.2) (Fig. B.2). We use spring constant $k_{\text{sp}} = 1$ and spring equilibrium length $l_{\text{eq}} = 1 l_{\text{actin}}$. For vanishing F_{sp} , we observe similar values of μ for simulation and theoretical calculations. For larger F_{sp} , the shear modulus μ obtained from simulation falls within the 1% deviation from the theoretical estimate.

Shear modulus of the RBC spectrin network

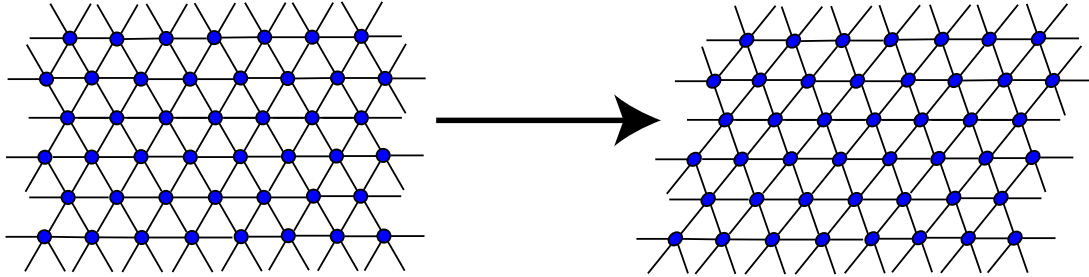


Figure B.1: Spring network before (left) and after (right) the application of the shear force.

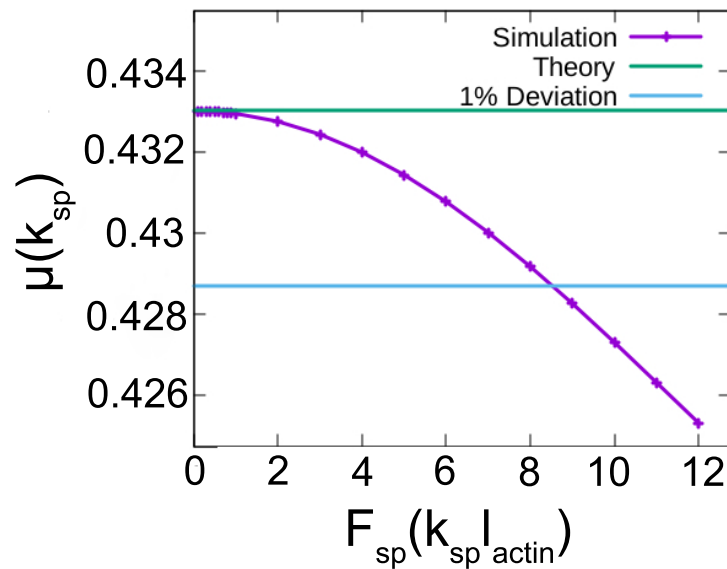


Figure B.2: Shear modulus μ as function of external force applied to the network F_{sp} (purple line). The green line is the value of μ calculated from Eq. (5.2). We use $k_{sp} = 1$ and $l_{eq} = 1 l_{actin}$. The blue line represents 1% deviation from the theoretical value.

Bibliography

- [1] J. Kreuter, *Nanoparticulate systems for brain delivery of drugs*, Adv. Drug Delivery Rev. **47**, 65 (2001).
- [2] Nanotechnology in medicine - nanomedicine, <http://www.understandingnano.com/medicine.html>, Accessed: 2017-18-12.
- [3] O. V. Salata, *Applications of nanoparticles in biology and medicine*, J. Nanobiotechnol. **2**, 3 (2004).
- [4] J. M. Aguilera and D. W. Stanley, *Microstructural principles of food processing and engineering*, Springer Science & Business Media, 1999.
- [5] J. Parada and J. Aguilera, *Food microstructure affects the bioavailability of several nutrients*, J. Food Sci. **72** (2007).
- [6] J. Kreuter, *Drug delivery to the central nervous system by polymeric nanoparticles: what do we know?*, Adv. Drug Delivery Rev. **71**, 2 (2014).
- [7] A. Schrade, Z. Cao, K. Landfester, and U. Ziener, *Preparation of raspberry-like nanocapsules by the combination of pickering emulsification and solvent displacement technique*, Langmuir **27**, 6689 (2011).
- [8] S. E. Gratton et al., *The effect of particle design on cellular internalization pathways*, Proc. Natl. Acad. Sci. U.S.A. **105**, 11613 (2008).
- [9] J. A. Champion and S. Mitragotri, *Role of target geometry in phagocytosis*, Proc. Natl. Acad. Sci. U.S.A. **103**, 4930 (2006).
- [10] S. Dasgupta, T. Auth, and G. Gompper, *Wrapping of ellipsoidal nanoparticles by fluid membranes*, Soft Matter **9**, 5473 (2013).
- [11] S. Dasgupta, T. Auth, and G. Gompper, *Shape and orientation matter for the cellular uptake of nonspherical particles*, Nano Lett. **14**, 687 (2014).
- [12] B. D. Chithrani, A. A. Ghazani, and W. C. Chan, *Determining the size and shape dependence of gold nanoparticle uptake into mammalian cells*, Nano Lett. **6**, 662 (2006).

BIBLIOGRAPHY

- [13] B. D. Chithrani and W. C. Chan, *Elucidating the mechanism of cellular uptake and removal of protein-coated gold nanoparticles of different sizes and shapes*, Nano Lett. **7**, 1542 (2007).
- [14] S. Barua et al., *Particle shape enhances specificity of antibody-displaying nanoparticles*, Proc. Natl. Acad. Sci. U.S.A. **110**, 3270 (2013).
- [15] H.-M. Ding and Y.-Q. Ma, *Role of physicochemical properties of coating ligands in receptor-mediated endocytosis of nanoparticles*, Biomaterials **33**, 5798 (2012).
- [16] S. Dasgupta, T. Auth, and G. Gompper, *Nano- and microparticles at fluid and biological interfaces*, J Phys.: Condens. Matter **29**, 373003 (2017).
- [17] Nanoparticle, <https://www.sciencedaily.com/terms/nanoparticle.htm>, Accessed: 2017-18-12.
- [18] Nanoparticle, <https://en.wikipedia.org/wiki/Nanoparticle>, Accessed: 2017-18-12.
- [19] T. A. Taton, *Nanostructures as tailored biological probes*, Trends Biotechnol. **20**, 277 (2002).
- [20] M. Bruchez, M. Moronne, P. Gin, S. Weiss, and A. P. Alivisatos, *Semiconductor nanocrystals as fluorescent biological labels*, Science **281**, 2013 (1998).
- [21] W. C. Chan and S. Nie, *Quantum dot bioconjugates for ultrasensitive non-isotopic detection*, Science **281**, 2016 (1998).
- [22] S. Wang, N. Mamedova, N. A. Kotov, W. Chen, and J. Studer, *Antigen/antibody immunocomplex from CdTe nanoparticle bioconjugates*, Nano Lett. **2**, 817 (2002).
- [23] C. Mah et al., *Microsphere-mediated delivery of recombinant AAV vectors in vitro and in vivo*, Mol. Ther. **1**, S239 (2000).
- [24] D. Pantarotto et al., *Immunization with peptide-functionalized carbon nanotubes enhances virus-specific neutralizing antibody responses*, Chem. Biol. **10**, 961 (2003).
- [25] R. Edelstein et al., *The BARC biosensor applied to the detection of biological warfare agents*, Biosens. Bioelectron. **14**, 805 (2000).
- [26] J.-M. Nam, C. S. Thaxton, and C. A. Mirkin, *Nanoparticle-based bio-bar codes for the ultrasensitive detection of proteins*, Science **301**, 1884 (2003).

- [27] R. Mahtab, J. P. Rogers, and C. J. Murphy, *Protein-sized quantum dot luminescence can distinguish between "straight", "bent", and "kinked" oligonucleotides*, J. Am. Chem. Soc. **117**, 9099 (1995).
- [28] J. Ma, H. Wong, L. Kong, and K.-W. Peng, *Biomimetic processing of nanocrystallite bioactive apatite coating on titanium*, Nanotechnol. **14**, 619 (2003).
- [29] A. De La Isla et al., *Nanohybrid scratch resistant coatings for teeth and bone viscoelasticity manifested in tribology*, Mater. Res. Innovations **7**, 110 (2003).
- [30] W. J. Parak et al., *Cell motility and metastatic potential studies based on quantum dot imaging of phagokinetic tracks*, Adv. Mater. **14**, 882 (2002).
- [31] Overview of cell structure, <http://exammasters.ca/overview-cell-structure/>, Accessed: 2017-18-12.
- [32] B. Alberts et al., *Essential cell biology*, Garland Science, 2013.
- [33] R. Milo and R. Phillips, *Cell biology by the numbers*, Garland Science, 2015.
- [34] M. M. Müller, *Theoretical studies of fluid membrane mechanics*, PhD thesis, Johannes Gutenberg-Universität in Mainz, 2007.
- [35] J. N. Israelachvili, *Intermolecular and Surface Forces*, Academic Press, 3rd edition, 2011.
- [36] Cell membrane, https://en.wikipedia.org/wiki/Cell_membrane, Accessed: 2017-08-11.
- [37] D. L. Nelson, A. L. Lehninger, and M. M. Cox, *Lehninger principles of biochemistry*, Macmillan, 2008.
- [38] O. G. Mouritsen, *Life-as a matter of fat*, Springer, 2005.
- [39] T. Heimburg, *Thermal biophysics of membranes*, John Wiley & Sons, 2008.
- [40] G. A. Jamieson and D. M. Robinson, *Mammalian cell membranes: Surface membranes of specific cell types*, Butterworths, 1977.
- [41] H. Lodish et al., *Molecular Cell Biology*, W.H. Freeman and Co., 2004.
- [42] M. Marsh and H. McMahon, *The structural era of endocytosis*, Science **285**, 215 (1999).

BIBLIOGRAPHY

- [43] B. Antonny, *Membrane deformation by protein coats*, *Curr. Opin. Struct. Biol.* **18**, 386 (2006).
- [44] M. S. Robinson, *Coats and vesicle budding*, *Trends Cell Biol.* **7**, 99 (1997).
- [45] H. T. McMahon and J. L. Gallop, *Membrane curvature and mechanisms of dynamic cell membrane remodelling*, *Nature* **438**, 590 (2005).
- [46] E. J. Luna and A. L. Hitt, *Cytoskeleton-plasma membrane interactions*, *SCIENCE-NEW YORK THEN WASHINGTON-* **258**, 955 (1992).
- [47] E. Chevalier-Larsen and E. L. Holzbaur, *Axonal transport and neurodegenerative disease*, *Biochim. Biophys. Acta, Mol. Basis Dis.* **1762**, 1094 (2006).
- [48] P. C. Bressloff and J. M. Newby, *Stochastic models of intracellular transport*, *Rev. Mod. Phys.* **85**, 135 (2013).
- [49] O. Rechavi, I. Goldstein, and Y. Kloog, *Intercellular exchange of proteins: the immune cell habit of sharing*, *FEBS Lett.* **583**, 1792 (2009).
- [50] I. A. Khalil, K. Kogure, H. Akita, and H. Harashima, *Uptake pathways and subsequent intracellular trafficking in nonviral gene delivery*, *Pharmacol. Rev.* **58**, 32 (2006).
- [51] S. Mayor and R. E. Pagano, *Pathways of clathrin-independent endocytosis*, *Nat. Rev. Mol. Cell Biol.* **8**, 603 (2007).
- [52] L.-A. H. Allen and A. Aderem, *Mechanisms of phagocytosis*, *Curr. Opin. Immunol.* **8**, 36 (1996).
- [53] A. Aderem and D. M. Underhill, *Mechanisms of phagocytosis in macrophages*, *Annu. Rev. Immunol.* **17**, 593 (1999).
- [54] H. Matsui, L. G. Johnson, S. H. Randell, and R. C. Boucher, *Loss of binding and entry of liposome-DNA complexes decreases transfection efficiency in differentiated airway epithelial cells*, *J. Biol. Chem.* **272**, 1117 (1997).
- [55] I. Kopatz, J.-S. Remy, and J.-P. Behr, *A model for non-viral gene delivery: Through syndecan adhesion molecules and powered by actin*, *J. Gene Med.* **6**, 769 (2004).
- [56] S. D. Conner and S. L. Schmid, *Regulated portals of entry into the cell*, *Nature* **422**, 37 (2003).
- [57] I. Canton and G. Battaglia, *Endocytosis at the nanoscale*, *Chem. Soc. Rev.* **41**, 2718 (2012).

- [58] C. Lamaze and S. L. Schmid, *The emergence of clathrin-independent pinocytic pathways*, *Curr. Opin. Cell Biol.* **7**, 573 (1995).
- [59] B. J. Reynwar et al., *Aggregation and vesiculation of membrane proteins by curvature-mediated interactions*, *Nature* **447**, 461 (2007).
- [60] H. T. McMahon and I. G. Mills, *COP and clathrin-coated vesicle budding: different pathways, common approaches*, *Curr. Opin. Cell Biol.* **16**, 379 (2004).
- [61] T. Kohyama, D. Kroll, and G. Gompper, *Budding of crystalline domains in fluid membranes*, *Phys. Rev. E* **68**, 061905 (2003).
- [62] K. Takei and V. Haucke, *Clathrin-mediated endocytosis: membrane factors pull the trigger*, *Trends Cell Biol.* **11**, 385 (2001).
- [63] S. Matveev, X. Li, W. Everson, and E. J. Smart, *The role of caveolae and caveolin in vesicle-dependent and vesicle-independent trafficking*, *Adv. Drug Delivery Rev.* **49**, 237 (2001).
- [64] J. Harris, D. Werling, J. C. Hope, G. Taylor, and C. J. Howard, *Caveolae and caveolin in immune cells: distribution and functions*, *Trends Immunol.* **23**, 158 (2002).
- [65] J. A. Swanson and C. Watts, *Macropinocytosis*, *Trends Cell Biol.* **5**, 424 (1995).
- [66] M. Amyere et al., *Origin, originality, functions, subversions and molecular signalling of macropinocytosis*, *Int. J. Med. Microbiol.* **291**, 487 (2001).
- [67] S. Sigismund et al., *Clathrin-independent endocytosis of ubiquitinated cargos*, *Proc. Natl. Acad. Sci. U.S.A.* **102**, 2760 (2005).
- [68] M. Kirkham and R. G. Parton, *Clathrin-independent endocytosis: new insights into caveolae and non-caveolar lipid raft carriers*, *Biochim. Biophys. Acta, Mol. Cell. Res.* **1745**, 273 (2005).
- [69] D. Derossi et al., *Cell internalization of the third helix of the Antennapedia homeodomain is receptor-independent*, *J. Biol. Chem.* **271**, 18188 (1996).
- [70] R. Tréhin and H. P. Merkle, *Chances and pitfalls of cell penetrating peptides for cellular drug delivery*, *Eur. J. Pharm. Biopharm.* **58**, 209 (2004).
- [71] C. Kleuss et al., *Assignment of G-protein subtypes to specific receptors inducing inhibition of calcium currents*, *Nature* **353**, 43 (1991).

BIBLIOGRAPHY

- [72] J. P. Leonetti, N. Mechti, G. Degols, C. Gagnor, and B. Lebleu, *Intracellular distribution of microinjected antisense oligonucleotides.*, Proc. Natl. Acad. Sci. U.S.A. **88**, 2702 (1991).
- [73] E. Barry, F. Gesek, and P. Friedman, *Introduction of antisense oligonucleotides into cells by permeabilization with streptolysin O.*, Biotechniques **15**, 1016 (1993).
- [74] P. Midoux, R. Mayer, and M. Monsigny, *Membrane permeabilization by α -helical peptides: a flow cytometry study*, Biochim. Biophys. Acta, Biomembr. **1239**, 249 (1995).
- [75] R. Bergan, Y. Connell, B. Fahmy, and L. Neckers, *Electroporation enhances c-myc antisense oligodeoxynucleotide efficacy*, Nucleic Acids Res. **21**, 3567 (1993).
- [76] U. Seifert, *Configurations of fluid membranes and vesicles*, Adv. Phys. **46**, 13 (1997).
- [77] F. Jülicher and R. Lipowsky, *Shape transformations of vesicles with intramembrane domains*, Phys. Rev. E **53**, 2670 (1996).
- [78] F. Jülicher and U. Seifert, *Shape equations for axisymmetric vesicles: a clarification*, Phys. Rev. E **49**, 4728 (1994).
- [79] U. Seifert, K. Berndl, and R. Lipowsky, *Shape transformations of vesicles: Phase diagram for spontaneous-curvature and bilayer-coupling models*, Phys. Rev. A **44**, 1182 (1991).
- [80] L. Miao, B. Fourcade, M. Rao, M. Wortis, and R. Zia, *Equilibrium budding and vesiculation in the curvature model of fluid lipid vesicles*, Phys. Rev. A **43**, 6843 (1991).
- [81] S. Svetina and B. Žekš, *Membrane bending energy and shape determination of phospholipid vesicles and red blood cells*, Eur. Biophys. J. **17**, 101 (1989).
- [82] U. Seifert and R. Lipowsky, *Adhesion of vesicles*, Phys. Rev. A **42**, 4768 (1990).
- [83] U. Seifert, *Self-consistent theory of bound vesicles*, Phys. Rev. Lett. **74**, 5060 (1995).
- [84] M. Deserno and T. Bickel, *Wrapping of a spherical colloid by a fluid membrane*, Europhys. Lett. **62**, 767 (2003).
- [85] M. Deserno, *Elastic deformation of a fluid membrane upon colloid binding*, Phys. Rev. E **69**, 031903 (2004).

-
- [86] A.-S. Smith, E. Sackmann, and U. Seifert, *Effects of a pulling force on the shape of a bound vesicle*, Europhys. Lett. **64**, 281 (2003).
- [87] A.-S. Smith, E. Sackmann, and U. Seifert, *Pulling tethers from adhered vesicles*, Phys. Rev. Lett. **92**, 208101 (2004).
- [88] G. Koster, A. Cacciuto, I. Derényi, D. Frenkel, and M. Dogterom, *Force barriers for membrane tube formation*, Phys. Rev. Lett. **94**, 068101 (2005).
- [89] I. Derényi, F. Jülicher, and J. Prost, *Formation and interaction of membrane tubes*, Phys. Rev. Lett. **88**, 238101 (2002).
- [90] T. R. Powers, G. Huber, and R. E. Goldstein, *Fluid-membrane tethers: minimal surfaces and elastic boundary layers*, Phys. Rev. E **65**, 041901 (2002).
- [91] K. Crane, *Discrete differential geometry: An applied introduction*, 2017.
- [92] Soap films and minimal surfaces, <https://redlegagenda.com/2015/09/23/soap-films-and-minimal-surfaces/>, Accessed: 2017-08-11.
- [93] W. Helfrich, *Elastic Properties of Lipid Bilayers: Theory and Possible Experiments*, Z. Naturforsch. c **28**, 693 (1973).
- [94] K. Khairy and J. Howard, *Minimum-energy vesicle and cell shapes calculated using spherical harmonics parameterization*, Soft Matter **7**, 2138 (2011).
- [95] W. Gózdź, *Deformations of lipid vesicles induced by attached spherical particles*, Langmuir **23**, 5665 (2007).
- [96] P. B. Canham, *The minimum energy of bending as a possible explanation of the biconcave shape of the human red blood cell*, J. Theor. Biol. **26**, 61 (1970).
- [97] E. A. Evans, *Bending elastic modulus of red blood cell membrane derived from buckling instability in micropipet aspiration tests*, Biophys. J. **43**, 27 (1983).
- [98] A. Zilker, H. Engelhardt, and E. Sackmann, *Dynamic reflection interference contrast (RIC-) microscopy: a new method to study surface excitations of cells and to measure membrane bending elastic moduli*, J. Phys. **48**, 2139 (1987).
- [99] H.-G. Döbereiner et al., *Advanced flicker spectroscopy of fluid membranes*, Phys. Rev. Lett. **91**, 048301 (2003).

BIBLIOGRAPHY

- [100] G. Morris, M. Pursell, S. Neethling, and J. Cilliers, *The effect of particle hydrophobicity, separation distance and packing patterns on the stability of a thin film*, J. Colloid Interface Sci. **327**, 138 (2008).
- [101] G. Apodaca, *Modulation of membrane traffic by mechanical stimuli*, Am. J. Physiol.-Renal Physiol. **282**, F179 (2002).
- [102] G. L. HW, M. Wortis, and R. Mukhopadhyay, *Stomatocyte–discocyte–echinocyte sequence of the human red blood cell: Evidence for the bilayer–couple hypothesis from membrane mechanics*, Proc. Natl. Acad. Sci. U.S.A. **99**, 16766 (2002).
- [103] E. L. Batchelder et al., *Membrane tension regulates motility by controlling lamellipodium organization*, Proc. Natl. Acad. Sci. U.S.A. **108**, 11429 (2011).
- [104] B. Pontes et al., *Membrane tension controls adhesion positioning at the leading edge of cells*, J. Cell Biol. , jcb (2017).
- [105] M. Herant, V. Heinrich, and M. Dembo, *Mechanics of neutrophil phagocytosis: behavior of the cortical tension*, J. Cell Sci. **118**, 1789 (2005).
- [106] A. E. Nel et al., *Understanding biophysicochemical interactions at the nanobio interface*, Nat. Mater. **8**, 543 (2009).
- [107] N. Dan, P. Pincus, and S. Safran, *Membrane-induced interactions between inclusions*, Langmuir **9**, 2768 (1993).
- [108] H. Aranda-Espinoza, A. Berman, N. Dan, P. Pincus, and S. Safran, *Interaction between inclusions embedded in membranes*, Biophys. J. **71**, 648 (1996).
- [109] R. Lipowsky and H.-G. Döbereiner, *Vesicles in contact with nanoparticles and colloids*, EPL (Europhys. Lett.) **43**, 219 (1998).
- [110] E. A. Evans and V. A. Parsegian, *Energetics of membrane deformation and adhesion in cell and vesicle aggregation*, Ann. N.Y. Acad. Sci. **416**, 13 (1983).
- [111] T. Kirchhausen, *Bending membranes*, Nat. Cell Biol. **14**, 906 (2012).
- [112] L. Johannes, C. Wunder, and P. Bassereau, *Bending on the rocks: a cocktail of biophysical modules to build endocytic pathways*, Cold Spring Harbor Perspect. Biol. **6**, a016741 (2014).
- [113] M. Ø. Jensen and O. G. Mouritsen, *Lipids do influence protein function—the hydrophobic matching hypothesis revisited*, Biochim. Biophys. Acta, Biomembr. **1666**, 205 (2004).

-
- [114] T. Auth and G. Gompper, *Self-avoiding linear and star polymers anchored to membranes*, Phys. Rev. E **68**, 051801 (2003).
- [115] C. Hiergeist and R. Lipowsky, *Elastic properties of polymer-decorated membranes*, J. Phys. II (France) **6**, 1465 (1996).
- [116] F. Campelo, H. T. McMahon, and M. M. Kozlov, *The hydrophobic insertion mechanism of membrane curvature generation by proteins*, Biophys. J. **95**, 2325 (2008).
- [117] B. Sorre et al., *Nature of curvature coupling of amphiphysin with membranes depends on its bound density*, Proc. Natl. Acad. Sci. U.S.A. **109**, 173 (2012).
- [118] J. C. Stachowiak et al., *Membrane bending by protein-protein crowding*, Nat. Cell Biol. **14**, 944 (2012).
- [119] P. N. Dannhauser and E. J. Ungewickell, *Reconstitution of clathrin-coated bud and vesicle formation with minimal components*, Nat. Cell Biol. **14**, 634 (2012).
- [120] R. Lipowsky and E. Sackmann, *Structure and dynamics of membranes: I. from cells to vesicles/II. generic and specific interactions*, Elsevier, 1995.
- [121] M. Do Carmo, *Differential geometry of curves and surfaces*, volume 2nd, Prentice Hall, 1976.
- [122] E. Kreyszig, *Introduction to differential geometry and Riemannian geometry*, volume 16, University of Toronto Press, 1968.
- [123] R. Capovilla, J. Guven, and J. Santiago, *Lipid membranes with an edge*, Phys. Rev. E **66**, 021607 (2002).
- [124] M. Traizet, *On the genus of triply periodic minimal surfaces*, J. Differ. Geom. **79**, 243 (2008).
- [125] K. Grosse-Brauckmann, *Triply periodic minimal and constant mean curvature surfaces*, Interface Focus **2**, 582 (2012).
- [126] M. Belushkin and G. Gompper, *Twist grain boundaries in cubic surfactant phases*, J. Chem. Phys. **130**, 134712 (2009).
- [127] U. Schwarz and G. Gompper, *Bicontinuous surfaces in self-assembling amphiphilic systems*, LECTURE NOTES IN PHYSICS-NEW YORK THEN BERLIN- , 107 (2002).
- [128] Y. Deng and M. Mieczkowski, *Three-dimensional periodic cubic membrane structure in the mitochondria of amoebae *Chaos carolinensis**, Protoplasma **203**, 16 (1998).

BIBLIOGRAPHY

- [129] S. Jiang, A. Göpfert, and V. Abetz, *Novel morphologies of block copolymer blends via hydrogen bonding*, *Macromolecules* **36**, 6171 (2003).
- [130] A. L. Mackay, *Periodic minimal surfaces*, *Physica B + C* **131**, 300 (1985).
- [131] I. Koltover, J. O. Rädler, and C. R. Safinya, *Membrane mediated attraction and ordered aggregation of colloidal particles bound to giant phospholipid vesicles*, *Phys. Rev. Lett.* **82**, 1991 (1999).
- [132] J. Käs and E. Sackmann, *Shape transitions and shape stability of giant phospholipid vesicles in pure water induced by area-to-volume changes*, *Biophys. J.* **60**, 825 (1991).
- [133] W. Wintz, H.-G. Döbereiner, and U. Seifert, *Starfish vesicles*, *EPL (Europhys. Lett.)* **33**, 403 (1996).
- [134] S. A. Safran, *Statistical thermodynamics of surfaces, interfaces, and membranes*, volume 90, Perseus Books, 1994.
- [135] M. Müller, K. Katsov, and M. Schick, *Biological and synthetic membranes: what can be learned from a coarse-grained description?*, *Phys. Rep.* **434**, 113 (2006).
- [136] M. Venturoli, M. M. Sperotto, M. Kranenburg, and B. Smit, *Mesosopic models of biological membranes*, *Phys. Rep.* **437**, 1 (2006).
- [137] J. C. Shillcock and R. Lipowsky, *Tension-induced fusion of bilayer membranes and vesicles*, *Nat. Mater.* **4**, 225 (2005).
- [138] J. C. Shillcock and R. Lipowsky, *The computational route from bilayer membranes to vesicle fusion*, *J. Phys.: Condens. Matter* **18**, S1191 (2006).
- [139] J. C. Shillcock, *Insight or illusion? Seeing inside the cell with mesoscopic simulations*, *HFSP J.* **2**, 1 (2008).
- [140] H. Noguchi, *Membrane simulation models from nanometer to micrometer scale*, *J. Phys. Soc. Jpn.* **78**, 041007 (2009).
- [141] V. V. Ginzburg, S. Balijepalli, K. A. Smith, and A. C. Balazs, *Approaches to Mesoscale Modeling of Nanoparticle–Cell Membrane Interactions*, *Nanotechnologies for the Life Sciences* (2009).
- [142] H. Noguchi and M. Takasu, *Fusion pathways of vesicles: a Brownian dynamics simulation*, *J. Chem. Phys.* **115**, 9547 (2001).
- [143] B. Granseth, B. Odermatt, S. J. Royle, and L. Lagnado, *Clathrin-mediated endocytosis is the dominant mechanism of vesicle retrieval at hippocampal synapses*, *Neuron* **51**, 773 (2006).

- [144] J. Balaji and T. Ryan, *Single-vesicle imaging reveals that synaptic vesicle exocytosis and endocytosis are coupled by a single stochastic mode*, Proc. Natl. Acad. Sci. U.S.A. **104**, 20576 (2007).
- [145] A. Chaudhuri, G. Battaglia, and R. Golestanian, *The effect of interactions on the cellular uptake of nanoparticles*, Phys Biol. **8**, 046002 (2011).
- [146] R. Vácha, F. J. Martinez-Veracoechea, and D. Frenkel, *Receptor-mediated endocytosis of nanoparticles of various shapes*, Nano Lett. **11**, 5391 (2011).
- [147] H. Yuan, J. Li, G. Bao, and S. Zhang, *Variable nanoparticle-cell adhesion strength regulates cellular uptake*, Phys. Rev. Lett. **105**, 138101 (2010).
- [148] H. Gao, W. Shi, and L. B. Freund, *Mechanics of receptor-mediated endocytosis*, Proc. Natl. Acad. Sci. U.S.A. **102**, 9469 (2005).
- [149] A.-S. Smith, K. Sengupta, S. Goennenwein, U. Seifert, and E. Sackmann, *Force-induced growth of adhesion domains is controlled by receptor mobility*, Proc. Natl. Acad. Sci. U.S.A. **105**, 6906 (2008).
- [150] S. F. Fenz, A.-S. Smith, R. Merkel, and K. Sengupta, *Inter-membrane adhesion mediated by mobile linkers: effect of receptor shortage*, Soft Matter **7**, 952 (2011).
- [151] J. Hu, R. Lipowsky, and T. R. Weikl, *Binding constants of membrane-anchored receptors and ligands depend strongly on the nanoscale roughness of membranes*, Proc. Natl. Acad. Sci. U.S.A. **110**, 15283 (2013).
- [152] T. Erdmann and U. S. Schwarz, *Stochastic dynamics of adhesion clusters under shared constant force and with rebinding*, J. Chem. Phys. **121**, 8997 (2004).
- [153] T. Cedervall et al., *Understanding the nanoparticle–protein corona using methods to quantify exchange rates and affinities of proteins for nanoparticles*, Proc. Natl. Acad. Sci. U.S.A. **104**, 2050 (2007).
- [154] B. D. Chithrani and W. C. Chan, *Elucidating the mechanism of cellular uptake and removal of protein-coated gold nanoparticles of different sizes and shapes*, Nano Lett. **7**, 1542 (2007).
- [155] S. Zhang, J. Li, G. Lykotrafitis, G. Bao, and S. Suresh, *Size-dependent endocytosis of nanoparticles*, Adv. Mater. **21**, 419 (2009).
- [156] N. Mücke et al., *Assessing the flexibility of intermediate filaments by atomic force microscopy*, J. Mol. Biol. **335**, 1241 (2004).

BIBLIOGRAPHY

- [157] F. Gittes, B. Mickey, J. Nettleton, and J. Howard, *Flexural rigidity of microtubules and actin filaments measured from thermal fluctuations in shape.*, J. Cell Biol. **120**, 923 (1993).
- [158] F. Pampaloni et al., *Thermal fluctuations of grafted microtubules provide evidence of a length-dependent persistence length*, Proc. Natl. Acad. Sci. U.S.A. **103**, 10248 (2006).
- [159] Microtubules, <https://www.cytoskeleton.com/motor-proteins/microtubules>, Accessed: 2017-08-11.
- [160] *Microtubules and Filaments*, Nature Education (2014).
- [161] Actin filament, <https://www.mechanobio.info/topics/cytoskeleton-dynamics/cytoskeleton/actin-filament/>, Accessed: 2017-08-11.
- [162] J. C. Winkelmann and B. G. Forget, *Erythroid and nonerythroid spectrins*, Blood **81**, 3173 (1993).
- [163] J. Li, M. Dao, C. Lim, and S. Suresh, *Spectrin-level modeling of the cytoskeleton and optical tweezers stretching of the erythrocyte*, Biophys. J. **88**, 3707 (2005).
- [164] V. L. Grum, D. Li, R. I. MacDonald, and A. Mondragón, *Structures of two repeats of spectrin suggest models of flexibility*, Cell **98**, 523 (1999).
- [165] J. Hansen, R. Skalak, S. Chien, and A. Hoger, *Influence of network topology on the elasticity of the red blood cell membrane skeleton*, Biophys. J. **72**, 2369 (1997).
- [166] S.-C. Liu, L. H. Derick, P. Agre, and J. Palek, *Alteration of the erythrocyte membrane skeletal ultrastructure in hereditary spherocytosis, hereditary elliptocytosis, and pyropoikilocytosis*, Blood **76**, 198 (1990).
- [167] J. A. Ursitti, D. W. Pumplin, J. B. Wade, and R. J. Bloch, *Ultrastructure of the human erythrocyte cytoskeleton and its attachment to the membrane*, Cytoskeleton **19**, 227 (1991).
- [168] B. Shen, *Ultrastructure and function of membrane skeleton*, Red Blood Cell Membranes: Structure, Function, Clinical Implications. Marcel Dekker, New York , 261 (1989).
- [169] S. Chien and L. A. Sung, *Molecular basis of red cell membrane rheology*, Biorheology **27**, 327 (1990).

- [170] V. Bennett and D. M. Gilligan, *The spectrin-based membrane skeleton and micron-scale organization of the plasma membrane*, *Annu. Rev. Cell Biol.* **9**, 27 (1993).
- [171] T. J. Byers and D. Branton, *Visualization of the protein associations in the erythrocyte membrane skeleton*, *Proc. Natl. Acad. Sci.* **82**, 6153 (1985).
- [172] S.-C. Liu, L. H. Derick, and J. Palek, *Visualization of the hexagonal lattice in the erythrocyte membrane skeleton.*, *J. Cell Biol.* **104**, 527 (1987).
- [173] M. Takeuchi, H. Miyamoto, Y. Sako, H. Komizu, and A. Kusumi, *Structure of the erythrocyte membrane skeleton as observed by atomic force microscopy*, *Biophys. J.* **74**, 2171 (1998).
- [174] D. Boal and D. H. Boal, *Mechanics of the Cell*, Cambridge University Press, 2012.
- [175] G.-Y. Huh, S. B. Glantz, S. Je, J. S. Morrow, and J. H. Kim, *Calpain proteolysis of α II-spectrin in the normal adult human brain*, *Neurosci. Lett.* **316**, 41 (2001).
- [176] A. Lesniak et al., *Nanoparticle adhesion to the cell membrane and its effect on nanoparticle uptake efficiency*, *J. Am. Chem. Soc.* **135**, 1438 (2013).
- [177] N. M. C. Membranes, *Probing Nonspecific Interactions using Model Membranes* Chen, Kai Loon; Bothun, Geoffrey D, *Environ. Sci. Technol.* **48**, 873 (2014).
- [178] A. C. Anselmo and S. Mitragotri, *An overview of clinical and commercial impact of drug delivery systems*, *J. Controlled Release* **190**, 15 (2014).
- [179] P. P. Wibroe et al., *Bypassing adverse injection reactions to nanoparticles through shape modification and attachment to erythrocytes*, *Nat. Nanotechnol.* **12**, 589 (2017).
- [180] K. Müller, D. A. Fedosov, and G. Gompper, *Margination of micro-and nano-particles in blood flow and its effect on drug delivery*, *Sci. Rep.* **4**, 4871 (2014).
- [181] P. U. Atukorale et al., *Influence of the glycocalyx and plasma membrane composition on amphiphilic gold nanoparticle association with erythrocytes*, *Nanoscale* **7**, 11420 (2015).
- [182] C. Wilhelm, F. Gazeau, J. Roger, J. Pons, and J.-C. Bacri, *Interaction of anionic superparamagnetic nanoparticles with cells: kinetic analyses of membrane adsorption and subsequent internalization*, *Langmuir* **18**, 8148 (2002).

BIBLIOGRAPHY

- [183] C. Poirier, D. Van Effenterre, B. Delord, L. Johannes, and D. Roux, *Specific adsorption of functionalized colloids at the surface of living cells: A quantitative kinetic analysis of the receptor-mediated binding*, *Biochim. Biophys. Acta, Biomembr.* **1778**, 2450 (2008).
- [184] S. Zhang, A. Nelson, and P. A. Beales, *Freezing or wrapping: the role of particle size in the mechanism of nanoparticle–biomembrane interaction*, *Langmuir* **28**, 12831 (2012).
- [185] A. Vakurov, R. Brydson, and A. Nelson, *Electrochemical modeling of the silica nanoparticle–biomembrane interaction*, *Langmuir* **28**, 1246 (2011).
- [186] J. Barnoud, G. Rossi, and L. Monticelli, *Lipid membranes as solvents for carbon nanoparticles*, *Phys. Rev. Lett.* **112**, 068102 (2014).
- [187] C. Huang, Y. Zhang, H. Yuan, H. Gao, and S. Zhang, *Role of nanoparticle geometry in endocytosis: laying down to stand up*, *Nano Lett.* **13**, 4546 (2013).
- [188] P. Gkeka, L. Sarkisov, and P. Angelikopoulos, *Homogeneous hydrophobic–hydrophilic surface patterns enhance permeation of nanoparticles through lipid membranes*, *J. Phys. Chem. Lett.* **4**, 1907 (2013).
- [189] K. Yang and Y.-Q. Ma, *Computer simulation of the translocation of nanoparticles with different shapes across a lipid bilayer*, *Nat. Nanotechnol.* **5**, 579 (2010).
- [190] A. H. Bahrami, R. Lipowsky, and T. R. Weigl, *The role of membrane curvature for the wrapping of nanoparticles*, *Soft Matter* **12**, 581 (2016).
- [191] J. Agudo-Canalejo and R. Lipowsky, *Critical particle sizes for the engulfment of nanoparticles by membranes and vesicles with bilayer asymmetry*, *ACS Nano* **9**, 3704 (2015).
- [192] A. Šarić and A. Cacciuto, *Fluid membranes can drive linear aggregation of adsorbed spherical nanoparticles*, *Phys. Rev. Lett.* **108**, 118101 (2012).
- [193] S. Semrau, T. Idema, T. Schmidt, and C. Storm, *Membrane-mediated interactions measured using membrane domains*, *Biophys. J.* **96**, 4906 (2009).
- [194] A. H. Bahrami, R. Lipowsky, and T. R. Weigl, *Tubulation and aggregation of spherical nanoparticles adsorbed on vesicles*, *Phys. Rev. Lett.* **109**, 188102 (2012).
- [195] T. Yue and X. Zhang, *Cooperative effect in receptor-mediated endocytosis of multiple nanoparticles*, *ACS Nano* **6**, 3196 (2012).

- [196] M. Raatz, R. Lipowsky, and T. R. Weigl, *Cooperative wrapping of nanoparticles by membrane tubes*, *Soft Matter* **10**, 3570 (2014).
- [197] A. Šarić and A. Cacciuto, *Mechanism of membrane tube formation induced by adhesive nanocomponents*, *Phys. Rev. Lett.* **109**, 188101 (2012).
- [198] M. Fošnarič, A. Iglič, D. M. Kroll, and S. May, *Monte Carlo simulations of complex formation between a mixed fluid vesicle and a charged colloid*, *J. Chem. Phys.* **131**, 09B610 (2009).
- [199] T. Hamada et al., *Size-dependent partitioning of nano/microparticles mediated by membrane lateral heterogeneity*, *J. Am. Chem. Soc.* **134**, 13990 (2012).
- [200] E. S. Melby et al., *Formation of supported lipid bilayers containing phase-segregated domains and their interaction with gold nanoparticles*, *Environ. Sci.: Nano* **3**, 45 (2016).
- [201] R. Mukhopadhyay, H. G. Lim, and M. Wortis, *Echinocyte shapes: bending, stretching, and shear determine spicule shape and spacing*, *Biophys. J.* **82**, 1756 (2002).
- [202] H. Deuling and W. Helfrich, *Red blood cell shapes as explained on the basis of curvature elasticity*, *Biophys. J.* **16**, 861 (1976).
- [203] M. P. Sheetz and S. Singer, *Biological membranes as bilayer couples. A molecular mechanism of drug-erythrocyte interactions*, *Proc. Natl. Acad. Sci. U.S.A.* **71**, 4457 (1974).
- [204] C. Monzel et al., *Measuring fast stochastic displacements of bio-membranes with dynamic optical displacement spectroscopy*, *Nat. Commun.* **6**, 8162 (2015).
- [205] H. Jung, A. D. Robison, and P. S. Cremer, *Multivalent ligand–receptor binding on supported lipid bilayers*, *J. Struct. Biol.* **168**, 90 (2009).
- [206] M. P. Allen and D. J. Tildesley, *Computer simulation of liquids*, Oxford University Press, 2017.
- [207] M. P. Sheetz, M. Schindler, and D. E. Koppel, *Lateral mobility of integral membrane proteins is increased in spherocytic erythrocytes*, *Nature* **285**, 510 (1980).
- [208] G. Rimon, N. Meyerstein, and Y. I. Henis, *Lateral mobility of phospholipids in the external and internal leaflets of normal and hereditary spherocytic human erythrocytes*, *Biochim. Biophys. Acta, Biomembr.* **775**, 283 (1984).

BIBLIOGRAPHY

- [209] B. Rózycki and R. Lipowsky, *Membrane curvature generated by asymmetric depletion layers of ions, small molecules, and nanoparticles*, J. Chem. Phys. **145**, 074117 (2016).
- [210] T. Auth and G. Gompper, *Budding and vesiculation induced by conical membrane inclusions*, Phys. Rev. E **80**, 031901 (2009).
- [211] E. Atilgan and S. X. Sun, *Shape transitions in lipid membranes and protein mediated vesicle fusion and fission*, J. Chem. Phys. **126**, 03B604 (2007).
- [212] W. L. Vaz, H. G. Kapitza, J. Stuempel, E. Sackmann, and T. M. Jovin, *Translational mobility of glycophorin in bilayer membranes of dimyristoylphosphatidylcholine*, Biochem. **20**, 1392 (1981).
- [213] W. L. Vaz, M. Criado, V. M. Madeira, G. Schoellmann, and T. M. Jovin, *Size dependence of the translational diffusion of large integral membrane proteins in liquid-crystalline phase lipid bilayers. A study using fluorescence recovery after photobleaching*, Biochem. **21**, 5608 (1982).
- [214] W. Vaz, D. Hallmann, R. Clegg, A. Gambacorta, and M. De Rosa, *A comparison of the translational diffusion of a normal and a membrane-spanning lipid in $L\alpha$ phase 1-palmitoyl-2-oleoylphosphatidylcholine bilayers*, Eur. Biophys. J. **12**, 19 (1985).
- [215] G. Seaman, R. Knox, F. Nordt, and D. Regan, *Red cell agins. I. Surface charge density and sialic acid content of density-fractionated human erythrocytes*, Blood **50**, 1001 (1977).
- [216] J. A. Chasis and N. Mohandas, *Red blood cell glycophorins*, Blood **80**, 1869 (1992).
- [217] N. G. d. Isla, B. D. Riquelme, R. J. Rasia, J. R. Valverde, and J. F. Stoltz, *Quantification of glycophorin A and glycophorin B on normal human RBCs by flow cytometry*, Transfusion **43**, 1145 (2003).
- [218] J. D. Corbett and D. E. Golan, *Band 3 and glycophorin are progressively aggregated in density-fractionated sickle and normal red blood cells. Evidence from rotational and lateral mobility studies.*, J. Clin. Invest. **91**, 208 (1993).
- [219] N. Kučerka, M.-P. Nieh, and J. Katsaras, *Fluid phase lipid areas and bilayer thicknesses of commonly used phosphatidylcholines as a function of temperature*, Biochim. Biophys. Acta Biomembr. **1808**, 2761 (2011).
- [220] A.-S. Smith and U. Seifert, *Effective adhesion strength of specifically bound vesicles*, Phys. Rev. E **71**, 061902 (2005).

-
- [221] G.-K. Xu, J. Hu, R. Lipowsky, and T. R. Weigl, *Binding constants of membrane-anchored receptors and ligands: A general theory corroborated by Monte Carlo simulations*, J. Chem. Phys. **143**, 12B613.1 (2015).
- [222] H. Noguchi and G. Gompper, *Shape transitions of fluid vesicles and red blood cells in capillary flows*, Proc. Natl. Acad. Sci. U.S.A. **102**, 14159 (2005).
- [223] D. A. Fedosov, B. Caswell, and G. E. Karniadakis, *A multiscale red blood cell model with accurate mechanics, rheology, and dynamics*, Biophys. J. **98**, 2215 (2010).
- [224] B. K. Pai and H. D. Weymann, *Equilibrium shapes of red blood cells in osmotic swelling*, J. Biomech. **13**, 105 (1980).
- [225] H.-G. Döbereiner, *Properties of giant vesicles*, Curr. Opin. Colloid Interface Sci. **5**, 256 (2000).
- [226] B. Jing and Y. Zhu, *Disruption of supported lipid bilayers by semihydrophobic nanoparticles*, J. Am. Chem. Soc. **133**, 10983 (2011).
- [227] Y. Guo, E. Terazzi, R. Seemann, J. B. Fleury, and V. A. Baulin, *Direct proof of spontaneous translocation of lipid-covered hydrophobic nanoparticles through a phospholipid bilayer*, Sci. Adv. **2**, e1600261 (2016).
- [228] M. Werner and J.-U. Sommer, *Translocation and induced permeability of random amphiphilic copolymers interacting with lipid bilayer membranes*, Biomacromolecules **16**, 125 (2014).
- [229] S. L. Richardson and P. Swietach, *Red blood cell thickness is evolutionarily constrained by slow, hemoglobin-restricted diffusion in cytoplasm*, Sci. Rep. **6**, 36018 (2016).
- [230] E. Evans and P. Leblond, *Geometric properties of individual red blood cell discocyte-spherocyte transformations.*, Biorheology **10**, 393 (1973).
- [231] P. Sens and N. Gov, *Force balance and membrane shedding at the red-blood-cell surface*, Phys. Rev. Lett. **98**, 018102 (2007).
- [232] W. Oberwagner et al., *Drug-induced endovesiculation of erythrocytes is modulated by the dynamics in the cytoskeleton/membrane interaction*, Blood Cells Mol. Dis. **64**, 15 (2017).
- [233] M. Bessis and R. I. Weed, *Living blood cells and their ultrastructure*, (1973).
- [234] D. A. Fedosov, M. Peltomäki, and G. Gompper, *Deformation and dynamics of red blood cells in flow through cylindrical microchannels*, Soft Matter **10**, 4258 (2014).

BIBLIOGRAPHY

- [235] D. A. Fedosov, H. Noguchi, and G. Gompper, *Multiscale modeling of blood flow: from single cells to blood rheology*, Biomech. Model. Mechanobiol. **13**, 239 (2014).
- [236] A. S. Popel and P. C. Johnson, *Microcirculation and hemorrheology*, Annu. Rev. Fluid Mech. **37**, 43 (2005).
- [237] H. H. Lipowsky, *Microvascular rheology and hemodynamics*, Microcirculation **12**, 5 (2005).
- [238] Z. He, J. Liu, and L. Du, *The unexpected effect of PEGylated gold nanoparticles on the primary function of erythrocytes*, Nanoscale **6**, 9017 (2014).
- [239] Y.-Z. Yoon, J. Kotar, G. Yoon, and P. Cicuta, *The nonlinear mechanical response of the red blood cell*, Phys. Biol. **5**, 036007 (2008).
- [240] Y.-Z. Yoon et al., *Flickering analysis of erythrocyte mechanical properties: dependence on oxygenation level, cell shape, and hydration level*, Biophys. J. **97**, 1606 (2009).
- [241] J. Müller et al., *Coating nanoparticles with tunable surfactants facilitates control over the protein corona*, Biomaterials **115**, 1 (2017).
- [242] P. Fattahi, G. Yang, G. Kim, and M. R. Abidian, *A review of organic and inorganic biomaterials for neural interfaces*, Adv. Mater. **26**, 1846 (2014).
- [243] R. M. Rothschild, *Neuroengineering tools/applications for bidirectional interfaces, brain–computer interfaces, and neuroprosthetic implants—a review of recent progress*, Front. Neuroeng. **3** (2010).
- [244] A. P. Alivisatos et al., *Nanotools for neuroscience and brain activity mapping*, ACS Nano **7**, 1850 (2013).
- [245] M. E. Spira and A. Hai, *Multi-electrode array technologies for neuroscience and cardiology*, Nat. Nanotechnol. **8**, 83 (2013).
- [246] A. Hai, J. Shappir, and M. E. Spira, *In-cell recordings by extracellular microelectrodes*, Nat. Methods **7**, 200 (2010).
- [247] S. Weidlich, K. J. Krause, J. Schnitker, B. Wolfrum, and A. Offenhäusser, *MEAs and 3D nanoelectrodes: electrodeposition as tool for a precisely controlled nanofabrication*, Nanotechnology **28**, 095302 (2017).
- [248] A. A. Belu, *Neurons on 3D Polymer Nanostructures*, PhD thesis, RWTH Aachen University, 2017.
- [249] X. Xie et al., *Mechanical model of vertical nanowire cell penetration*, Nano Lett. **13**, 6002 (2013).

- [250] F. Santoro et al., *Interfacing electrogenic cells with 3D nanoelectrodes: Position, shape, and size matter*, ACS Nano **8**, 6713 (2014).
- [251] D. Axelrod, *Total internal reflection fluorescence microscopy in cell biology*, Traffic **2**, 764 (2001).
- [252] K. Toma, H. Kano, and A. Offenhausser, *Label-free measurement of cell–electrode cleft gap distance with high spatial resolution surface plasmon microscopy*, ACS Nano **8**, 12612 (2014).
- [253] A. Friedmann, A. Hoess, A. Cismak, and A. Heilmann, *Investigation of cell–substrate interactions by focused ion beam preparation and scanning electron microscopy*, Acta Biomater. **7**, 2499 (2011).
- [254] G. Wrobel et al., *Transmission electron microscopy study of the cell–sensor interface*, J. R. Soc. Interface **5**, 213 (2008).
- [255] F. Santoro, E. Neumann, G. Panaitov, and A. Offenhäusser, *FIB section of cell–electrode interface: An approach for reducing curtaining effects*, Microelectron. Eng. **124**, 17 (2014).
- [256] L. C. Kapitein and C. C. Hoogenraad, *Which way to go? Cytoskeletal organization and polarized transport in neurons*, Mol. Cell. Neurosci. **46**, 9 (2011).
- [257] L. C. Kapitein and C. C. Hoogenraad, *Building the neuronal microtubule cytoskeleton*, Neuron **87**, 492 (2015).
- [258] T. Baumgart, S. T. Hess, and W. W. Webb, *Imaging coexisting fluid domains in biomembrane models coupling curvature and line tension*, Nature **425**, 821 (2003).
- [259] P. I. Kuzmin, S. A. Akimov, Y. A. Chizmadzhev, J. Zimmerberg, and F. S. Cohen, *Line tension and interaction energies of membrane rafts calculated from lipid splay and tilt*, Biophys. J. **88**, 1120 (2005).
- [260] F. Hochmuth, J.-Y. Shao, J. Dai, and M. P. Sheetz, *Deformation and flow of membrane into tethers extracted from neuronal growth cones*, Biophys. J. **70**, 358 (1996).
- [261] J. Dai, M. P. Sheetz, X. Wan, and C. E. Morris, *Membrane tension in swelling and shrinking molluscan neurons*, J. Neurosci. **18**, 6681 (1998).
- [262] A. Kell and R. W. Glaser, *On the mechanical and dynamic properties of plant cell membranes: their role in growth, direct gene transfer and protoplast fusion*, J. Theor. Biol. **160**, 41 (1993).

BIBLIOGRAPHY

- [263] X. Xie, A. Aalipour, S. V. Gupta, and N. A. Melosh, *Determining the time window for dynamic nanowire cell penetration processes*, ACS Nano **9**, 11667 (2015).
- [264] C. Xie, Z. Lin, L. Hanson, Y. Cui, and B. Cui, *Intracellular recording of action potentials by nanopillar electroporation*, Nat. Nanotechnol. **7**, 185 (2012).
- [265] J. Li, G. Lykotrafitis, M. Dao, and S. Suresh, *Cytoskeletal dynamics of human erythrocyte*, Proc. Natl. Acad. Sci. U.S.A. **104**, 4937 (2007).
- [266] G. Marcelli, K. H. Parker, and C. P. Winlove, *Thermal fluctuations of red blood cell membrane via a constant-area particle-dynamics model*, Biophys. J. **89**, 2473 (2005).
- [267] L. Pan, R. Yan, W. Li, and K. Xu, *Super-Resolution Microscopy Reveals the Native Ultrastructure of the Erythrocyte Cytoskeleton*, Cell Rep. **22**, 1151 (2018).
- [268] N. Gov and S. Safran, *Red blood cell membrane fluctuations and shape controlled by ATP-induced cytoskeletal defects*, Biophys. J. **88**, 1859 (2005).
- [269] N. Gov and S. Safran, *Red blood cell shape and fluctuations: cytoskeleton confinement and ATP activity*, J. Biol. Phys. **31**, 453 (2005).
- [270] Biological molecules 2: Modelling dna and rna, <http://biologicalphysics.iop.org/cws/article/lectures/48662>, Accessed: 2018-02-03.
- [271] N. S. Gov, *Less is more: removing membrane attachments stiffens the RBC cytoskeleton*, New J. Phys. **9**, 429 (2007).
- [272] J. Mills et al., *Nonlinear elastic and viscoelastic deformation of the human red blood cell with optical tweezers*, Mech. Chem. Biosyst. **1**, 169 (2004).
- [273] C. Humpert and M. Baumann, *Local membrane curvature affects spontaneous membrane fluctuation characteristics*, Mol. Membr. Biol. **20**, 155 (2003).
- [274] R. W. Snow, C. A. Guerra, A. M. Noor, H. Y. Myint, and S. I. Hay, *The global distribution of clinical episodes of Plasmodium falciparum malaria*, Nature **434**, 214 (2005).
- [275] A. F. Cowman and B. S. Crabb, *Invasion of red blood cells by malaria parasites*, Cell **124**, 755 (2006).

-
- [276] J. Baum, T.-W. Gilberger, F. Frischknecht, and M. Meissner, *Host-cell invasion by malaria parasites: insights from Plasmodium and Toxoplasma*, Trends Parasitol. **24**, 557 (2008).
- [277] L. Bannister and A. Dluzewski, *The ultrastructure of red cell invasion in malaria infections: a review.*, Blood Cells **16**, 257 (1990).
- [278] S. Dasgupta et al., *Membrane-wrapping contributions to malaria parasite invasion of the human erythrocyte*, Biophys. J. **107**, 43 (2014).
- [279] M. Aikawa, L. H. Miller, J. Johnson, and J. Rabbage, *Erythrocyte entry by malarial parasites. A moving junction between erythrocyte and parasite*, J. Cell Biol. **77**, 72 (1978).
- [280] L. Bannister, G. Butcher, E. Dennis, and G. Mitchell, *Structure and invasive behaviour of Plasmodium knowlesi merozoites in vitro*, Parasitology **71**, 483 (1975).
- [281] J. Baum, A. T. Papenfuss, B. Baum, T. P. Speed, and A. F. Cowman, *Regulation of apicomplexan actin-based motility*, Nat. Rev. Microbiol. **4**, 621 (2006).
- [282] A. Keeley and D. Soldati, *The glideosome: a molecular machine powering motility and host-cell invasion by Apicomplexa*, Trends Cell Biol. **14**, 528 (2004).
- [283] P. K. Harris et al., *Molecular identification of a malaria merozoite surface sheddase*, PLoS Pathog. **1**, e29 (2005).
- [284] G. Mitchell, L. Bannister, and R. Sinden, *Malaria parasite invasion: interactions with the red cell membrane*, Crit. Rev. Oncol. Hemat. **8**, 255 (1988).
- [285] K. Lingelbach and K. A. Joiner, *The parasitophorous vacuole membrane surrounding Plasmodium and Toxoplasma: an unusual compartment in infected cells*, J. Cell Sci. **111**, 1467 (1998).
- [286] K. Ayi, W. C. Liles, P. Gros, and K. C. Kain, *Adenosine triphosphate depletion of erythrocytes simulates the phenotype associated with pyruvate kinase deficiency and confers protection against Plasmodium falciparum in vitro*, J. Infect. Dis. **200**, 1289 (2009).
- [287] J. A. Olson and A. Kilejian, *Involvement of spectrin and ATP in infection of resealed erythrocyte ghosts by the human malarial parasite, Plasmodium falciparum.*, J. Cell Biol. **95**, 757 (1982).

BIBLIOGRAPHY

- [288] Y. Park et al., *Metabolic remodeling of the human red blood cell membrane*, Proc. Natl. Acad. Sci. USA **107**, 1289 (2010).
- [289] P. Srinivasan et al., *Binding of Plasmodium merozoite proteins RON2 and AMA1 triggers commitment to invasion*, Proc. Natl. Acad. Sci. USA **108**, 13275 (2011).
- [290] S. Singh, M. M. Alam, I. Pal-Bhowmick, J. A. Brzostowski, and C. E. Chitnis, *Distinct external signals trigger sequential release of apical organelles during erythrocyte invasion by malaria parasites*, PLoS Pathog. **6**, e1000746 (2010).
- [291] D. T. Riglar et al., *Super-resolution dissection of coordinated events during malaria parasite invasion of the human erythrocyte*, Cell Host Microbe **9**, 9 (2011).
- [292] V. L. Lew and T. Tiffert, *Is invasion efficiency in malaria controlled by pre-invasion events?*, Trends Parasitol. **23**, 481 (2007).
- [293] F. Angrisano et al., *Spatial localisation of actin filaments across developmental stages of the malaria parasite*, PloS ONE **7**, e32188 (2012).
- [294] L. H. Miller, M. Aikawa, J. G. Johnson, and T. Shiroishi, *Interaction between cytochalasin B-treated malarial parasites and erythrocytes. Attachment and junction formation.*, J. Exp. Med. **149**, 172 (1979).
- [295] E. S. Zuccala and J. Baum, *Cytoskeletal and membrane remodelling during malaria parasite invasion of the human erythrocyte*, Br. J. Haematol. **154**, 680 (2011).
- [296] J. M. Dobrowolski and L. D. Sibley, *Toxoplasma invasion of mammalian cells is powered by the actin cytoskeleton of the parasite*, Cell **84**, 933 (1996).
- [297] N. Andenmatten et al., *Conditional genome engineering in Toxoplasma gondii uncovers alternative invasion mechanisms*, Nat. Methods **10**, 125 (2013).
- [298] V. Gonzalez et al., *Host cell entry by apicomplexa parasites requires actin polymerization in the host cell*, Cell Host Microbe **5**, 259 (2009).
- [299] Malaria, <http://www.austincc.edu/microbio/2704w/pf.htm>, Accessed: 2017-30-12.
- [300] H. Strey, M. Peterson, and E. Sackmann, *Measurement of erythrocyte membrane elasticity by flicker eigenmode decomposition*, Biophys. J. **69**, 478 (1995).

- [301] N. Gov, A. Zilman, and S. Safran, *Cytoskeleton confinement and tension of red blood cell membranes*, Phys. Rev. Lett. **90**, 228101 (2003).
- [302] U. Seifert and R. Lipowsky, *Morphology of vesicles*, Handb. Biol. Phys. **1**, 403 (1995).
- [303] D. E. Discher, D. H. Boal, and S. K. Boey, *Simulations of the erythrocyte cytoskeleton at large deformation. II. Micropipette aspiration*, Biophys. J. **75**, 1584 (1998).
- [304] D. H. Boal, *Computer simulation of a model network for the erythrocyte cytoskeleton*, Biophys. J. **67**, 521 (1994).
- [305] V. Heinrich, K. Ritchie, N. Mohandas, and E. Evans, *Elastic thickness compressibility of the red cell membrane*, Biophys. J. **81**, 1452 (2001).
- [306] S. Tsukita, H. Ishikawa, S. Sato, and M. Nakao, *Electron microscope study of reassociation of spectrin and actin with the human erythrocyte membrane*, J. Cell Biol. **90**, 70 (1981).
- [307] M. Puig-de Morales-Marinkovic, K. T. Turner, J. P. Butler, J. J. Fredberg, and S. Suresh, *Viscoelasticity of the human red blood cell*, Am. J. Physiol. Cell Physiol. **293**, C597 (2007).
- [308] M. Dao, C. T. Lim, and S. Suresh, *Mechanics of the human red blood cell deformed by optical tweezers*, J. Mech. Phys. Solids **51**, 2259 (2003).
- [309] P. Bronkhorst et al., *A new method to study shape recovery of red blood cells using multiple optical trapping*, Biophys. J. **69**, 1666 (1995).
- [310] T. M. Fischer, *Shape memory of human red blood cells*, Biophys. J. **86**, 3304 (2004).
- [311] The kramers problem and first passage times, <http://physics.gu.se/~frtbm/joomla/media/mydocs/LennartSjogren/kap8.pdf>, Accessed: 2018-06-03.

Ich versichere, daß ich die von mir vorgelegte Dissertation selbständig angefertigt, die benutzten Quellen und Hilfsmittel vollständig angegeben und die Stellen der Arbeit — einschließlich Tabellen, Karten und Abbildungen —, die anderen Werken im Wortlaut oder dem Sinn nach entnommen sind, in jedem Einzelfall als Entlehnung kenntlich gemacht habe; daß diese Dissertation noch keiner anderen Fakultät oder Universität zur Prüfung vorgelegen hat; daß sie — abgesehen unten angegebenen Teilpublikationen — noch nicht veröffentlicht worden ist sowie, daß ich eine solche Veröffentlichung vor Abschluß des Promotionsverfahrens nicht vornehmen werde. Die Bestimmungen der Promotionsordnung sind mir bekannt. Die von mir vorgelegte Dissertation ist von Professor Gompper betreut worden.

Köln, den 15. März 2018

Karandeep Singh

Adresse	Ehrenfeldgürtel 8 50823 Köln
Geburtsdatum	26.12.1990
Geburtsort	Sareyan
Familienstand	Ledig
Staatsangehörigkeit	Indisch
1993 – 2006	Grundschule St. Thomas Sen. Sec. School Ludhiana
2006 – 2008	Gymnasium Shishu Niketan Model Sen. Sec. School Chandigarh
2009 – 2014	Physikstudium IISER Mohali Mohali Masterarbeit mit dem Thema „Endocytosis of Nanoparticles“
seit August 2014	Doktorarbeit Forschungszentrum Jülich
seit Oktober 2014	Promotionsstudium Universität zu Köln

Köln, den 15. März 2018

